COMPUTATIONALLY-EFFICIENT FINITE-ELEMENT-BASED THERMAL AND ELECTROMAGNETIC MODELS OF ELECTRIC MACHINES

by

Kan Zhou

A dissertation submitted in partial fulfillment
of the requirements for the degree of
Doctor of Philosophy
(Electrical Engineering: Systems)
in the University of Michigan
2015

Doctoral Committee:

Associate Professor Heath F. Hofmann, Chair
Professor Ian A. Hiskens
Assistant Professor Johanna L. Mathieu
Professor Anna G. Stefanopoulou

DEDICATION

This dissertation is dedicated to my wife, Huan, for her unconditional love, support and encouragement over the past years.

ACKNOWLEDGMENTS

Getting through graduate school is not easy, but I am lucky to have received a lot of support from everywhere in the past five years. This journey would not have been such enjoyable without the help from all the wonderful people around me. No words could sufficiently express my gratitude but I will try my best here.

I would like to thank my family first. My father has been a role model to me since my childhood. He teaches me how to approach any problem logically, and encouraged to me to be an engineer just as he is. He also teaches me to be happy even when the world does not go my way. I find this lesson extremely valuable. My mother loves me with all her heart, and cares about me all the time. And of course thank my wife Huan for everything in the past five years. She has shown me nothing but unconditional love and support. Without her, I would not have been here today.

Research advisor is probably the most important person in a graduate student's academic life, and I am lucky to have Professor Heath Hofmann as my advisor in the past five years. He has provided me with the perfect balance between research freedom and hands-on guidance, which I appreciate a lot. Not only his research insights, but also his personality and philosophy has taught me many valuable lessons. I would like to express my deepest gratitude to Heath for all his academic and life advice, and all the help, encouragement, and support during my graduate study.

I would also like to extend my sincere gratitude to my professors and research collaborators in the past five years. I appreciate the valuable feedback and suggestions from Professors Ian Hiskens, Johanna Mathieu, and Anna Stefanopoulou, and thank them for being my committee members. Special thanks to Professor Stefanopoulou for her guid-

ance and support since 2011, and for organizing and leading such a successful Automotive Research Center, which has funded and helped so many students like myself. Professor Zoran Filipi, Professor John Wagner, Dr. Andrej Ivanco, William (Xinran) Tao, and Anna (Xueyu) Zhang have been such great research collaborators for years. Without them, a lot of my research production would not have happened. I am also grateful to my collaborators from industry and government – Dr. Xiao Hu (ANSYS), Dr. Lei Hao (GM), Dr. Zed Tang (ANSYS), Dr. Ed Tate (Exa), Dr. Wesley Zanardelli (GM), and Dr. Denise Rizzo (TARDEC) for all their help and support.

Finally I would like to thank my fellow PhD students at Michigan Power and Energy Lab, Jun Hou, Fei Lv, Dr. Jason Pries, Dave Reed, Aaron Stein, Abdi Zeynu for all the help and the enjoyable time we spent together. Thank my lab mates Chao Ma, Prerit Terway, and Victoria Cheung for all the good work. The gratitude is extended my office mates Sina Baghsorkhi, Stephanie Crocker, and Matt Kvalheim for making EECS4305 such a nice and enjoyable office to work in. At last I would like to express my gratitude to my friends Boxiao Chen, Wendy (Hsiaomin) Huang, Larry (Miaobin) Lien, Yang Liu, Peng Tian, Jiangfeng Wu, Chunyang Zhai, Cheng Zhang, Qi Zheng, and Tong Zhou, for all the good time together.

TABLE OF CONTENTS

LIST OF FIGURES

LIST OF TABLES

LIST OF ALGORITHMS

LIST OF ABBREVIATIONS

ADI alternating direction implicit

CAD Computer Aided Design

CE computationally-efficient

CFD Computational Fluid Dynamics

EC Equivalent Circuit

EM electromagnetic

EV Electric Vehicle

FE finite element

FEA Finite Element Analysis

GHG greenhouse gas

HEV Hybrid Electric Vehicle

IGBT insulated-gate bipolar transistor

LP lumped-parameter

LDV light-duty vehicle

MOR Model Order Reduction

MQS magneto-quasistatic

MS magneto-static

MTPA max torque per ampere

MVP magnetic vector potential

ODE ordinary differential equation

PDE partial differential equation

PM permanent magnet

PMSM permanent magnet synchronous machine

ROM reduced-order model

RTD Resistance Temperature Detector

SVD Singular Value Decomposition

ABSTRACT

COMPUTATIONALLY-EFFICIENT FINITE-ELEMENT-BASED THERMAL AND ELECTROMAGNETIC MODELS OF ELECTRIC MACHINES

by

Kan Zhou

Chair: Heath F. Hofmann

With the modern trend of transportation electrification, electric machines are a key component of electric/hybrid electric vehicle (EV/HEV) powertrains. It is therefore important that vehicle powertrain-level and system-level designers and control engineers have access to accurate yet computationally-efficient (CE), physics-based modeling tools of the thermal and electromagnetic (EM) behavior of electric machines. In this dissertation, CE yet accurate thermal and EM models for electric machines, which are suitable for use in vehicle powertrain design, optimization, and control, are developed. This includes not only creating fast and accurate thermal and EM models for specific machine designs, but also the ability to quickly generate and determine the performance of new machine designs through the application of scaling techniques to existing designs. With the developed techniques, the thermal and EM performance can be accurately and efficiently estimated. Furthermore, powertrain or system designers can easily and quickly adjust the characteristics and the performance of the machine in ways that are favorable to the overall vehicle performance.

CHAPTER 1

Introduction

1.1 Background and Motivation

Motivated by the needs of improving fuel economy, reducing pollution and greenhouse gas (GHG) emissions, and decreasing dependence on petroleum fuels, research interests in transportation electrification and Electric Vehicle/Hybrid Electric Vehicle (EV/HEV) have been increasing for years. Various reports have suggested that EV/HEVs need to possess a large portion of market share in the next 25-35 years to satisfy the regulatory emission standards and achieve GHG reduction goals. For example, a national goal for electrification was set in [1] that by 2040, 75% of the vehicle miles traveled in the U.S. should be electric miles. The U.S. Department of Energy suggests that advanced powertrain vehicles have the potential to dominate the light-duty vehicle (LDV) market by 2050 [2], where conventional vehicles with internal combustion engines will only have 8% market share, as shown in Fig. 1.1.

With such trend of transportation electrification, electric machines are a key component of EV/HEV powertrains. As a result, there is increasing interest in the simulation, modeling, and optimization of electric machines to achieve better performance, reduced cost, and improved reliability of electric machines. Electric machines are fundamentally multi-physical. The physics involved in machine operation include electromagnetic (EM), thermal (heat conduction, convection, and radiation), fluid dynamics, structural, noise and

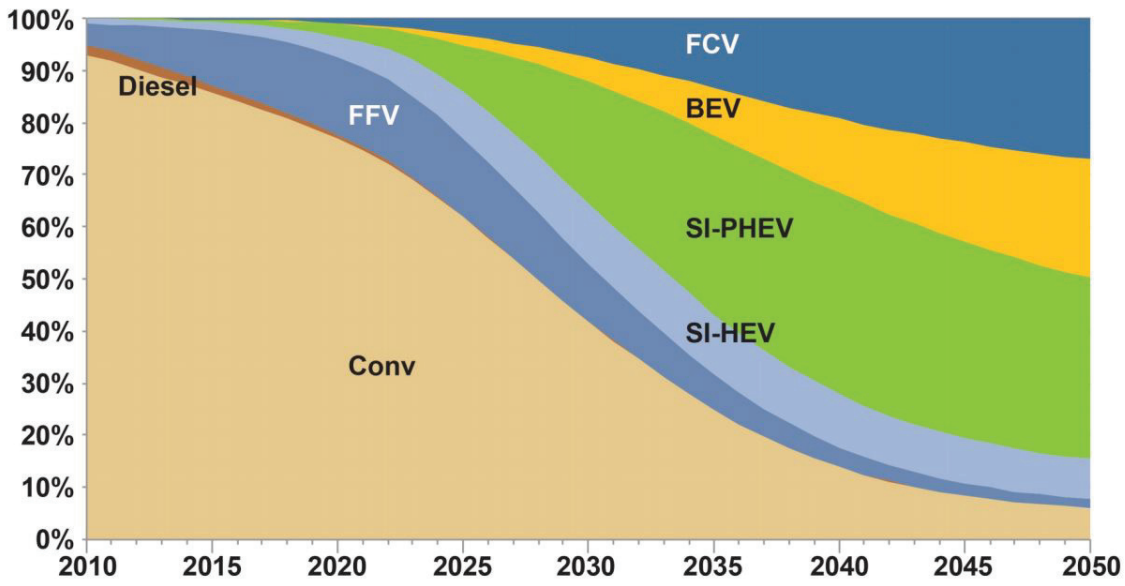

Figure 1.1: Advanced powertrain vehicles have the potential to dominate the LDV market by 2050, figure from [2].

vibration, etc. Each type of physics plays an important role in the high performance and high reliability operation of electric machines. This dissertation focuses on the EM and thermal perspectives of electric machines.

There are two levels of electric machine modeling and simulation – the component level and the system level. For component-level modeling, the focus is usually on improving accuracy, and making sure the simulation can accurately reflect the physics. Thus it can to some extent replace expensive prototyping and testing. These models are usually slow to run, since they capture a lot of details. For system-level modeling, the electric machine models are integrated in a larger and higher-level simulation/optimization/control framework, e.g. vehicle powertrain. Thus, the detailed but slow component-level models are no longer suitable for these purposes due to computational constraints. It is therefore important that vehicle powertrain-level and system-level designers and control engineers have access to accurate, computationally-efficient (CE), and physics-based modeling tools for electric machines. To satisfy such needs, this dissertation is focused on CE modeling of electric machines, where two physics are included – thermal and EM.

1.2 Literature Review and Objectives

In this section, the literature on thermal and EM modeling of electric machines is reviewed, where CE modeling is the focus. The literature on the applications of CE models is also included. Based on the context and background established through the literature review, the objectives of this dissertation are presented at the end of each subsection.

1.2.1 Thermal Modeling

Thermal models are used to determine the internal temperatures of electric machines. In previous works, both lumped-parameter-based and finite-element-based thermal models have been used to capture the thermal dynamics of electric machines.

In lumped-parameter (LP) thermal models, the geometry of an electric machine is lumped into discrete circuit components, such as thermal resistor, thermal capacitor, and heat sources. These models are usually relatively fast [3, 4]. However, complex and large LP models are required to accurately capture the distributed nature of the losses, the temperature distribution in the machine, and the complexity of the machine geometry [5]. Additionally, the appropriate structure/topology and resulting thermal parameters of the LP models, and their sensitivity to variations in cooling conditions, can be difficult to identify [6].

Finite element (FE) method can be used to accurately predict the internal temperatures of a machine with complex geometries, where the geometry of an electric machine is meshed into small elements. Both 2D [7] and 3D [8, 9] finite element analysis (FEA) has been used in previous work. These approaches can provide accurate and distributed temperature information inside the machine, and can model complex structures easily by importing geometry directly from Computer Aided Design (CAD) softwares. However, solving FEA models is time-consuming (especially 3D FEA).

The temperature knowledge is valuable in practice and has been implemented in dif-

ferent applications, e.g., 1) determining the temperature-dependent power capability of an electric machine at a given instant in time [10]. This information allows high-performance operation of electric machines, especially when operating under severe duty cycles where thermal limitations overshadow other physical limitations; 2) protection and condition monitoring [11, 12], to ensure electric machines operate safely under temperature limits; 3) machine design optimization [13]; and 4) real-time implementation in a system-level control algorithm, or in full-scale vehicle-level powertrain simulation and optimization routine [14, 15].

Many of these applications require the thermal models to be computationally efficient while maintaining sufficient accuracy. Thus, to make the full-order dynamic thermal models computationally efficient, various model order reduction (MOR) techniques have been used previously [16]. For electric machine thermal modeling, pole-zero cancellation and Hankel Singular Value Decomposition (SVD) were used in [17] to build a two-state thermal model for induction machines based on a lumped-parameter model. A transfer-function-based system identification approach was used in [18] to generate low-order reduced models for induction machines. A 1600-node lumped-parameter induction machine model was reduced to 4 nodes using a transfer-function-based MOR approach in [19]. A balanced-truncation MOR method was used in [20] for the LP permanent magnet synchronous machine (PMSM) thermal models. However, the accuracy of each of these reduced-order models (ROMs) is fundamentally limited by the accuracy of the original lumped-parameter model.

An FEA-based MOR method for power electronic circuits was presented in [21]. The FE mesh is partitioned into different regions to build a LP equivalent circuit (EC). The lumped parameters are determined by steady-state FEA results. However, this approach only reduces the full-order FE model to a medium-order EC model with hundreds of states. Moreover, the MOR process involves an iterative process for determining the size of the reduced model, and a training process is needed to accurately estimate the parameters for

the EC.

Eigenfunction-based techniques have been used for modeling power electronic circuits [22] and electric machines [23]. However, the techniques presented in [22] require calculating a huge number of eigenfunctions (10^5-10^6) for the multilayer structure to achieve good accuracy. Furthermore, the method is restricted to systems where all layers have the same horizontal extent of rectangular shape, which is not suitable for modeling electric machines.

In one of my early works, a CE thermal model was presented [23], where the calculation of all the eigenvalues/eigenvectors of the FE matrices is required. This is computationally infeasible for the huge matrices generated by 3D FEA. Furthermore, the 2D machine model used in [23] cannot accurately capture the temperature variation in the axial direction of the electric machine. Convective cooling on the ends of the machine also needs to be modeled to achieve better accuracy. Thus, a 3D model is necessary to accurately capture the thermal dynamics in the machine.

In this dissertation, one of the objectives is to develop a CE dynamic thermal model that can achieve similar level of accuracy as traditional full-order 3D dynamic thermal conduction FEA, while being much faster to run as compared to the full-order model. Additionally, the CE model should be fast to generate, and not depend on system inputs or training data.

1.2.2 Electromagnetic Modeling

FEA has been widely used in EM modeling of electric machines for decades. Both magneto-static (MS) and magneto-quasistatic (MQS) FEA has been used in various applications. Both MS and MQS formulations are approximations to Maxwell's equations,

which are shown below:

$$\nabla \cdot \vec{D} = \rho, \tag{1.1}$$

$$\nabla \cdot \vec{B} = 0, \tag{1.2}$$

$$\nabla \times \vec{E} = -\frac{\partial \vec{B}}{\partial t}, \tag{1.3}$$

$$\nabla \times \vec{H} = \vec{J} + \frac{\partial \vec{D}}{\partial t}, \tag{1.4}$$

where $\vec{D}$ is electric flux density, ρ is free charge density, $\vec{B}$ is magnetic flux density, $\vec{E}$ is electric field intensity, $\vec{H}$ is magnetic field intensity, and $\vec{J}$ is electric current density. Equation (1.1) is Gauss's law, Equation (1.2) is Gauss's law for magnetism, Equation (1.3) is Faraday's law, and Equation (1.4) is Ampere's law.

By neglecting the effect of charge accumulation and displacement field, MQS formulations are derived:

$$\nabla \cdot \vec{D} = 0, \tag{1.5}$$

$$\nabla \cdot \vec{B} = 0, \tag{1.6}$$

$$\nabla \times \vec{E} = -\frac{\partial \vec{B}}{\partial t}, \tag{1.7}$$

$$\nabla \times \vec{H} = \vec{J}. \tag{1.8}$$

In the spacial and temporal scales of interest for electric machines, MQS is a good and accurate approximation to Maxwell's equations [24]. By further neglecting the dynamic effects in Faraday's law, MS formulations can be derived:

$$\nabla \cdot \vec{D} = 0, \tag{1.9}$$

$$\nabla \cdot \vec{B} = 0, \tag{1.10}$$

$$\nabla \times \vec{E} = 0, \tag{1.11}$$

$$\nabla \times \vec{H} = \vec{J}. \tag{1.12}$$

Table 1.1: Trade-offs between magneto-static and magneto-quasistatic FEA

Magnetostatic FEA	Magneto-quasistatic FEA
Fast to solve	Slow to solve
Position dependent	Time dependent
FEA results can be used for all rotor speeds	New solutions required for each speed
Cannot capture skin and proximity effect	Can capture skin and proximity effect
Over-estimates magnet losses	Accurate magnet losses
Suitable for powertrain-level optimization	Suitable for machine design optimization

MS formulations have been preferred in CE modeling due to the computational benefits gained at the cost of ignoring dynamic effects, thus lacking accuracy in loss estimation. A detailed comparison between MS and MQS formulations is shown in Table 1.1.

Due to the computational intensity involved in MQS FEA, CE EM models have mainly focused on utilizing MS formulations, for example, in [25–31]. In [27], two-dimensional (2D) nonlinear MS FEA was used for calculating the magnetic vector potential in the coils. By taking advantage of phase symmetry, only three MS FEA solutions, which correspond to three different rotor positions (one for each phase), are used to reconstruct the flux linkage waveform for each phase. Post-processing techniques and analytical relationships are then used to estimate the motor performance (i.e. torque, voltage, and core losses). Based on [27], Fourier analysis and space-time transformations were added to the CE-FEA model in [28] so the radial and tangential components of the flux density at any point in the stator core can be calculated. Based on [27, 28], Zhang et al. [30] proposed an analytical relationship to estimate the PM eddy-current losses by dividing the PM region into small blocks and using the flux density information in each block. T.J.E. Miller et al. [31] proposed to use a small set of 2D MS FEA solutions to build a flux-MMF diagram for fast calculation of average torque and inductances of the machine.

Although MS-based models suffer to some extent in the accuracy of loss calculation (AC winding loss and PM eddy-current loss), it can be useful in some applications, e.g., in machine design [32, 33], machine drives [34], and EV/HEV powertrain–level analysis

[35]. In EV/HEV powertrain–level simulation and optimization, torque–speed curves and efficiency maps of an electric machine design are a convenient tool to use [36–41]. An example map is shown in Fig. 1.2, where speed is shown in the x-axis, torque is shown in the y-axis, and efficiency level is shown by contour lines.

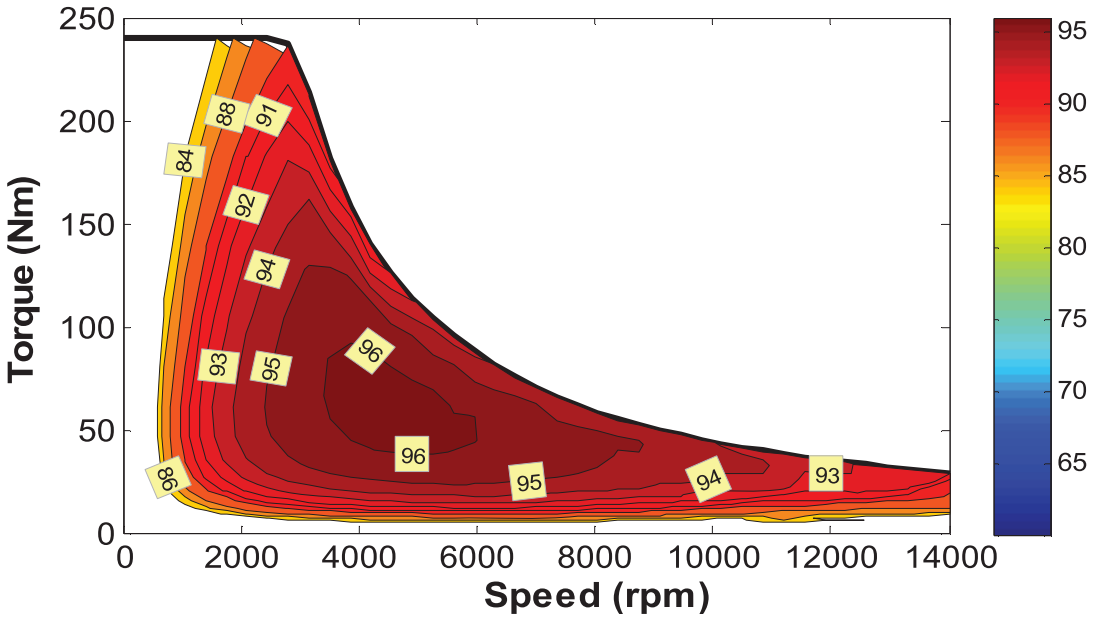

Figure 1.2: An example efficiency map of Toyota Prius motor, figure from [40].

Generating an accurate optimal efficiency map for a specific design using FEA is computationally intensive. Although simulating a single operating point of current magnitude, phase angle, and rotor position is usually fast, obtaining an average torque requires calculating multiple rotor positions in one period. Furthermore, to find the operating point with optimal efficiency for a given torque and speed combination requires simulating a large number of current magnitudes and phase angles to maximize efficiency while satisfying voltage constraints (the number of operating points that needs to be checked is even higher in the field weakening region). Multiplying this computation time for one torque and speed combination by the number of points in an efficiency map, such a process is computationally intensive and can take several core-hours. For example, as reported in [42], it takes 12 core-hours to simulate the efficiency map for a given design. This is very slow for

powertrain- or system-level design optimization purposes.

In addition to FEA simulations of the efficiency map for a given design, the ability to quickly generate and predict the performance of new electric machine designs is also crucial for EV/HEV powertrain–level design and optimization. To quickly generate new designs for given specifications, the idea of dimensional scaling has been discussed in [43–45]. However, dimensional scaling by itself is limited in terms of producing a sufficient set of machine designs and enough degrees of freedom for powertrain design and optimization.

In this dissertation, one of the objectives is to develop a toolkit that can 1) quickly generate machine designs based on an existing design with enough degrees of freedom through different scaling techniques; 2) quickly calculate the efficiency maps of these new designs. The process should be much faster than the traditional method of solving FEA for each individual operating point in efficiency map, to the extent that it is sufficiently fast to be integrated into a system– or powertrain–level simulation/optimization routine.

1.2.3 Electromagnetic-Thermal Coupled Analysis

Electromagnetic-thermal coupled analysis of electric machines has been reported in recent years [32,46–49]. The general process of EM-thermal coupled analysis is to start from an EM simulation that determines the torque, losses, and other quantities (e.g. flux linkage, voltage, flux density, field intensity, etc) for a given operating point. The losses are then fed into the thermal simulation to estimate temperature under such loss conditions. Since the material properties are temperature-dependent, they are updated according to the estimated temperature at the end of thermal simulation, and fed back to the EM simulation for another iteration. This iterative process stops when the temperatures converge. However, these papers all focus on component-level simulation and optimization, and are therefore not suitable for powertrain-level simulation due to computational constraints.

The temperature-dependent torque-speed curve was estimated by EM-thermal coupled analysis in [50], showing the impact of temperature rise on torque production. However,

using EM-thermal analysis in efficiency map estimation has not yet been reported in the literature. The efficiency map of an electric machine is constrained by temperature, since the torque capability and losses are both affected by temperature. Furthermore, the continuous operating region, which is defined as the operating points where the machine can safely run at steady state without hitting the temperature limit of the winding insulation and PM materials, can provide useful information for powertrain design and optimization. To predict the continuous operating region of an efficiency map, a thermal model is needed to couple with the EM model. Furthermore, an accurate prediction of demagnetization also requires temperature information in the PM [47], since the intrinsic coercivity of the PM material is affected by temperature.

In this dissertation, one of the objectives is to develop an EM-thermal coupled model that can be integrated into the efficiency map generation toolkit mentioned in Section 1.2.2, and provide the ability to quickly estimate the continuous operating region of the efficiency map.

1.3 Contributions and Dissertation Outline

The intellectual contributions of this dissertation are:

1. The application of orthogonal decomposition as a modal-based MOR technique, where only a small subset of eigenmodes need to be calculated, to a full-order 3D dynamic thermal FEA model of an electric machine to build a CE dynamic thermal model that is much faster than 3D FEA and sufficiently accurate.

2. The development of a "normalized extent of excitation" calculation that can automate the process of selecting the most significantly excited eigenmodes without the need of training data or iterative processes. Furthermore, the calculation does not depend on the system inputs by using normalized distribution vectors.

3. The development of a scalable 2D MS model that can be used to generate new machine designs using three independent scaling techniques. Moreover, the torque-speed curve and efficiency map of the scaled designs can be quickly estimated using pre-calculated base design FEA data, without the necessity of re-solving the FEA for these scaled designs.

4. The development of a EM-thermal coupled model by coupling the aforementioned scalable MS model with a 3D scalable static thermal model to estimate the continuous operating region of the scaled design directly using the pre-calculated base design thermal data, without the necessity of re-solving the coupled EM-thermal FEA for these scaled designs.

This dissertation is organized as follows:

- Chapter 1 has presented the background and motivation behind the proposed objectives of the dissertation, along with a detailed literature review. The objectives were presented, and the intellectual contributions have been highlighted.

- Chapter 2 will present the development of a *CE 3D FE-based dynamic thermal model of electric machines*, where eigenmode-based MOR techniques are used to generate a ROM. The process of building a full-order 3D FEA model is presented at first, followed by the MOR technique. Simulation results are presented to show that the ROM can dramatically reduce computation time while maintaining satisfactory accuracy comparing with the full-order model. Experimental results are shown to validate the model and the feasibility of using the proposed ROM for real-time operation.

- Chapter 3 will present a *CE 2D MS FE-based scalable model for electric machines* that is suitable for powertrain design optimization. Three independent scaling techniques are proposed to quickly generate new machine designs. The efficiency maps of the new designs can be efficiently calculated using a pre-determined FEA database,

without the necessity of re-solving FEA for the scaled designs. Results show that the torque-speed curve and the shape of the efficiency contour can be adjusted in a CE manner.

- Chapter 4 will present a *CE finite-element-based EM-thermal coupled scalable model of electric machines* that is scalable and suitable for fast temperature-dependent efficiency map generation and continuous operating region prediction. The scalable 2D MS model is coupled with a scalable 3D static thermal analysis and solved iteratively in the database generation process. After the database is generated, the efficiency map and the continuous operating region of the scaled designs can be calculated quickly.

- Chapter 5 will present the conclusion of the dissertation, along with some related future work.

CHAPTER 2

Computationally-Efficient Finite-element-based Dynamic Thermal Model of Electric Machines

2.1 Introduction

In this chapter, a 3D thermal FEA-based MOR technique is proposed for electric machines. A modal-based orthogonal decomposition method [51] is used to decompose the full-order FE model without the necessity of calculating all the eigenmodes of the 3D model. An automatic process based on a proposed "extent of excitation" calculation is used to select the eigenmodes that should be included in the reduced-order dynamic model. The selection process is not dependent on inputs, does not require training or iterative process. Finally, only specific temperatures are calculated to further reduce the size of the problem. Based on both simulation and experimental results, the proposed reduced-order model is shown to be both fast and accurate enough to be used as a real-time temperature monitor or in powertrain-level simulation and optimization of electric vehicles (EVs) and hybrid electric vehicles (HEVs).

2.2 Dynamic 3D Thermal Analysis

2.2.1 Conduction Heat Transfer

The partial differential equation (PDE) associated with thermal conduction is given as follows:

$$d\frac{\partial T}{\partial t} - \kappa\nabla^2 T = q_{loss}, \tag{2.1}$$

where T is the continuum temperature, and κ and d are the thermal conductivity and specific heat, respectively, of the machine materials, and q_{loss} represents heat generation inside the machine. Using finite element analysis techniques and considering convective heat transfer boundary conditions, the machine model is meshed and the above PDE can be discretized into an ordinary differential equation (ODE) as follows:

$$\mathbf{D}\dot{\vec{t}} + \mathbf{K}\vec{t} = \vec{q}, \tag{2.2}$$

where $\vec{t}$ is the nodal temperature vector of the finite element mesh, $\mathbf{K}$ is the finite element matrix which corresponds to thermal conductivity, and $\mathbf{D}$ is the finite element matrix which corresponds to specific heat. Both $\mathbf{K}$ and $\mathbf{D}$ are n-by-n symmetric matrices generated by the FEA assembly process, where n is the number of nodes in the 3D finite-element mesh. The vector $\vec{q}$ corresponds to the excitation/inputs of the thermal model, and can be categorized as follows:

$$\vec{q} = \sum_k P_k \vec{f_k} + \sum_l H_l \vec{g_l}. \tag{2.3}$$

The vectors $P_k\vec{f_k}$ correspond to different loss mechanisms of the machine, including conduction losses, core losses, permanent magnet (PM) losses, and friction and windage losses. The scalars P_k correspond to the total amount of loss, and the vectors $\vec{f_k}$ correspond

to the normalized spatial loss distribution in the machine. Each type of loss can be further broken down into sub-domains that have different loss density distributions. For example, the stator iron can be divided into the back-iron region, the tooth region, and the tooth-face region, with different core loss distribution assigned to each sub-domain. Thus, the resolution of the loss density distribution can be adjusted. Likewise, the vectors $H_l\vec{g}_l$ correspond to convective heat transfer on different boundaries of the machine, representing Neumann boundary conditions of the finite element model. The scalars H_l correspond to the heat flux density, and the vectors $\vec{g_l}$ correspond to the normalized heat flux distribution on the machine boundaries.

The thermal conductivity tensor of the stator slot region is calculated by using the rule-of-mixtures technique. As the slot region is a mixture of copper conductor and insulation, the equivalent thermal conductivity tensor can be calculated as follows:

$$[\kappa_{ij}] = \begin{bmatrix} \kappa_x & 0 & 0 \\ 0 & \kappa_y & 0 \\ 0 & 0 & \kappa_z \end{bmatrix}, \tag{2.4}$$

where

$$\kappa_x = \kappa_y = \frac{1}{\frac{f_s}{\kappa_{Cu}} + \frac{1-f_s}{\kappa_v}}, \tag{2.5}$$

$$\kappa_z = f_s\kappa_{Cu} + (1 - f_s)\kappa_v, \tag{2.6}$$

κ_x and κ_y are the thermal conductivity in the cross sectional plane, κ_z is the thermal conductivity in axial direction, f_s is the slot filling factor, and κ_{Cu} and κ_v are the thermal conductivity of copper and varnish, respectively.

2.2.2 Convection Cooling on Machine Boundaries

The convective excitation component in (2.3) can be used to simulate air and liquid cooling on any boundary of the machine (typically on the stator outer boundary and both ends of the machine). Newton's Law of Cooling is used to calculate the heat flux at the machine boundaries:

$$H_l = h_l(T_{cl} - T_{bl}), \tag{2.7}$$

where h_l is the heat transfer coefficient on the l-th convective boundary, T_{bl} is the temperature on the boundary, and T_{cl} is the coolant or ambient temperature. A convective Neumann boundary condition is then applied to the boundaries of the finite-element model. The heat transfer coefficient for air cooling or liquid cooling can be determined through empirical measurements or computational fluid dynamic (CFD) simulations.

2.2.3 Heat Transfer in the Air Gap

The stator and rotor finite element models are coupled at the air gap of the machine to capture the speed-dependent air gap heat transfer. Both conductive and convective heat transfer occurs in the air gap. In this chapter, this issue is addressed by modeling the air gap with an effective thermal conductivity which captures both conduction and convection.

In order to derive this effective conductivity, the stator and rotor are modeled as concentric rotating cylinders. The convection heat transfer between two rotating cylinders can be calculated using the dimensionless Reynolds number (R_e), Taylor number (T_a), and Nusselt number (N_u). The Reynolds and Taylor numbers are given in [52], and are repeated below:

$$R_e = \frac{g\omega_r r_r}{\nu},\ T_a = R_e\sqrt{\frac{g}{r_r}}, \tag{2.8}$$

where g is the length of air gap, ω_r is the rotational velocity of the rotor, r_r is the rotor radius, and ν is the kinematic viscosity of air. The Nusselt number can be then determined by the corresponding Taylor number [3, 52, 53]:

$$N_u = \begin{cases} 2.2, & T_a < 41, \\ 0.23 \times T_a^{0.63} \times P_r^{0.27}, & 41 \leq T_a \leq 100, \\ 0.425 \times T_a^{0.5} \times P_r^{0.27}, & T_a > 100, \end{cases} \tag{2.9}$$

where $P_r = \frac{\nu}{\alpha}$ is the Prandtl number and α is the thermal diffusivity of air. The convection heat transfer, which is determined by the Nusselt number, can be combined with the conductive heat transfer term in the heat transfer equation to form an effective thermal conductivity for both conductive and convective heat transfer [8]:

$$\kappa_{eq}\left(\omega_r\right) = \frac{N_u \kappa_{air}}{2}, \tag{2.10}$$

where κ_{air} is the thermal conductivity of still air.

Once the equivalent thermal conductivity is determined, we exploit the fact that the air gap is a cylindrical annulus, as shown in Fig. 2.1. Solving Laplace's equation, and assuming a uniform normal heat flux density H_g and temperature T_g at the air gap boundaries of the stator and rotor, we achieve the following heat flux/temperature relationship between the stator and rotor:

$$H_{sg} = \frac{\kappa_{eq}\left(\omega_r\right)}{r_{sg} \ln\left(\frac{r_{sg}}{r_{rg}}\right)} \left(T_{rg} - T_{sg}\right), \tag{2.11}$$

$$H_{rg} = \frac{\kappa_{eq}\left(\omega_r\right)}{r_{rg} \ln\left(\frac{r_{sg}}{r_{rg}}\right)} \left(T_{rg} - T_{sg}\right). \tag{2.12}$$

The air gap convective excitation vector for the stator and rotor $H_{ig}\vec{g}_{ig}$ can then be calculated and used in (2.3). The block diagram of the entire full-order thermal model is

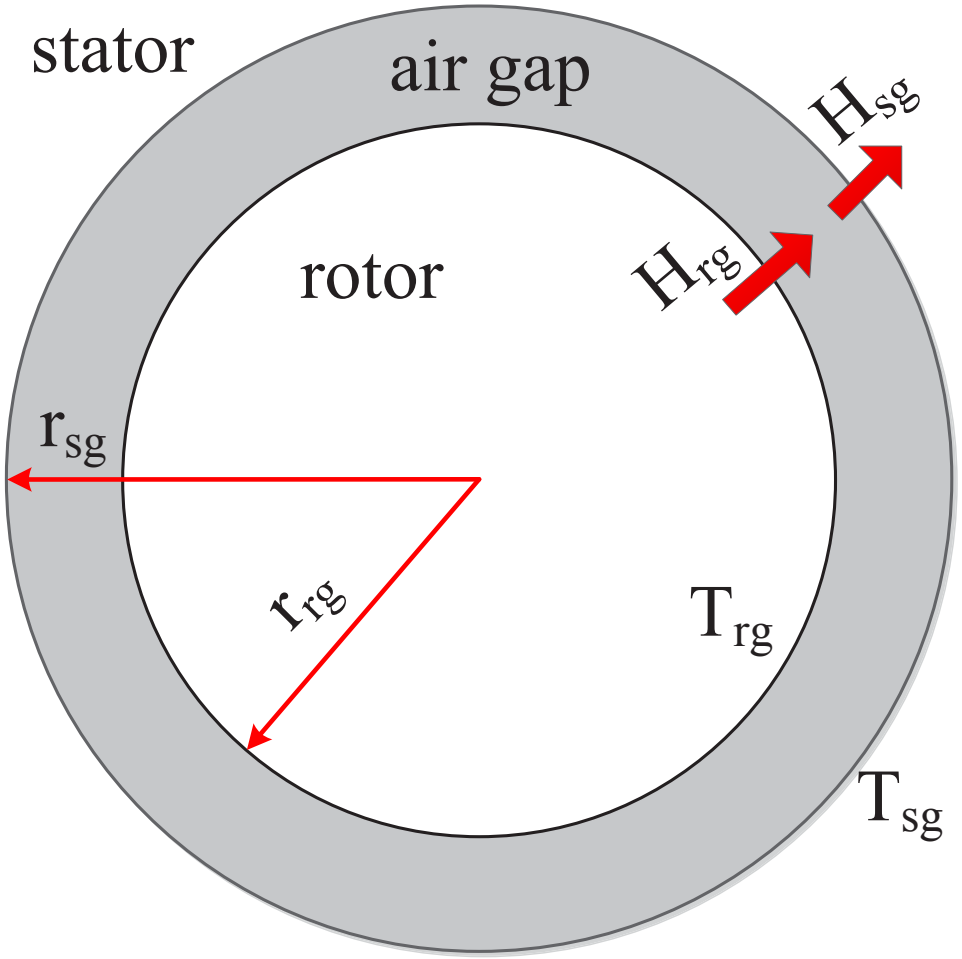

Figure 2.1: Flux relations for cylindrical annulus, representing the air gap.

shown in Fig. 2.2. The inputs to the model are coolant temperature, heat transfer coefficients, speed, and torque. The speed and torque are fed into a look-up table for calculating the losses in the machine. The look-up table can be built by either solving a corresponding electromagnetic FEA, or conducting experimental measurements. The losses and cooling conditions are then used in the stator and rotor thermal model, which are then coupled together using the air gap heat transfer relationship. The outputs of the model are temperatures in different locations inside the machine.

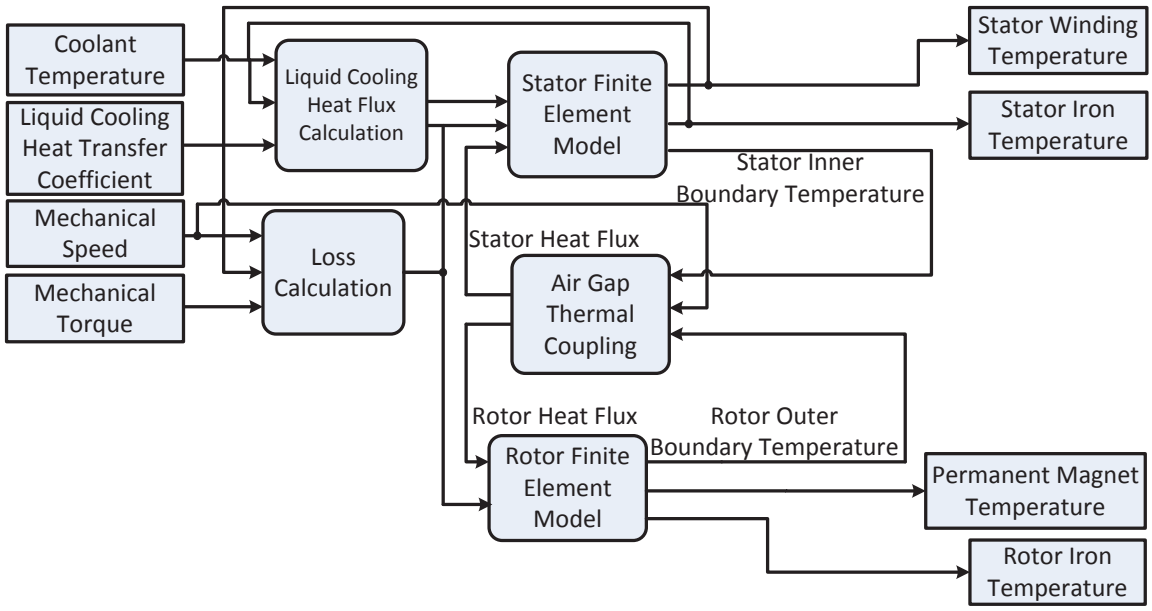

Figure 2.2: Block diagram of thermal model.

2.3 Model Order Reduction for 3D FEA Model

The order of the finite element model discussed in the previous section is now reduced. Two assumptions are made in the following analysis and results. First, the RMS line current is used to calculate conduction losses instead of the instantaneous current, as it is assumed that the oscillations in the instantaneous heat generation due to the time-varying current are sufficiently filtered by the thermal capacitance of the machine. This is valid when the

period of the current waveform is significantly smaller than the time constants associated with the thermal dynamics. By assuming this, the required time step length in the reduced-order model can be much larger than the period of the current, thus making the model more computationally efficient.

Second, the normalized loss distribution in the associated material is considered to be independent of frequency, i.e. the normalized loss distribution vector $\vec{f_k}$ in (2.3) is constant. This assumption simplifies the model-order-reduction process and reduces the size of the resulting model.

2.3.1 Decomposition of Dynamic and Static Eigenmodes

The proposed method is based upon the simulation of the eigenmodes of the dynamic thermal system as shown in (2.2). An eigenmode (or mode) is defined as an eigenvector $\vec{v_i}$ associated with an eigenvalue λ_i of (2.2) that satisfy the generalized eigenvector equation:

$$(\mathbf{K} - \lambda_i \mathbf{D})\vec{v_i} = 0. \tag{2.13}$$

This is similar to the concept of "modes" in structural dynamics, where the dynamic system is broken down into different modes that have different modal shapes and resonant frequencies. The difference is that the structural analysis is a second order system while the thermal conduction is a first-order system.

In previous work [23], in order to build a reduced-order model, all the eigenvectors of the 2D FEA model need to be calculated. However, this is computationally infeasible for a 3D model, which may contain millions of eigenvectors. To develop a computationally feasible model-order-reduction technique for 3D FEA, we take advantage of the orthogonality property of the eigenmodes of the real, symmetric matrices generated by FEA. Using the proposed technique, only a small subset of the eigenmodes need to be calculated.

As $\mathbf{K}$ and $\mathbf{D}$ are both n-by-n symmetric matrices generated by 3D FEA, they satisfy

the following orthogonality properties:

$$\vec{v}_i^T \mathbf{D} \vec{v}_j = \begin{cases} d_i, \ i = j \\ 0, \ i \neq j \end{cases}, \ \vec{v}_i^T \mathbf{K} \vec{v}_j = \begin{cases} k_i, \ i = j \\ 0, \ i \neq j \end{cases}. \tag{2.14}$$

Therefore, they can be diagonalized as follows:

$$\mathbf{V^T D V} = \mathbf{d} = \begin{bmatrix} d_1 & & & 0 \\ & d_2 & & \\ 0 & & ... & \\ & & & d_n \end{bmatrix}, \tag{2.15}$$

$$\mathbf{V^T K V} = \mathbf{k} = \begin{bmatrix} k_1 & & & 0 \\ & k_2 & & \\ 0 & & ... & \\ & & & k_n \end{bmatrix}. \tag{2.16}$$

We separate the eigenvectors into m "dynamic" and $(n-m)$ "static" vectors (to be defined later) [51]:

$$\begin{aligned} \mathbf{V} &= [\vec{v}_1 \quad \vec{v}_2 \quad ... \quad \vec{v}_m \, \vec{v}_{m+1} \quad \vec{v}_{m+2} \quad ... \quad \vec{v}_{n)}] \\ &= [\mathbf{V_d} \quad \mathbf{V_s}]. \end{aligned} \tag{2.17}$$

Thus,

$$\mathbf{V}_d{}^{\mathbf{T}}\mathbf{D}\mathbf{V}_d = \mathbf{d}_d = \begin{bmatrix} d_1 & & & 0 \\ & d_2 & & \\ & & \ddots & \\ 0 & & & d_m \end{bmatrix}, \tag{2.18}$$

$$\mathbf{V}_s{}^{\mathbf{T}}\mathbf{D}\mathbf{V}_s = \mathbf{d}_s = \begin{bmatrix} d_{m+1} & & & 0 \\ & d_{m+2} & & \\ & & \ddots & \\ 0 & & & d_n \end{bmatrix}. \tag{2.19}$$

The same relationship also holds for matrix $\mathbf{K}$: $\mathbf{V}_d^{\mathbf{T}}\mathbf{K}\mathbf{V}_d = \mathbf{k}_d$, $\mathbf{V}_s^{\mathbf{T}}\mathbf{K}\mathbf{V}_s = \mathbf{k}_s$, where $\mathbf{k}_d$ and $\mathbf{k}_s$ are diagonal matrices similar to $\mathbf{d}_d$ and $\mathbf{d}_s$. Thus, by using a change of basis $\vec{t} = \mathbf{V}\vec{x}$, (2.2) becomes

$$\mathbf{d}\dot{\vec{x}} + \mathbf{k}\vec{x} = \mathbf{V}^T\vec{q}. \tag{2.20}$$

To reduce the order of the dynamic system, the "static" eigenmodes are assumed to converge to their steady-state values instantaneously, i.e.:

$$\dot{x}_j = 0 \Rightarrow x_j = \frac{1}{k_j}\left(\vec{v}_j^T\vec{q}\right). \tag{2.21}$$

Thus,

$$\begin{aligned}
\vec{t} &= \mathbf{V}\vec{x} = \sum_{j=1}^{m} \vec{v}_j x_j + \sum_{j=m+1}^{n} \vec{v}_j x_j = \mathbf{V_d}\vec{x}_d + \sum_{j=m+1}^{n} \frac{1}{k_j}\vec{v}_j\vec{v}_j^{\mathrm{T}}\vec{q} \\
&= \mathbf{V_d}\vec{x}_d + \left(\sum_{j=1}^{n} \frac{1}{k_j}\vec{v}_j\vec{v}_j^{\mathrm{T}} - \sum_{j=1}^{m} \frac{1}{k_j}\vec{v}_j\vec{v}_j^{\mathrm{T}}\right)\vec{q} \\
&= \mathbf{V_d}\vec{x}_d + \left(\mathbf{V k^{-1} V^T} - \mathbf{V_d k_d^{-1} V_d^T}\right)\vec{q} \\
&= \mathbf{V_d}\vec{x}_d + \left(\mathbf{K^{-1}} - \mathbf{V_d k_d^{-1} V_d^T}\right)\vec{q}. \qquad (2.22)
\end{aligned}$$

By substituting (2.3) into (2.22), the temperature can be calculated as

$$\vec{t} = \mathbf{V_d}\vec{x}_d + \sum_k P_k\vec{u}_k + \sum_l H_l\vec{s}_l, \qquad (2.23)$$

where vectors $\vec{u}_k$ and $\vec{s}_l$ can be pre-calculated by performing matrix-vector solves:

$$\vec{u}_k = \left(\mathbf{K^{-1}} - \mathbf{V_d k_d^{-1} V_d^T}\right)\vec{f}_k, \qquad (2.24)$$

$$\vec{s}_l = \left(\mathbf{K^{-1}} - \mathbf{V_d k_d^{-1} V_d^T}\right)\vec{g}_l. \qquad (2.25)$$

By substituting (2.21) and (2.23) into (2.2), and left-multiplying the equation by $\mathbf{V_d^T}$, the dynamics of the reduced-order model are shown by

$$\mathbf{d}_d\dot{\vec{x}}_d + \mathbf{k}_d\vec{x}_d = \sum_k P_k\vec{f}_{v,k} + \sum_l H_l\vec{g}_{v,l}, \qquad (2.26)$$

where vectors $\vec{f}_{v,k} = \mathbf{V_d^T}\vec{f}_k$ and $\vec{g}_{v,l} = \mathbf{V_d^T}\vec{g}_l$ can also be pre-calculated. Since $\mathbf{d}_d$ and $\mathbf{k}_d$ are both diagonal matrices, all the "dynamic" eigenmodes are decoupled and can be simulated separately. This results in a collection of first-order differential equations.

In this approach, instead of calculating all the eigenmodes of the huge 3D FEA problem, we only need to calculate a subset of eigenmodes, in order of decreasing time constant, to determine the modes that should be modeled dynamically. This can be done by using MAT-

LAB's built-in function "*eigs*", which is efficient at calculating the generalized eigenvector problem for sparse matrices.

2.3.2 Dynamic Eigenmodes Selection

To decompose the system, the most significantly excited eigenmodes are considered as dynamic modes. To select the eigenmodes, the extent of excitation of the i-th eigenmode for each type of excitation is calculated:

$$E_i = \begin{cases} \tau_i \vec{v}_i^T \vec{f}_k & \text{(for losses)} \\ \tau_i \vec{v}_i^T \vec{g}_l & \text{(for boundary heat transfer)} \end{cases}, \tag{2.27}$$

where $\tau_i = \frac{1}{\lambda_i} = \frac{d_i}{k_i}$ is the time constant associated with the i-th eigenmode. The time-constant term in (2.27) is used to increase the weights of slower eigenmodes, as the system response of interest is mainly governed by the slowest eigenmodes. The extent of excitation for each type of excitation (loss or boundary heat transfer) is then normalized for comparison:

$$E_{i,norm} = \frac{E_i}{\max\limits_{j=1...k,1...l}(E_j)}, \tag{2.28}$$

In this way, the extent of excitation of each eigenmode does not depend on specific system inputs P_k and H_l. And the process of normalization allows a fair comparison between different type of excitations. To select the eigenmodes that need to be modeled as dynamic states, a threshold is set and the eigenmodes that have at least one extent of excitation that exceeds the threshold value are selected as the dynamic modes. This is an advantage over previous techniques that depend on system inputs [23], where the selected eigenmodes may not accurately model the dynamics due to overshadowed excitations.

In practice, users can either select the number of dynamic states they would like to

include in the reduced-order model, or specify a threshold value. The algorithm will then automatically generate a reduced-order model. We also note that by calculating the extent of excitation separately for each type of excitation, the dynamic modes selection process is general and does not depend on specific loss/cooling inputs.

The flowchart of the eigenmode selection process is shown in Fig. 2.3. For example, a full-order 3D FEA may contain 10^5 dynamic states. By only calculating the 50 slowest eigenvectors of the full-order model, and comparing their extents of excitation with the threshold value, 11 eigenmodes that are significantly excited can be selected as dynamic modes. The other 39 slow eigenmodes that are weakly excited or unexcited, along with the 99950 fast eigenmodes that are not calculated, are considered as static modes. Thus, the number of dynamic states can be greatly reduced in the reduced-order model.

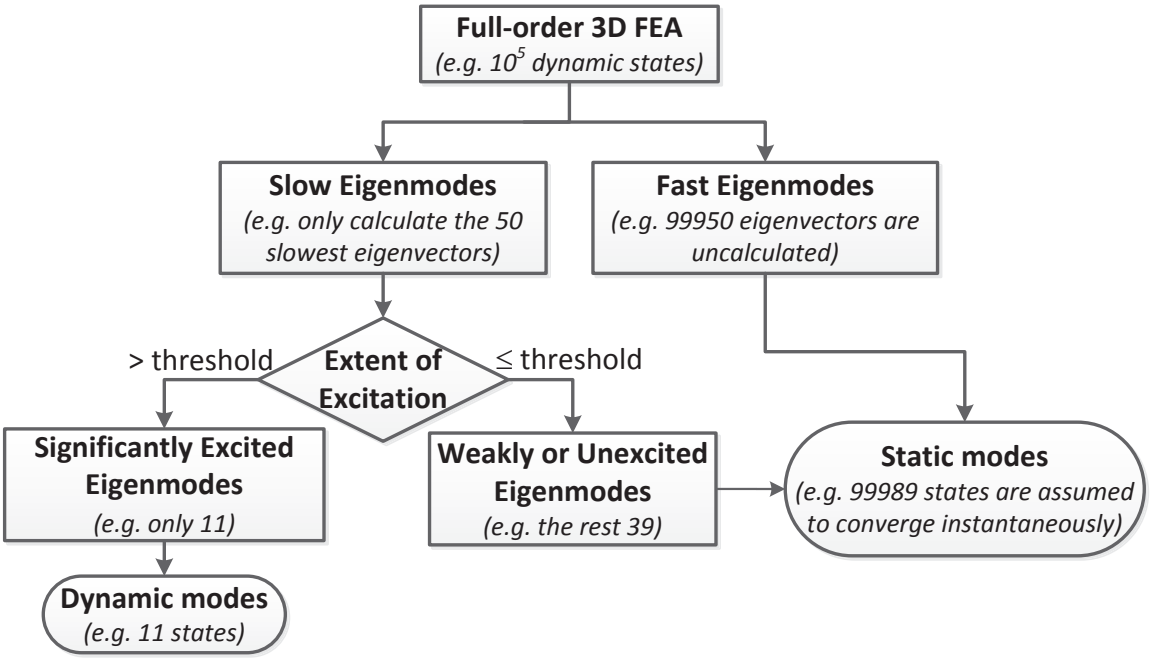

Figure 2.3: Eigenmode selection process.

2.3.3 Efficient Temperature Calculation

In practice, we are only interested in a few "hot spot" temperatures of the machine, either in the regions that are usually hottest (e.g. the center region of each slot and permanent magnets), or the nodal temperatures that correspond to the physical location of the temperature sensor to simulate the actual temperature measurement. Therefore, we only calculate the values of a small subset of nodal temperatures $\vec{t}_{hs}$. The i-th hot spot temperature t_{hsi} (i.e. the i-th element of $\vec{t}_{hs}$) that corresponds to the j-th node in the global finite element mesh is calculated as follows based on (2.23):

$$t_{hsi} \quad = \quad \vec{v}_{dj}^{T}\vec{x}_d + t_{ej}, \tag{2.29}$$

where $\vec{v}_{dj}^{T}$ is the j-th row of matrix $\mathbf{V_d}$ in (2.23), and t_{ej} is the j-th element of vector $\vec{t}_e = \sum_k P_k\vec{u}_k + \sum_l H_l\vec{s}_l$ in (2.23).

Furthermore, (2.29) also allows fast calculation of the average temperature of a boundary or a set of nodal temperatures inside the machine by using an n-by-1 averaging vector $\vec{m}_{avg}$, whose i-th element is

$$m_{avg,i} = \begin{cases} \frac{1}{N_{hs}}, & i = j \\ 0, & i \neq j \end{cases}, \tag{2.30}$$

where j is the global identification number of a node in the set and N_{hs} is the total number of nodes in the set. The average temperature of the set is then given by

$$t_{avg} \quad = \quad \vec{m}_{avg}^{T}\mathbf{V_d}\vec{x}_d + \sum_k \vec{m}_{avg}^{T}\vec{u}_k P_k + \sum_l \vec{m}_{avg}^{T}\vec{s}_l H_l, \tag{2.31}$$

where vector $\vec{m}_{avg}^{T}\mathbf{V_d}$ and scalars $\vec{m}_{avg}^{T}\vec{u}_k$ and $\vec{m}_{avg}^{T}\vec{s}_l$ can be pre-calculated.

The final state-space representation of the proposed reduced-order model is then given by (2.26), (2.29), and (2.31). Note that in these equations, only m-by-m diagonal matrices,

m-by-1 vectors, and scalars are involved. Thus, by using the above model-order-reduction techniques, the size of the resulting reduced-order model is dramatically smaller than that of the full-order model. It requires a significantly smaller number of calculations compared with the full-order model and thus being much faster to solve. For example, a full-order 3D machine model may contain on the order of 10^5 to 10^6 dynamic states. As will be seen, by using the proposed techniques it can be reduced to a model with approximately 10 dynamic eigenmodes ($m \approx 10$) while maintaining satisfactory accuracy.

2.4 Simulation

2.4.1 Model Construction

A 145kW, 400N-m (peak), liquid-cooled PMSM from UQM Technologies [54], which is suitable for use in vehicle propulsion, is used as our example. Its 3D geometry is shown in Fig. 2.4. Based on the above methodology, a full-order thermal FEA solver and a reduced-order thermal model have been implemented for the PMSM in MATLAB. The 3D dynamic finite element thermal model of the PMSM was built by visual inspection, a set of simple tests, and material properties from previous publications.

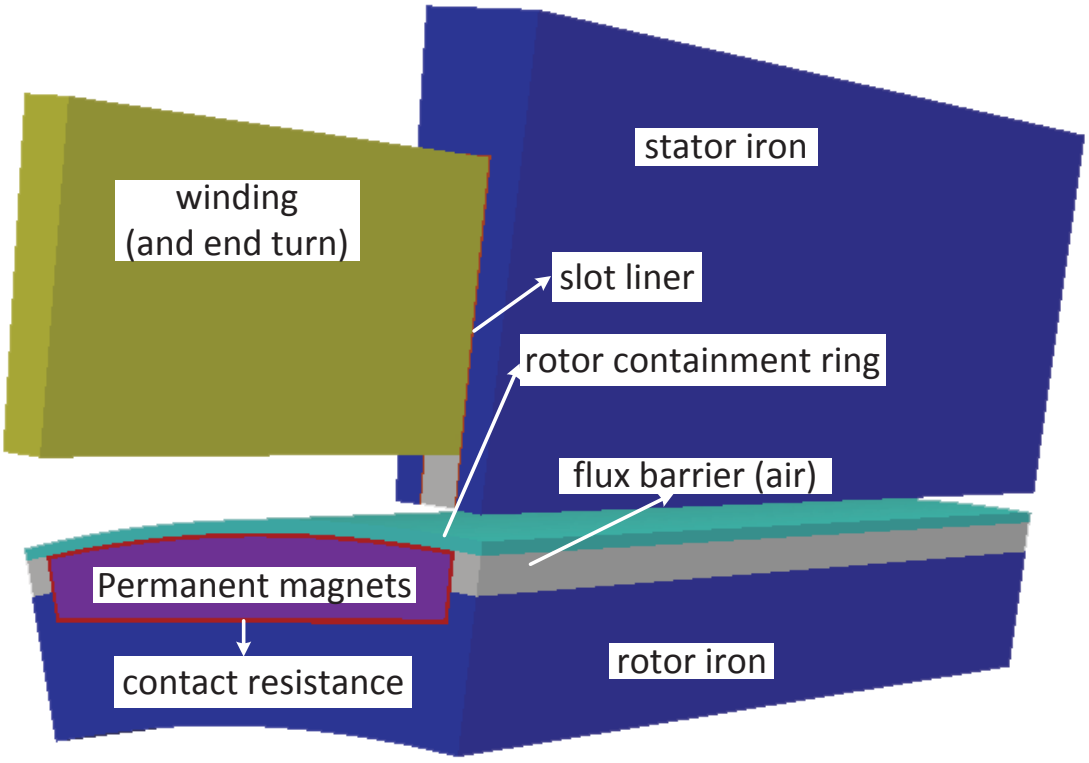

Figure 2.4: 3D geometry of a PMSM.

Table 2.1: Material properties and thermal parameters used in the simulation

Material	$\kappa(\mathrm{W}/(\mathrm{m}\cdot\mathrm{K}))$	$\rho(\mathrm{kg}/\mathrm{m}^3)$	$c(\mathrm{J}/(\mathrm{kg}\cdot\mathrm{K}))$
Iron stack [8] (cross-section direction)	20	7600	447
Iron stack [8] (axial direction)	3.4	7600	447
Copper [8]	390	8900	383
Insulation [8]	0.175	1100	1500
Magnets [8]	9	7600	440
Still air	0.025	1.2	1007
Slot liner [7]	0.076	2150	1172
Rotor containment ring (steel)	50	7874	460
Rotor iron-PM contact resistance (tuned using step response)	3.1e-3	1.2	1007
Liquid Convection Cooling	$1000\mathrm{W}/(\mathrm{m}^2\cdot\mathrm{K})$		
Natural Convection Cooling (end turn)	$3.5\mathrm{W}/(\mathrm{m}^2\cdot\mathrm{K})$		
Natural Convection Cooling (rotor end)	$7\mathrm{W}/(\mathrm{m}^2\cdot\mathrm{K})$		

The material properties (thermal conductivity κ, density ρ, and specific heat c) and thermal parameters used in the simulation are shown in Table 2.1. The heat transfer coefficient of the natural convection cooling was determined by using an Omega HFS-3 heat flux sensor. The heat transfer coefficient of the stator end turn is considered to be half of the measured natural convection heat transfer coefficient in the actual machine, since about half of the area of the end turn region is covered. The heat transfer coefficient of the liquid cooling is determined by a set of steady-state tests. We note that the material properties and thermal parameters listed in Table 2.1 were not tuned, except for the thermal conductivity of the contact resistance layer between the rotor iron and the PM. Due to the inherent difficulty in determining the thermal conductivity of the contact resistance layer, it was tuned using an optimization routine which minimizes the RMS error between the measured and simulated PM temperature waveforms in a step response test with $I_{amp} = 200$A (more details can be found in Section 2.5). After this optimal thermal conductivity was found, it was used in all the simulations presented in this chapter.

In the simulations, winding conduction losses, stator core losses, rotor core losses, and PM eddy current losses in the thermal simulation are determined at each machine operating point by a corresponding 2D nonlinear electromagnetic time-domain steady-state FEA [55], where an entire pole of the machine is modeled. The average loss density in each region is then calculated assuming a uniform distribution. The losses and boundary heat transfers are assumed to be identical for each tooth-slot pair in the stator, and for each pole in the rotor. Thus, only one tooth-slot pair in the stator and one pole in the rotor needs to be modeled in the simulations.

One nodal temperature in the end turn region and one in the PM region are used in the reduced-order model. The location of the hotspots in the FE mesh correspond to the actual location of the temperature sensors in the experimental setup. In addition, two average temperature calculations, as presented in (2.31), are needed to determine the average air-gap boundary temperature for the stator and rotor for the air-gap heat transfer calculation.

Thus, there are two hotspot calculations for the stator and rotor model, respectively.

The detailed steps for the reduced-order model construction are listed as follows. First, the 3D machine geometry is drawn and meshed in COMSOL Multiphysics. Second, the finite element mesh is imported into MATLAB using COMSOL LiveLink for MATLAB. Third, the full-order finite element model is assembled in MATLAB. Fourth, a small subset of eigenmodes is calculated in order of decreasing time constant using the full-order finite element matrices, and their extent of excitation is calculated using (2.27). The eigenmodes chosen to be modeled as dynamic modes are selected based on the threshold value, as described in Section 2.3.2. Finally, the reduced-order model is generated.

2.4.2 Extent of Excitation Calculation

By using the proposed normalized extent of excitation calculation method in Section 2.3.2, the normalized extents of excitation of the slowest 20 eigenmodes in the stator and 10 eigenmodes in the rotor of the PMSM were calculated, and are shown in Figs. 2.5 and 2.6, respectively. Note that the y-axis of these two figures are abbreviated for better display, since the slowest eigenmodes in the stator and rotor have a much longer time constant, and thus a much larger extent of excitation in (2.27), than those of the other eigenmodes. As can be seen from Figs. 2.5 and 2.6, only a relatively small subset of the eigenmodes are significantly excited for each type of excitation and therefore need to be included in the dynamic portion. Examples of a significantly-excited stator eigenmode (Eigenmode #2) and an unexcited mode (Eigenmode #5) are shown in Figs. 2.7 and 2.8. A significantly-excited rotor eigenmode (Eigenmode #2) and a weakly-excited mode (Eigenmode #5) are shown in Figs. 2.9 and 2.10. For Stator Eigenmode #2, the largest extent of excitation (0.29) is due to end cooling, as can be verified by the mode pattern in Fig. 2.7. For Rotor Eigenmode #2, large extent of excitation is observed from the containment ring loss and air gap cooling, as can be verified by the mode pattern in Fig. 2.9.

To illustrate the dynamic eigenmodes selection process, a threshold of 0.06 is set for

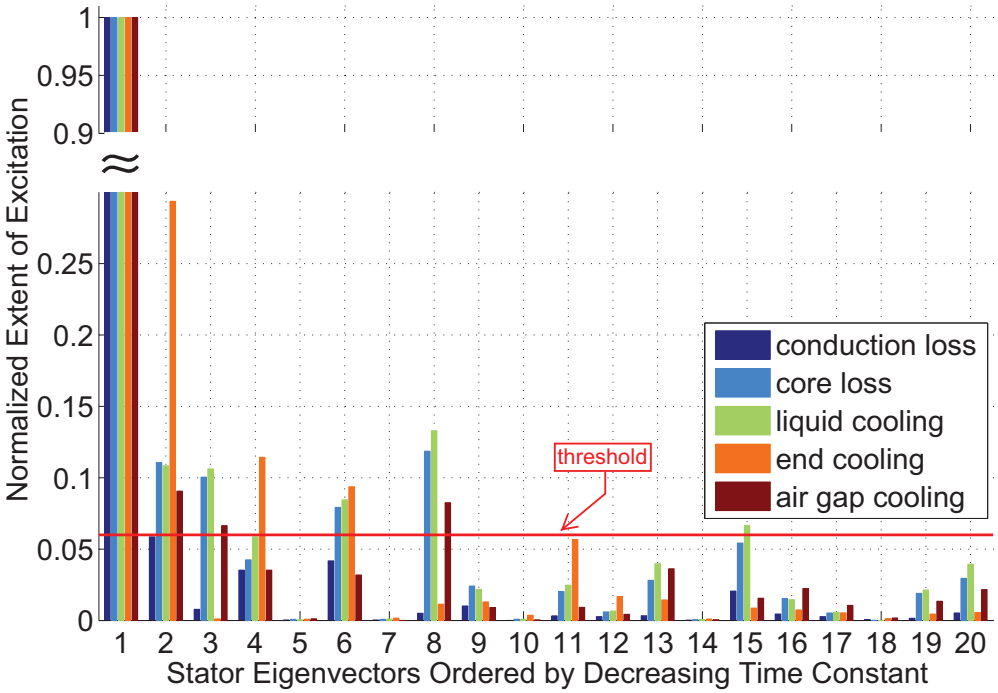

Figure 2.5: Normalized extent of excitation of stator (zoomed-in at y-axis).

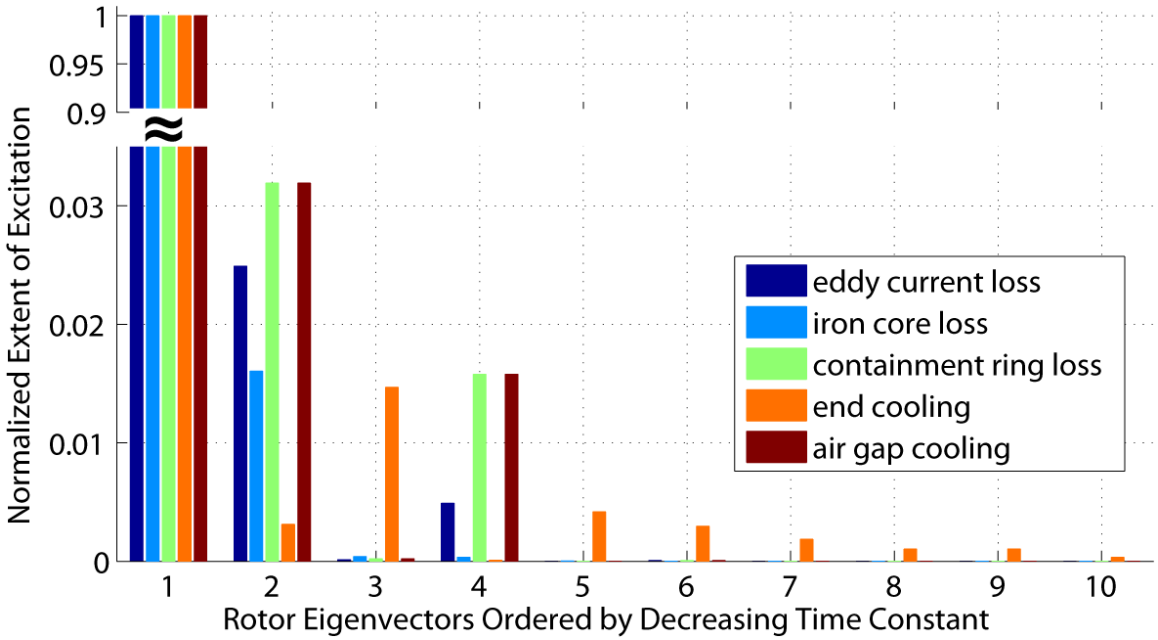

Figure 2.6: Normalized extent of excitation of rotor (zoomed-in at y-axis).

Fig. 2.5 as an example. By using this threshold value, the 1st, 2nd, 3rd, 4th, 6th, 8th, and 15th eigenmodes will be chosen as dynamic modes and result in a 7th-order model for the stator. Thus, by adjusting the threshold value, the number of dynamic states included in the reduced-order model can be automatically adjusted.

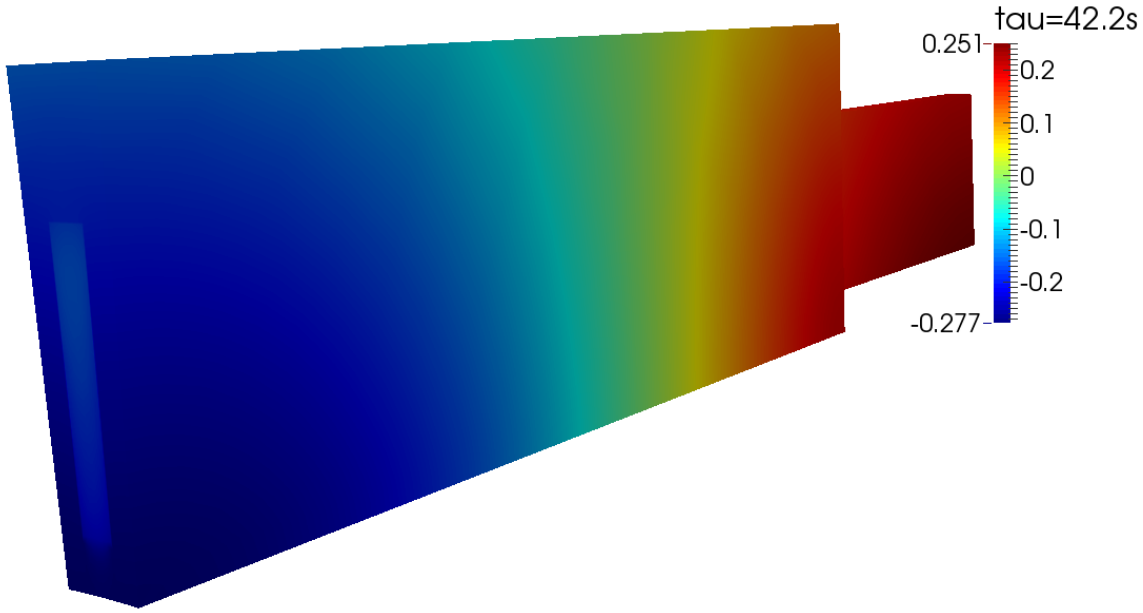

Figure 2.7: Stator tooth-slot pair Eigenmode #2 (significantly excited), τ=42.2sec. For this mode, the largest extent of excitation is due to end cooling, as can be seen from the mode pattern in this plot.

2.4.3 Simulation Results

By using the proposed techniques, a reduced-order model is built from the full-order finite element model of the machine. The simulation results of a step response and a real-life driving cycle are shown in this section. In this section, both the full-order and the reduced-order model used implicit Trapezoidal integration [56, p. 46] with a 1sec time step length. To allow a fair comparison, Cholesky factorization with a permutation matrix was pre-calculated for the full-order model to accelerate the solving process. In the following discussions, the "simulation time" refers to the time span of the simulation, while the computation time refers to the amount of CPU time the simulation takes to run. All the

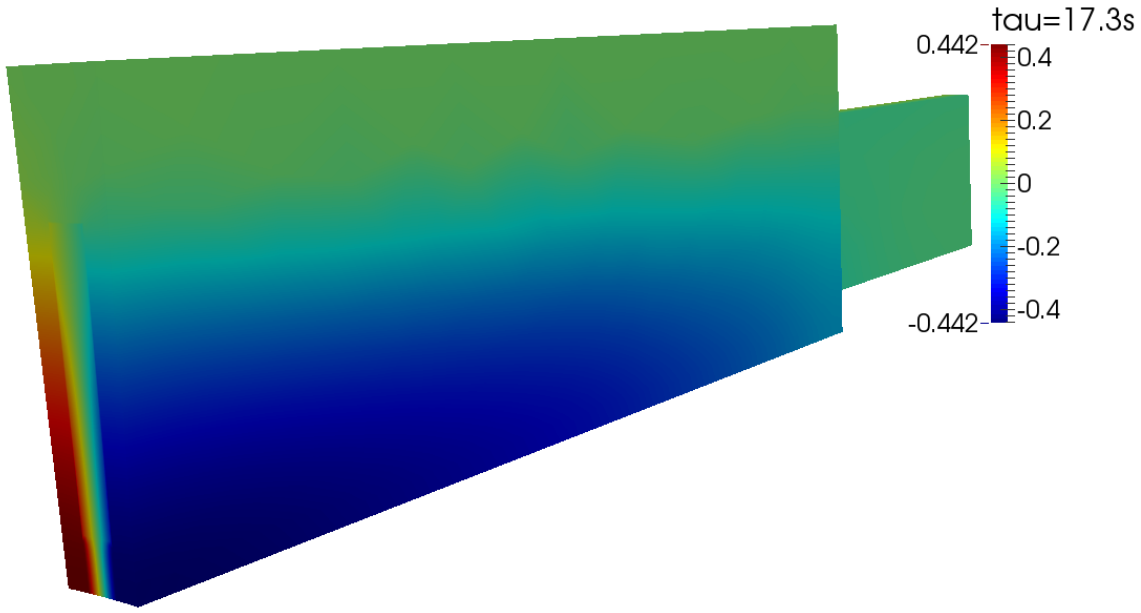

Figure 2.8: Stator tooth-slot pair Eigenmode #5 (unexcited), τ=17.3sec.

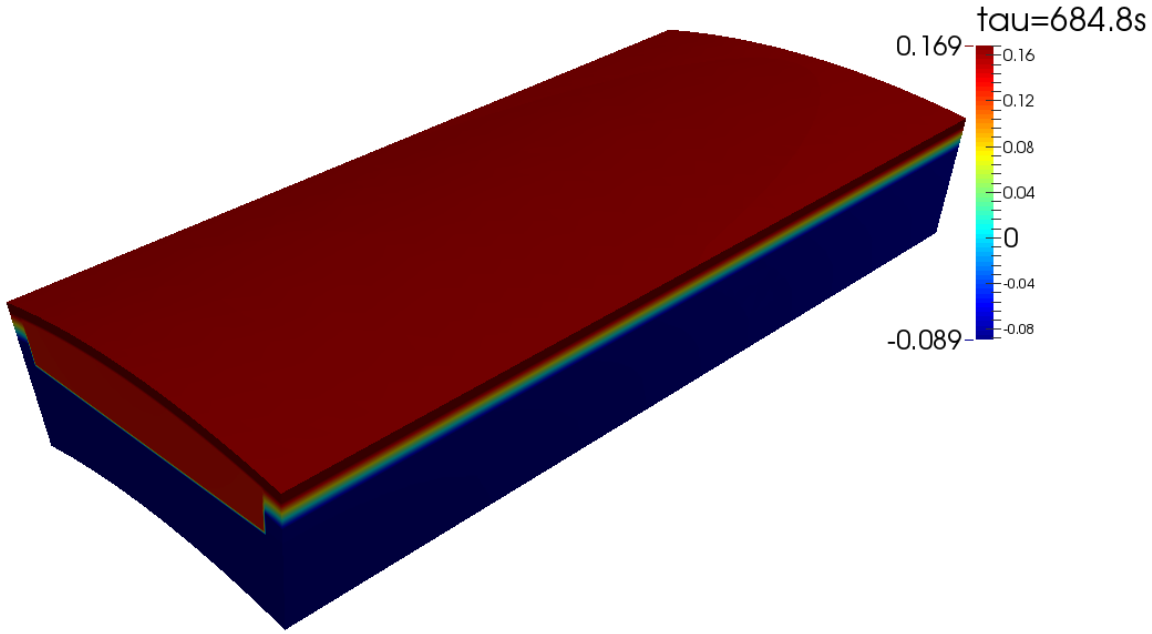

Figure 2.9: Rotor pole Eigenmode #2 (significantly excited), τ=684.8sec. For this mode, the largest extent of excitation is due to containment ring loss and air gap cooling, as can be seen from the mode pattern in the plot.

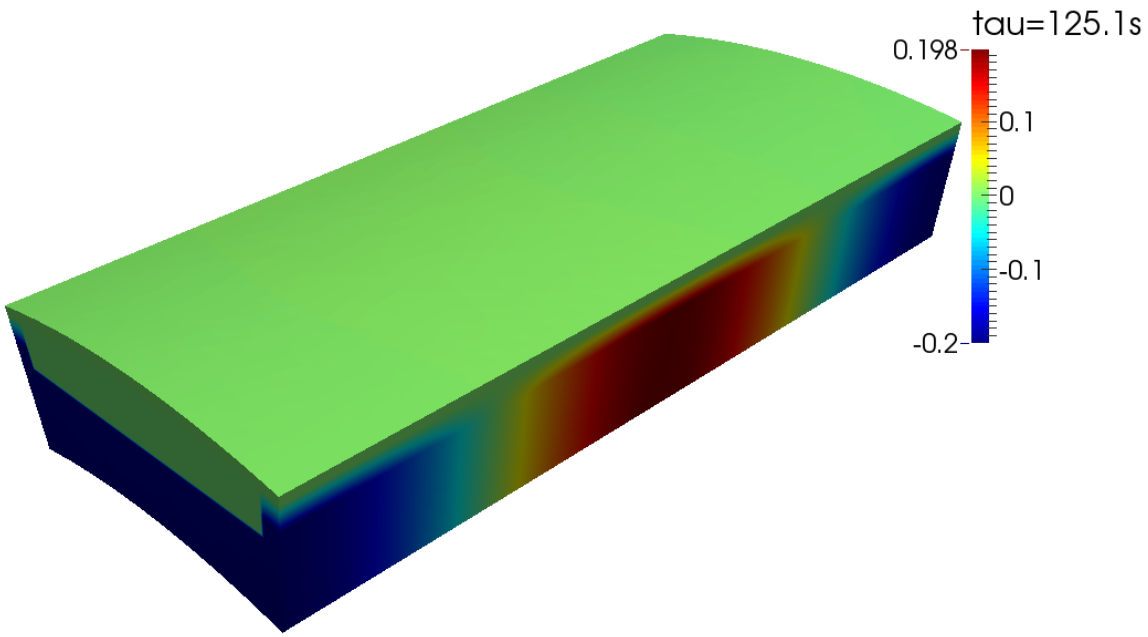

Figure 2.10: Rotor pole Eigenmode #5 (weakly excited), τ=125.1sec.

simulations were conducted on a workstation with an Intel Xeon X2350 dual-core CPU operating at 2.67GHz.

2.4.3.1 Step Response

The step response due to a step in torque command at 4000RPM and 350N-m is simulated by the full-order model and a variety of reduced-order models that contain different numbers of dynamic states. The results are shown in Fig. 2.11 and Table 2.2. As can be seen from the table, the accuracy of the reduced-order model is improved by increasing the number of dynamic eigenmodes included. A trade-off can therefore be made between accuracy and the number of states (and therefore computation time) by the users, depending on their specific requirements. By using a 7+4-order reduced model (7 dynamic states in the stator, 4 dynamic states in the rotor), the error remains less than 0.23°C and 0.13°C for stator and rotor for the entire time span. Note that the "jump" at $t = 0$ in the lower-order models is due to the assumption that the static eigenmodes in the reduced-order models instantaneously converge to their quasi-steady-state values.

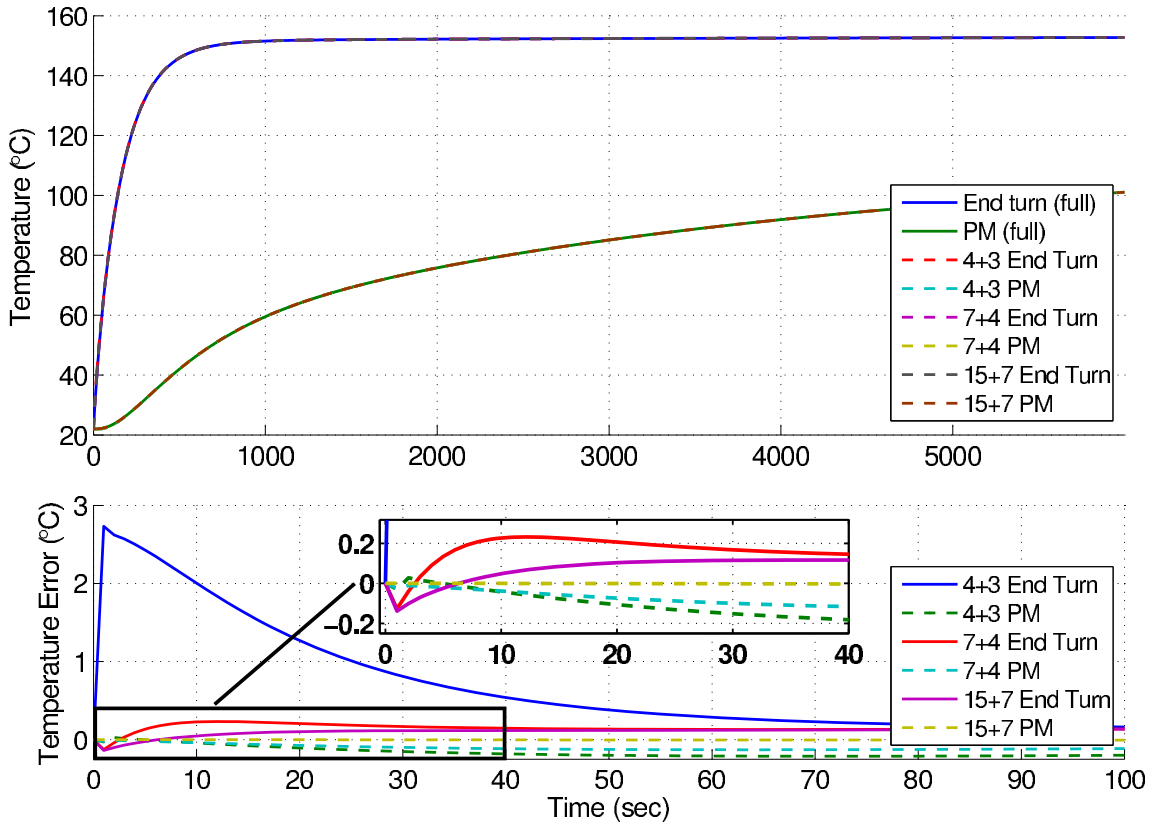

Figure 2.11: Step response temperature comparison @ 4000RPM, 350N-m for "x" stator + "y" rotor states in the reduced-order model.

Table 2.2: Error of various reduced-order models in the step response

# of States (Stator+Rotor)	Max. Error(°C) Stator	Rotor	Max. Relative Error Stator	Rotor
4+3	2.73	0.21	11.89%	0.94%
7+4	0.23	0.13	0.72%	0.58%
15+7	0.14	0.02	0.60%	0.04%
25+10	0.07	0.01	0.18%	0.02%

2.4.3.2 Driving Cycle Simulation

The internal temperatures of the machine have also been simulated during typical driving cycles. The speed and torque commands of an example driving cycle are shown in Fig. 2.12. The driving cycle shown in Fig. 2.12 is simulated using the full-order model and the 7+4-order reduced model. The simulation time is 1300sec. The temperature response and temperature error for the driving cycle simulation is shown in Fig. 2.13. As can be seen from the figure, the maximum error is less than 0.94°C (stator) and 0.07°C (rotor) for the entire time span, and all the transient responses are captured with sufficient accuracy. A detailed comparison of the two models is shown in Table 2.3. As can be seen from Table 2.3, the size of the problem is reduced from 103.9k states and 103.9k nodes to 11 states and 4 temperature calculations, which reduces the computation time by over 4 orders of magnitude. It takes only 16.8 milliseconds to simulate a driving cycle from 0 to 1300sec for the reduced-order model, while it takes 219.8 seconds to simulate the full-order model.

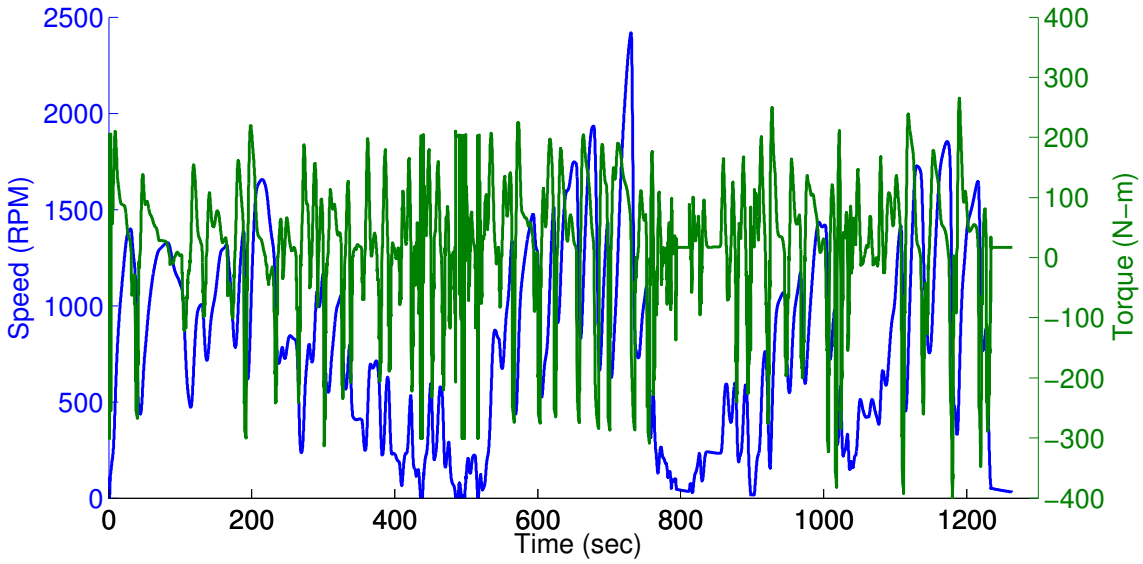

Figure 2.12: An example driving cycle for HEV simulation.

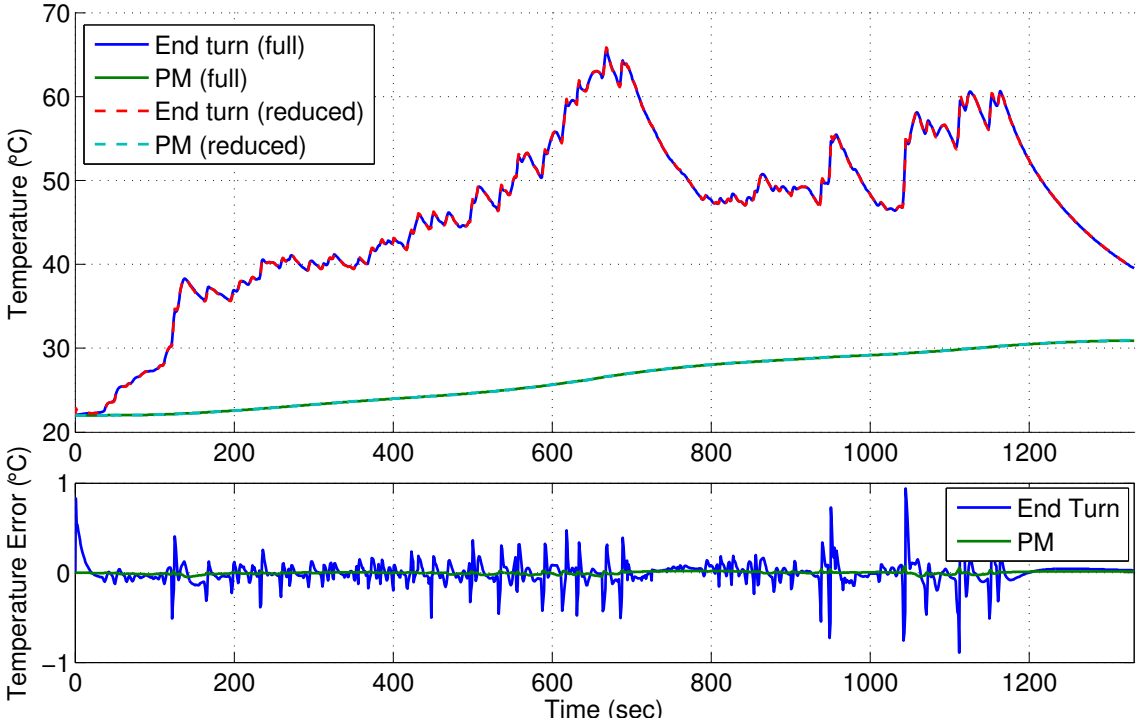

Figure 2.13: Temperature and temperature error for driving cycle simulation by using a reduced-order model with 7 stator and 4 rotor states.

Table 2.3: Comparison of full- and reduced-order models for simulating a driving cycle

	# of States	# of Nodal Temperatures	Computation Time	Max Error(°C) Stator	Rotor
Full	52.2k+51.7k	52.2k+51.7k	219.8s	N/A	N/A
Reduced	7+4	2+2	16.8ms	0.94	0.07

2.4.4 CE Sensitivity Analysis

The reduced order model also allows much faster thermal sensitivity analysis, which can provide useful insights for electric machine thermal and cooling system design. The differential sensitivity of a given thermal parameter or material property to the peak temperature during a driving cycle can be calculated as

$$S_p = \frac{\Delta T_{max}}{\Delta p} \frac{p}{T_{max}}, \tag{2.32}$$

where p is a thermal parameter or material property, T_{max} is the peak temperature during a driving cycle, Δp is a small variation in p around the nominal parameter/material property, and ΔT_{max} is the resulting change in peak temperature.

As an example, differential sensitivity analysis on both thermal parameters (e.g. coolant temperature, liquid cooling heat transfer coefficient, air cooling heat transfer coefficient, and initial conditions) and material properties (e.g. thermal conductivity of copper, iron, magnets, varnish, and slot liner) were conducted for UQM PowerPhase 145, and the results are shown in Figs. 2.14 and 2.15.

As can be seen in Fig. 2.14, for the UQM machine used in the simulation, both stator and rotor peak temperature are very sensitive to the coolant temperature, which matches the intuition that majority of the heat is removed through liquid cooling. As can be seen in Fig. 2.15, for the UQM machine used in the simulation, stator peak temperature is very sensitive to the thermal conductivity of the varnish, since it is much smaller than the thermal conductivity of copper and has a huge effect in the Rule-of-Mixture calculation (2.5). For rotor, the peak temperature is very sensitive to the thermal conductivity of lamination.

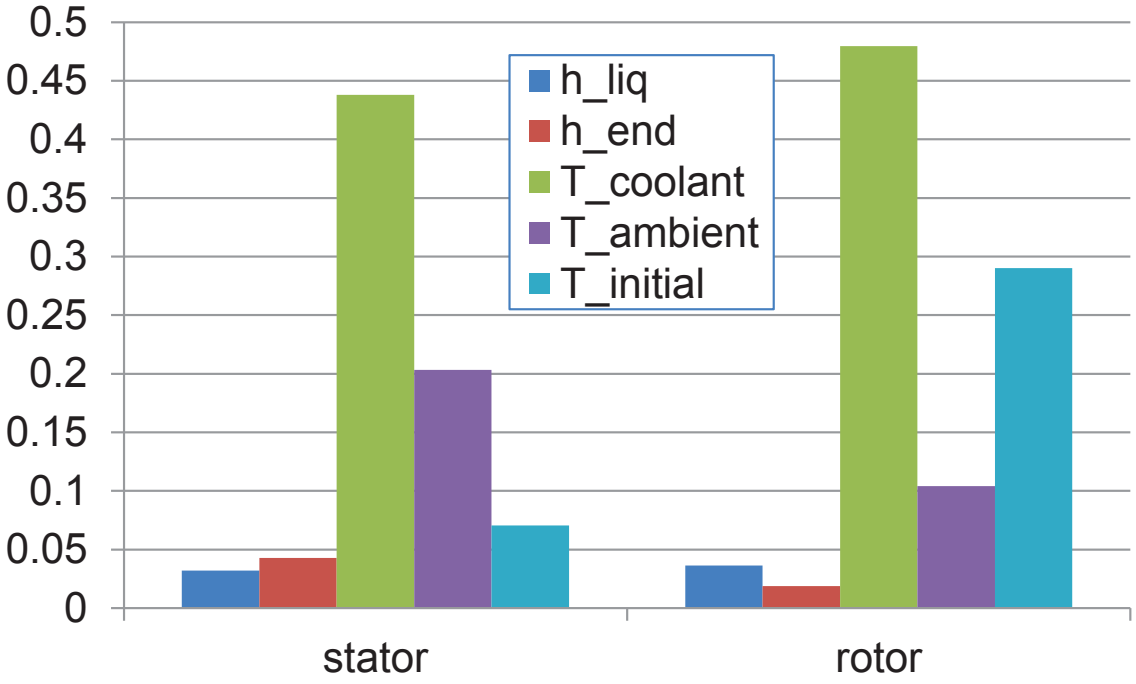

Figure 2.14: Differential sensitivities for thermal parameters.

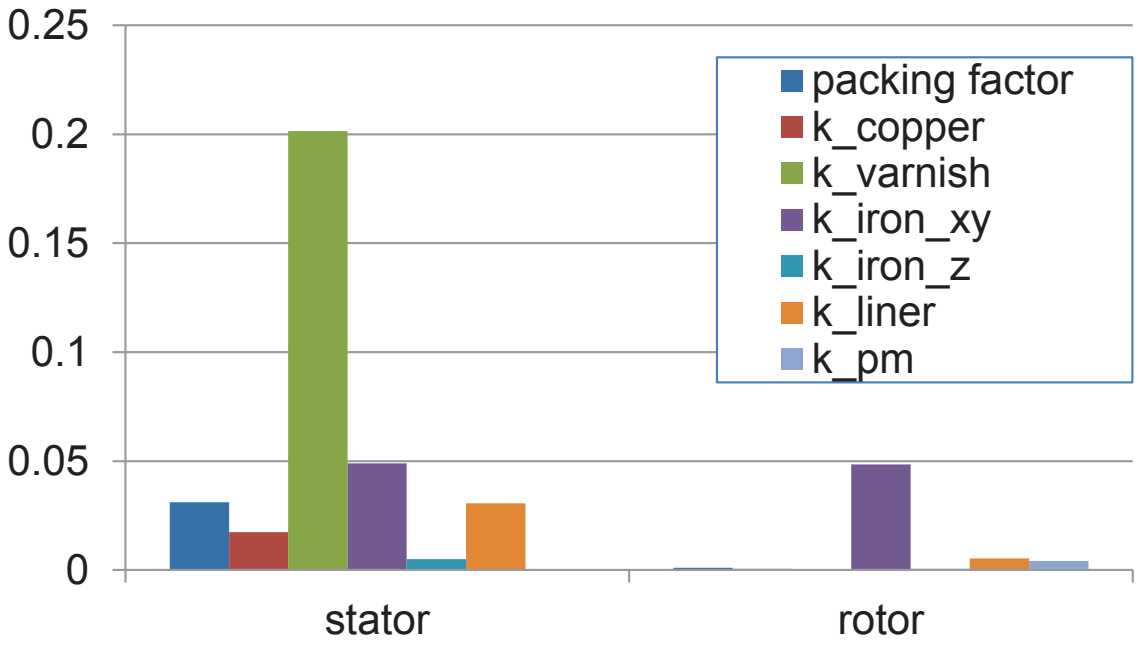

Figure 2.15: Differential sensitivities for material properties.

2.5 Experimental Validation

As shown in Section 2.4.3, the reduced-order model results match well with those of the full-order FEA model, and there exists a trade-off between accuracy and computation time that can be adjusted by the number of dynamic states included in the reduced-order model. In this section, a realistic benchmark case is used to test the reduced-order model, and to illustrate the potential of using the reduced-order model in real-time operations. We note that the experimental results presented in this section are solely for reference purposes, since the reduced-order model converges to the full-order model as the number of states increases, and thus is unrelated to the error between the full-order model and experimental results.

A test setup was constructed which consists of a UQM PowerPhase145 145kW PMSM, a three-phase rectifier, a 600A/1200V 3-phase IGBT inverter, and corresponding cooling systems. PT100 Resistance Temperature Detectors (RTDs) from Omega were used to measure the temperatures of the stator end-turn, inlet coolant, and outlet coolant. A Texense IRN2 infrared sensor, which is mounted on the end cap of the machine and pointing at the permanent magnets, is used to measure the PM temperature. The locations of the RTDs and the infrared sensor are shown Fig. 2.16. In the experiments, coolant and ambient temperatures were measured and fed into the thermal model as inputs.

Locked-rotor tests were conducted due to the ease of determining the natural convection cooling heat transfer coefficient on the end surfaces of the machine. Determining accurate heat transfer coefficients on the end-turn surface and rotor end surface due to rotor rotation at different speeds often requires detailed CFD simulation or complex experimental setups [5, 57–59], which is beyond the scope of this dissertation.

A synchronous reference frame current regulator is used to generate balanced three-phase currents with a switching frequency of 10kHz and a DC bus voltage of 290V. The magnitude of the current is determined by either a constant command in step response tests, or a dynamic command that corresponds to the torque of the driving cycle in driving cycle

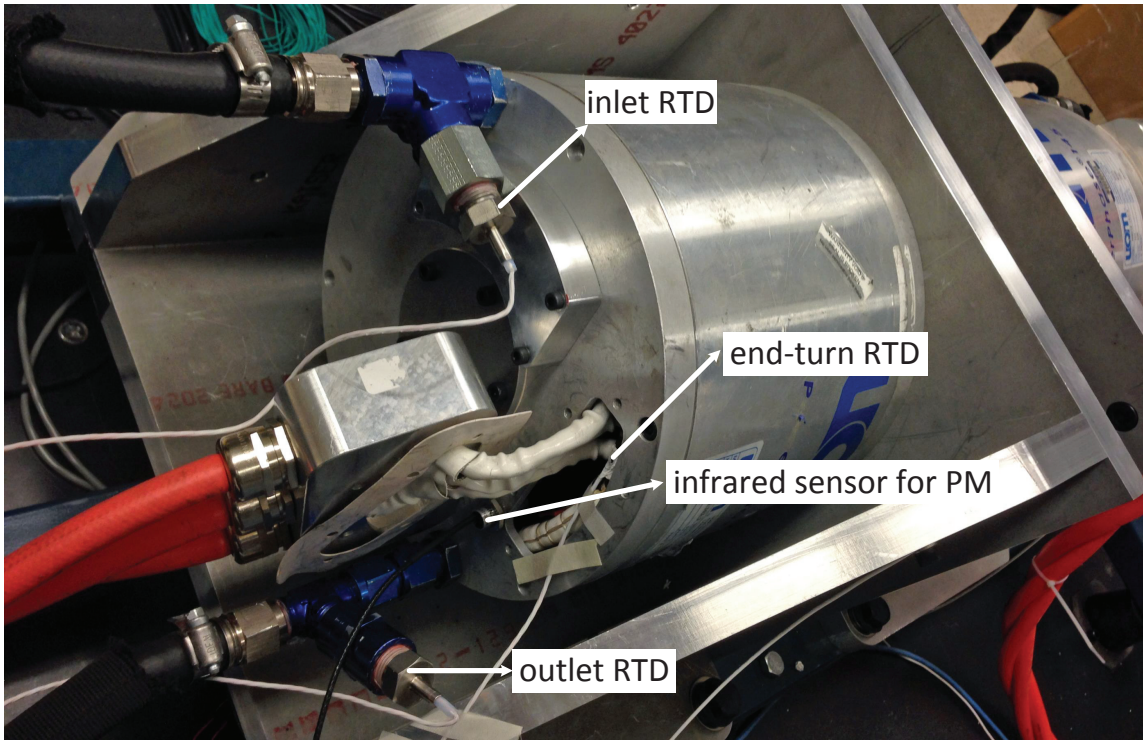

Figure 2.16: Temperature sensor locations.

tests. The electrical frequency of the stator current was kept at 40Hz in the locked-rotor tests. In these tests, the reduced-order model uses explicit Forward Euler integration for the purpose of mimicking real-time application, and reducing computation time.

The step response tests were conducted first to tune the thermal conductivity of the contact resistance layer between the PM and rotor iron. The thickness of the contact layer was set to 0.25mm. In the step response, the current magnitude is set at 200A. An optimization routine which minimizes the error between the measured and simulated PM temperature waveforms is used to find the optimal thermal conductivity. The step response with different thermal conductivities of the contact layer are shown in Fig. 2.17. As shown in the figure, $\kappa_{cont} = 3.1 \times 10^{-3}$W/(m·K) was found to be the optimal thermal conductivity, and was therefore used in all the simulations in this dissertation.

In the driving cycle test, the command shown in Fig. 2.12 was repeated twice to make the temperature rise more significant. The driving cycle response of the locked–rotor tests

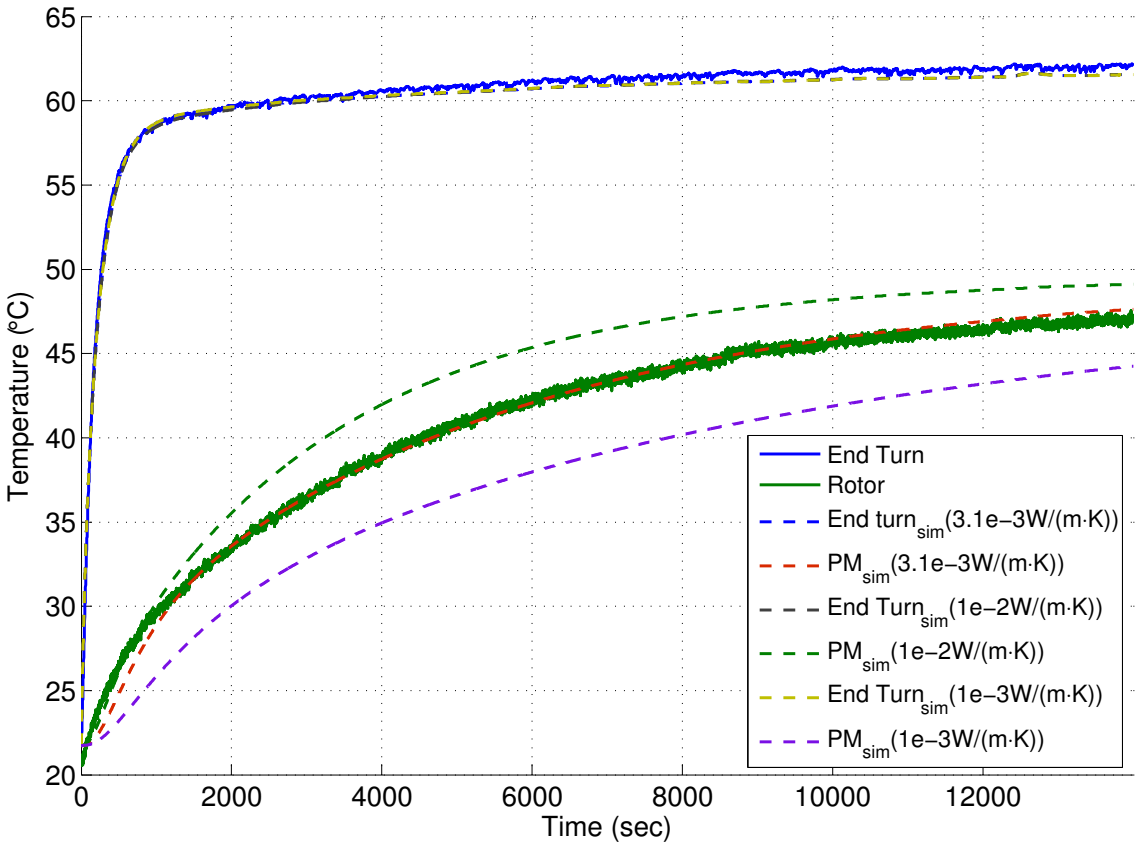

Figure 2.17: Experimental data vs. simulation, step response (I_{pk}=200A) with various thermal conductivities for the contact resistance layer. The experimental data was used in the tuning of the thermal conductivity of the contact layer, with 3.1e-3$W/(m \cdot K)$ found to be the optimal value.

is shown in Fig. 2.18. As can be seen from the figure, the simulation results (using a 7+4-order reduced-order model) match well with the experimental data. The absolute and RMS errors for the step and driving cycle response are listed in Table 2.4.

It takes the reduced-order model 33.0 milliseconds to simulate the driving cycle from 0 to 2600sec with a 1sec step length on Intel Xeon X2350 @ 2.67GHz dual-core CPU, which corresponds to a 12.7 microsecond computation time for each 1sec time step (an acceleration ratio of 78740). This is easily fast enough for a real-time temperature observer on the processor we used. It should also be fast enough for real-time micro-controller implementations of the model.

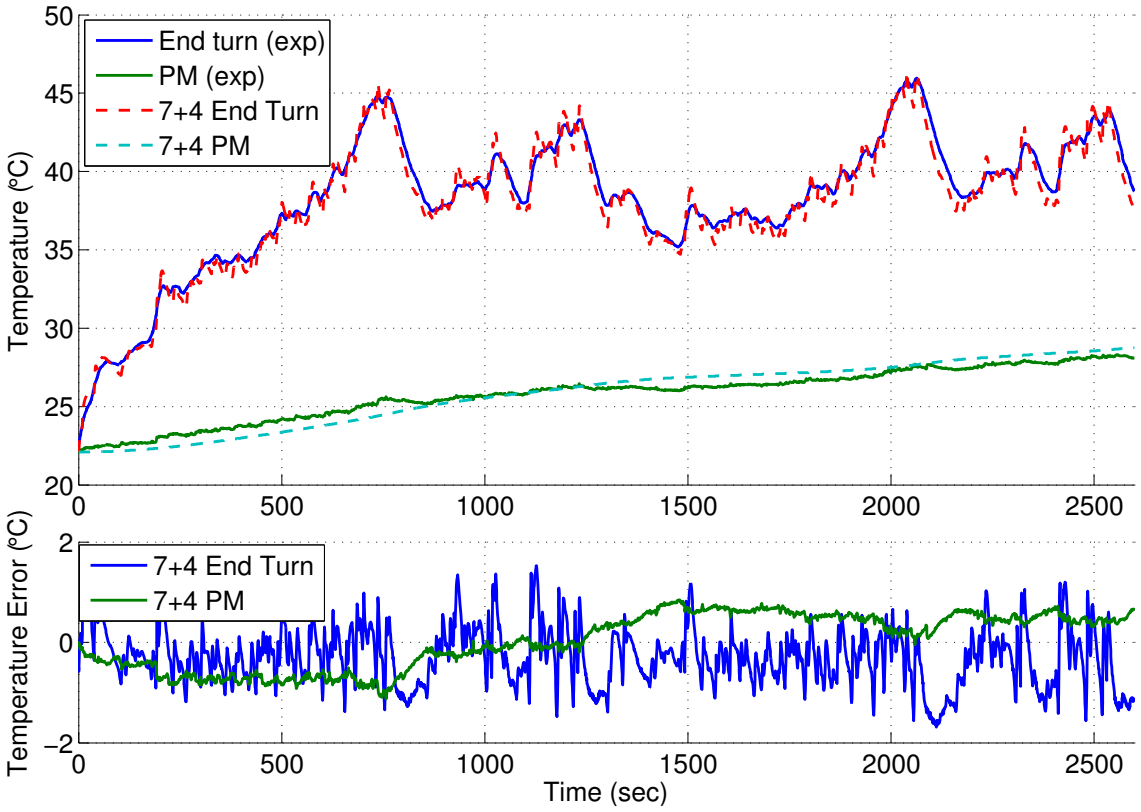

Figure 2.18: Comparison of experimental driving cycle test results with reduced order model consisting of 7 stator modes and 4 rotor modes.

Table 2.4: Error of the reduced-order model vs. experimental results

	# of States	Max. Error (°C) End Turn	Max. Error (°C) PM	Max. Relative Error End Turn	Max. Relative Error PM	RMS Error (°C) End Turn	RMS Error (°C) PM
Step Command	7+4	2.16	2.13	8.4%	8.2%	0.43	0.47
Driving Cycle	7+4	1.69	1.13	4.0%	4.4%	0.64	0.54

2.6 Discussion

2.6.1 Computation Time

There are four steps involved in the proposed model-order-reduction technique: 1) full-order model generation; 2) orthogonal eigenmode decomposition; 3) reduced-order model generation; 4) reduced-order model simulation. In the test case presented in this chapter, the first three steps take 36.5, 35.7 (when calculating the slowest 40 eigenvectors for stator and the slowest 30 for rotor), and 16.0 seconds, respectively, and the last step, as shown in Sections 2.4.3 and 2.5, only takes tens of milliseconds on the workstation described in Section 2.4.3.2. In electric/hybrid electric vehicle powertrain-level simulation or real-time temperature observer applications, the first three steps can be pre-calculated beforehand. Only the last step is required for each simulation or to be run in real-time conditions.

We also note that the total computation time for all the four steps (about 88.2sec) in the proposed technique is still almost 3 times faster than that required to simulate a full-order model (36.5sec for full-order generation, plus 219.8sec for simulation as shown in Table 2.3). Thus, the proposed reduced-order model can also bring significant benefits for applications that require the generation of new full-order models at each iteration (e.g. electric machine design optimization).

2.6.2 Explicit vs. Implicit Integration

In Section 2.4.3, implicit Trapezoidal integration was used to solve the full–order and reduced–order model for comparison purpose, while explicit Forward Euler integration was

used for the reduced-order model in Section 2.5 for the purpose of mimicking real-time application and reducing computation time.

Since the full–order model is a stiff system whose smallest time constant is on the order of microseconds, the explicit method is unstable unless using an extremely small time step, which results in long computation time. Thus, implicit integration methods have to be used in practice for the full-order model to ensure numerical stability and computational efficiency [56, pp. 72-73].

On the other hand, the smallest time constant of the reduced–order model is on the order of seconds, which makes explicit methods (such as Forward Euler) feasible. Since only scalar operations are involved in the reduced-order model, as shown in (2.26) where the matrices are diagonal, the reduced-order model avoids a matrix–vector solve at each step, thus being more computationally efficient. This shows another advantage of the reduced–order model over the full–order model.

Another benefit of using explicit numerical integration is that the temperature-dependent losses can be captured directly in the reduced-order model, where the losses are updated explicitly using the temperature at the previous time steps. For example, the winding conduction loss at temperature T can be evaluated as:

$$P_{wind,T} = P_{wind,20^\circ C}\left[1 + \beta\left(T - 20^\circ C\right)\right], \tag{2.33}$$

where $P_{wind,20^\circ C}$ is the winding conduction loss at 20°C, $\beta = 0.003862K^{-1}$ is the temperature coefficient of the electric resistivity of copper. Such temperature-dependent winding conduction loss was implemented in Section 2.5. Since the temperature-dependent P_k are serving as the inputs to the thermal model, the same model-order-reduction technique can be applied without any modification.

Unlike the thermal material properties, which are mild functions of temperature in the operating temperature range of electric machines (e.g. the thermal conductivity of copper

changes by about 3% over a temperature range of $-25°\mathrm{C}$ to $130°\mathrm{C}$, and its specific heat changes by less than 5% over the same range), the electromagnetic material properties are strong functions of temperature (e.g. the electric resistivity of copper). One nice feature of the proposed reduced-order thermal model is that it can provide temperatures for use in loss estimation.

2.6.3 Trade-offs in the Reduced-order Model

Although faster, the reduced-order model will always lose some information, and thus accuracy, when compared with the full-order model. Thus, there exists a trade-off between computation time and accuracy. A good model-order-reduction technique should allow the users to adjust such trade-off according to their specific applications. In the proposed model-order-reduction technique, users can adjust the accuracy by adjusting the following trade-offs.

2.6.3.1 Symmetry in the Thermal Model

In Section 2.4 and 2.5, only a tooth-slot pair was modeled for the stator, and only a single pole was modeled for the rotor, by assuming symmetries in the loss and boundary heat transfer distributions in the thermal model. This is only for the purpose of reducing the size of the 3D mesh and accelerating the generation process of the reduced order model. If an entire pole or an entire machine geometry is modeled, the 3D FE mesh becomes much larger, and the computation time and memory consumption for the reduced-model generation process (especially the eigenvector calculation) will increase substantially.

However, the proposed model-order-reduction technique will still work if an entire pole or an entire machine is modeled in the thermal model. Although the computation time for generating the reduced order model is much longer than that presented in this chapter, after the reduced-order model is generated, the model can be still fast to run since it contains a dramatically smaller number of dynamic states in the reduced model than that in the

full-order model. In some scenarios, it is necessary to model an entire pole or an entire machine, for example, when simulating stalling scenarios, unbalanced phase currents, or asymmetric cooling conditions. The proposed method would be actually more useful in these cases, as a traditional full-order 3D thermal model for an entire machine would be extremely computationally intensive.

2.6.3.2 Detailed Distributed Loss Modeling

In Section 2.3, the normalized loss density distribution vectors $\vec{f_k}$ are assumed to be independent of operating points in terms of current magnitude, phase angle, and rotor speed. This allows the pre-calculations of (2.24), (2.25), (2.26), and a straightforward extent of excitation calculation in (2.27). The proposed reduced-order model can also take the full-order nodal loss information as inputs, where (2.3) becomes

$$\vec{q} = \sum_k \vec{q}_k + \sum_l H_l \vec{g}_l, \tag{2.34}$$

where $\vec{q}_k$ is the nodal loss vector (internal forcing vector) calculated from the full-order FEA assembly process for each type of loss, which can be operating-point dependent and contains loss information for each node in the FE mesh. Equation (2.26) then becomes

$$\mathbf{d}_d \dot{\vec{x}}_d + \mathbf{k}_d \vec{x}_d = \mathbf{V_d^T} \vec{q}. \tag{2.35}$$

By using this technique, the distributed loss in the reduced-order model can be modeled as accurately as the full-order model. However, the computational benefits of pre-calculating time-invariant, operating-point-independent vectors $\vec{u}_k$, $\vec{s}_l$ and $\mathbf{V_d^T} \vec{f}_k$ in (2.24), (2.25), and (2.26) are lost. Instead, time-varying, operating-point-dependent full-order vectors $\vec{q}_k$ are needed. This increases the computation time and memory cost.

2.6.3.3 Time-dependent Convective Heat Transfer Boundary Condition

When the heat transfer coefficients on convective boundaries are time-invariant, by substituting (2.7) into (2.2), the nodal temperature component in (2.7) can be combined into the stiffness matrix $\mathbf{K}$ in (2.2) forming a combined stiffness matrix $\mathbf{K}'$. The orthogonal decomposition in Section 2.3.1 is then applied to $\mathbf{D}$ and $\mathbf{K}'$ for model-order-reduction. When the heat transfer coefficients on convective boundaries are time-varying (e.g. due to changes in cooling temperature or rotor speed), combining (2.7) and (2.2) would create a time-varying $\mathbf{K}'$. In this case, the orthogonal decomposition process is applied to $\mathbf{D}$ and the original stiffness matrix $\mathbf{K}$ for model-order-reduction, and the time- and temperature-dependent heat flux on the right hand side of (2.2) are considered as inputs to the system. Provided explicit numerical integration techniques are used, this is straight forward to implement.

2.6.3.4 Unit Delay from Air Gap Coupling for Solving Full-order Model

In this chapter, the stator and rotor models are simulated separately and coupled together using the air gap transfer relationship discussed in Section 2.2.3. For the implicit Trapezoidal integration used in Section 2.4.3, the boundary temperature at the previous time step (t_{k-1}) is used to calculate the air gap heat flux at t_k, which introduces a unit delay to the system dynamics. The unit delay can be eliminated by augmenting the stator and rotor state-space equations with the air gap transfer relationship to form a single state-space representation for the entire machine. The unit delay has negligible impact on the simulation results in this chapter and eliminating it by augmenting the matrices makes the simulation time much longer. Thus, the unit delay is kept in this chapter.

For example, simulating a single 103.9k-state model for the entire machine is more than 20 times slower than simulating a 52.2k-state stator model and a 51.7k-state rotor model coupled by air gap, while the accuracy improvement from unit-delay elimination is in the range of $0.01^{\circ}\mathrm{C}$.

2.7 Conclusion

A CE 3D FE-based dynamic thermal model is proposed, developed, and presented in this chapter. By applying orthogonal decomposition and eigenmode-based MOR, the full-order 3D FEA model can be reduced to a ROM with a small number of states based on the proposed "normalized extent of excitation" calculation. Results show that the proposed model can dramatically reduce the computation time by over 4 orders of magnitude comparing with a full-order dynamic thermal FEA model while maintaining satisfactory accuracy. Experimental results show that a ROM with 7 stator states and 4 rotor states can accurately capture the temperature response in the testing machine comparing with measurements. These results suggest that, although the geometry of an electric machine can be complex and may result in a large 3D FEA mesh, a dynamic thermal model with a few dynamics states can be accurate enough for many applications. This chapter presents a systematic way of generating such a reduced-order model. Furthermore, a ratio of 80000 between simulation time and real time was observed in Section 2.5, which is fast enough for real-time implementation in embedded controllers.

Such a CE thermal model can be useful in real-time condition monitoring, model-based controls, system-level simulation, and thermal protection/management. Moreover, the MOR process only requires calculating a small subset of eigenvectors of the full-order 3D FEA model, and does not depend on the inputs to the system. Thus, the ROM generation process is also fast. As a result, the computation time for generating and simulating the ROM is still 3 times faster than simulating the full-order model. This can bring benefits for applications that require the generation of new full-order models at each iteration (e.g. electric machine design optimization).

CHAPTER 3

Computationally–Efficient Magnetostatic-FEA-based Scalable Model of Electric Machines

3.1 Introduction

This chapter focuses on developing a physics-based, CE, scalable EM electric machine model for vehicle powertrain designers that is fast enough for powertrain-level simulation/optimization. The proposed scaling framework is based on MS FEA, which makes it possible to quickly generate and determine the EM performance of new machine designs through the application of scaling techniques to an existing "base" design. Three scaling techniques are used to quickly generate new machine designs from the base design for vehicle powertrain-level simulation and optimization. Using the proposed scaling techniques, the performance of the new designs in terms of efficiency map can be predicted quickly by avoiding re-solving FEA for the scaled designs, so vehicle powertrain designers can efficiently adjust the characteristics and the performance of the machine in ways that are favorable to the overall vehicle performance. The result is a scalable model that can estimate the efficiency map of a new scaled machine design in several core-minutes, after a base-design database is pre-calculated. This is fast enough to be integrated into vehicle powertrain optimization.

In Section 3.2, the MS finite element model used in this dissertation is discussed. This is used in the FEA database generation process. Section 3.3 presents three scaling techniques for generating new designs from a "base design" FEA database. It is shown that the performance of the scaled designs can be estimated directly from the base design database, without the necessity of re-solving FEA. In Section 3.4, the process of the proposed design scaling simulation framework is presented. In Section 3.5, results and examples are presented to demonstrate the benefits the proposed method can bring to the powertrain designers. In this chapter, a permanent magnet synchronous machine (PMSM) design is used as a case study to illustrate the proposed technique. But the proposed scaling techniques are general and can work with other types of machine topologies, such as field-wound synchronous machines, induction machines, and switched reluctance machines.

3.2 Finite Element Modeling and Post-Processing

Nonlinear 2D MS FEA and post-processing techniques are used in this dissertation to estimate the EM performance of a machine instead of transient or steady-state analysis. This choice is due to the following reasons. First, MS FEA is much faster to solve than transient or steady-state analysis. Second, MS FEA is rotor-position-dependent instead of time-dependent so it can be used for all rotor speeds. Third, MS FEA enables the proposed number-of-turns scaling technique, which will be discussed in Section 3.3. It is noted that the accuracy of loss estimation will suffer to some extent using MS FEA. However, this is a trade-off for making the model feasible to be used in powertrain level simulation/optimization.

The MS formulations used in this dissertation are listed below:

$$\nabla \cdot \vec{B} = 0, \tag{3.1}$$

$$\nabla \times \vec{E} = 0, \tag{3.2}$$

$$\nabla \times \vec{H} = \vec{J}, \tag{3.3}$$

where $\vec{B}$ is magnetic flux density, $\vec{E}$ is electric field intensity, $\vec{H}$ is magnetic field intensity, and $\vec{J}$ is electric current density. Note that the dynamic effects in Faraday's Law are neglected in MS FEA, as shown in (3.2). In this dissertation, a current-driven MS FEA model is used. Thus, the inputs to the model are current magnitude and phase angle, and rotor position.

3.2.1 Torque Calculation

The instantaneous electromagnetic torque is calculated using FEA for a given combination of current magnitude, phase angle, and rotor position. Several rotor positions within one period are then simulated, and the average torque is calculated and stored in the database for later use.

3.2.2 Loss Calculation

Winding conduction losses, stator and rotor core losses, PM eddy current losses, and power electronic losses are estimated using MS FEA, post-processing techniques, and analytical relationships.

3.2.2.1 Winding Conduction Losses

The winding conduction losses are estimated as follows:

$$P_{cond} = N_{slot} \left(l_{slot} + l_{end} \right) \sigma_{slot} \iint J^2 ds, \tag{3.4}$$

where N_{slot} is the number of slots, l_{slot} is the length of the slot, l_{end} is the length of the end winding, σ_{slot} is the effective electrical conductivity of the slot region, and J is the current density. The length of the end winding can be determined through measurement of the base design, or estimated using analytical relationships based on the dimensions and the layout of the winding (e.g., [60, 61]).

The effective electrical conductivity of the slot region σ_{slot} can be calculated as:

$$\sigma_{slot} = \sigma_{copper} f_{fill}, \tag{3.5}$$

where σ_{copper} is the conductivity of copper, and f_{fill} is the slot fill factor.

The electric resistivity of copper is a function of temperature, and can increase by 54.07% with a temperature rise from $20°\mathrm{C}$ to $160°\mathrm{C}$. An accurate estimation of the temperature effect on winding resistance is not possible without coupling a thermal model to the EM model. In this chapter, the resistivity of copper is adjusted to the winding temperature limit for continuous operation as a rough approximation to such temperature effect:

$$\rho_{Cu,T_1} = \rho_{Cu,T_0} \left[1 + \beta \left(T_1 - T_0\right)\right] \tag{3.6}$$

where T_1 is the winding temperature limit for continuous operation, $T_0 = 20°C$ is room temperature, ρ_{Cu,T_1} is the resistivity of copper at T_1, $\rho_{Cu,T_0} = 1.68 \times 10^8 \Omega \cdot m$ is the resistivity of copper at room temperature, $\beta = 0.003862 K^{-1}$ is the temperature coefficient of the electric resistivity of copper.

3.2.2.2 Core Losses

Core losses are estimated in post-processing using the flux density distribution in the lamination calculated from 2D MS FEA. The flux density vector in each finite element $\vec{B}(\theta_r)$ is evaluated at a set of different rotor positions θ_r within one period. The rotor–position–dependent flux density $\vec{B}(\theta_r)$ is then converted to time-dependent flux density

$\vec{B}(t)$ at specific rotor speeds (and electrical frequencies f_e), where t and θ_r are related as

$$t = \frac{\frac{N_{pole}}{2}\theta_r}{2\pi f_e}, \tag{3.7}$$

where N_{pole} is the number of poles.

There are two important phenomena to capture in the core loss calculation of electric machines: 1) non-sinusoidal flux density waveforms; 2) the rotational field. Building an accurate model to capture both effects is difficult, and "no relevant significant work has appeared in the literature" [62]. In this chapter, the rotational core losses due to the rotational flux density vector with harmonics are calculated as the sum of pulsating losses with harmonics in both x and y directions [62]:

$$P_{core} = P_{core,x}\left(B_x\left(t\right)\right) + P_{core,y}\left(B_y\left(t\right)\right), \tag{3.8}$$

where P_{core} is the rotational core loss, $P_{core,x}$ and $P_{core,y}$ are the pulsating core loss with harmonics in x and y directions, which are functions of flux density B_x and B_y, respectively.

Among several core loss models, two models were found to be suitable for capturing the harmonics in the pulsating core loss in this paper: 1) a Fourier-series-based method [63] which is fast but lacks accuracy as it assumes the losses of each harmonic are independent of one another; and 2) an Improved Generalized Steinmetz Equation (IGSE) [64] which can capture the nonlinearity and minor loops, but is computationally intensive to run. As the proposed scaling techniques in Section 3.3 do not depend on the choice of loss model, users can decide on which loss model to use. The first method is presented below, and used in the simulation in this dissertation due to its computational efficiency.

By performing Fourier Transform on the x component of $\vec{B}(t)$, the core losses can then

be evaluated as a function of f_e and $\hat{B}_{x,h}$ as:

$$P_{core,x} = \sum_h P_h \left(f_e, \hat{B}_{x,h} \right). \tag{3.9}$$

where $P_{x,h}$ is the pulsating core loss at the h-th harmonic in x direction, $\hat{B}_{x,h}$ is the flux density at the h-th harmonic in x direction. Using the Steinmetz Equation, the core loss can be normalized with respect to frequency as follows:

$$\begin{aligned} P_{core,x} &= c_e N_{pole} l \sum_h c_1 (h f_e)^{c_2} \sum_i \iint_{\Delta_i} \hat{B}_{x,h}^{c_3} ds \\ &= {f_e}^{c_2} P_{core,x,norm}, \end{aligned} \tag{3.10}$$

where

$$P_{core,x,norm} = c_e N_{pole} l \sum_h c_1 h^{c_2} \sum_i \iint_{\Delta_i} \hat{B}_{x,h}^{c_3} ds \tag{3.11}$$

is the normalized core loss in x direction, l is the length of the iron, Δ_i is the area of the i-th finite element, and c_1, c_2, c_3 are the Steinmetz coefficients. An empirical corrective coefficient c_e is used to take the manufacturing and lamination process into account, as the core loss estimation is usually systematically lower than the measurement to the extent that a factor of 2 or more are often observed [65]. The same process applies for the y direction.

3.2.2.3 Permanent Magnet Eddy Current Losses

The permanent magnet eddy current losses can be estimated using Faraday's Law [66, 67]:

$$\vec{E} = -\left(\frac{\partial \vec{A}}{\partial t} + \nabla \phi \right), \tag{3.12}$$

where $\vec{E}$ is the electric field intensity, $\vec{A}$ is the magnetic vector potential, and ϕ is the electric potential. No net current in the permanent magnets indicates

$$\iint_{S_i} \left(\frac{\partial \vec{A}}{\partial t} + \nabla \phi \right) ds = 0, \tag{3.13}$$

where S_i is the area of the i-th PM. The electric potential of the i-th PM in the average sense can therefore be obtained as

$$\nabla \phi = -\frac{1}{S_i} \iint_{S_i} \frac{\partial \vec{A}}{\partial t} ds. \tag{3.14}$$

In a 2D problem, $\vec{A} = A_z \hat{z}$, thus

$$E_z = -\left(\frac{\partial A_z}{\partial t} - \frac{1}{S_i} \iint_{S_i} \frac{\partial A_z}{\partial t} ds \right). \tag{3.15}$$

In the harmonic form, the h-th harmonic of the electric field is

$$E_{zh} = -j\omega_e h \left(A_{zh} - \frac{1}{S_i} \iint_{S_i} A_{zh} ds \right), \tag{3.16}$$

where $\omega_e = 2\pi f_e$ is the electrical angular velocity. For linear triangular finite elements, define the magnetic vector potential of the i-th PM in the average sense as

$$\begin{aligned} A_{avg,h} &= \frac{1}{S_i} \sum_{k=1}^{N_i} \iint_{\Delta_k} A_{zhk} ds \\ &= \frac{1}{S_i} \sum_{k=1}^{N_i} \frac{\Delta_k}{3} \left(A_{zhk,1} + A_{zhk,2} + A_{zhk,3} \right), \end{aligned} \tag{3.17}$$

where N_i is the number of elements in the i-th PM, Δ_k is the area of the k-th element, and $A_{zhk,1}, A_{zhk,2}, A_{zhk,3}$ are the nodal values of the k-th element. Thus, the nodal value of the

eddy current density is given by

$$J_{EC,h} = -j\omega_e h\sigma_{PM}(A_{zh} - A_{avg,h}) = f_e J_{EC,norm}, \tag{3.18}$$

where σ_{PM} is the electric conductivity of the PM material and $J_{EC,norm} = -2\pi j h\sigma_{PM}(A_{zh} - A_{avg,h})$ is the normalized eddy current density with respect to frequency at each node.

If J corresponds to the peak value, the average eddy current loss in a linear triangular element is [68]

$$\begin{aligned} P_k &= \Re e\left(\frac{l_{PM}}{2\sigma_{PM}}\iint_{\Delta_k} J_{EC}{J_{EC}}^* ds\right) &(3.19)\\ &= \frac{\Delta_k l_{PM}}{12\sigma_{PM}}[|J_{k1}|^2 + |J_{k2}|^2 + |J_{k3}|^2 + \Re e(J_{k1}J_{k2}^* + J_{k1}J_{k3}^* + J_{k3}J_{k2}^*)]. &(3.20)\end{aligned}$$

where l_{PM} is the length of PM, and J_{k1}, J_{k2}, J_{k3} are the nodal eddy-current densities of the k-th element. The total eddy current loss in PM is then given by

$$P_{PM} = N_{pole}\sum_{k=1}^{N_i} P_k = f_e^2 P_{PM,norm}, \tag{3.21}$$

where $P_{PM,norm}$ is the normalized eddy current loss with respect to frequency, which is calculated using the normalized eddy current density $J_{EC,norm}$. It is noted that the proposed scaling techniques in Section 3.3 do not depend on the choice of PM eddy-current loss estimation method. Users can also choose to use other post-processing techniques, e.g. [30].

The conduction loss calculation in (3.4) is independent of frequency, and therefore underestimates the winding losses at high rotor speeds by not capturing the skin and proximity effect. Furthermore, PM losses are overestimated by neglecting the effects of the induced currents on the magnetic field structure. These are the compromises created due to our use of MS FEA.

One advantage of using the MS approach and the proposed loss expressions is that the

core losses in (3.10) and PM losses in (3.21) can be normalized with respect to frequency, thanks to the proportional relationship with respect to f_e^x. Using normalized expressions for these losses, all of the calculated values for a given operating point of current magnitude and phase angle are independent of frequency, and the results can be easily used for any frequency (i.e., rotor speed). Another benefit of using normalized losses is that the flux density distribution in the iron and the eddy-current density distribution in the PM are no longer needed to be stored in the database, which dramatically reduces the file size of the FEA database.

3.2.2.4 Power Electronic Losses

Power electronic losses, which include the conduction losses of the insulated-gate bipolar transistors (IGBT) and the anti-parallel diodes, switching losses, reverse recovery losses, and gate charging losses, can be calculated using analytical relationships and empirical data. In this dissertation, the power electronic losses are calculated as follows.

IGBT conduction losses can be calculated as [69–71]:

$$P_{IGBT,cond} = \left(\frac{1}{2} - \frac{T_d}{T_s}\right)\left(V_{CE0}\frac{I_{pk}}{\pi} + R_c\frac{I_{pk}^2}{4}\right) + \left(V_{CE0}\frac{I_{pk}}{8} + R_c\frac{I_{pk}^2}{3\pi}\right), \tag{3.22}$$

where T_d is the dead-time duration, $T_s = \frac{1}{f_{sw}}$ is the switching period, f_{sw} is the switching frequency, V_{CE0} is the IGBT on-state zero-current collector-emitter voltage, R_c is the collector-emitter on-state resistance, and I_{pk} is peak phase current.

Diode conduction losses can be calculated as [69–71]:

$$P_{diode,cond} = \left(\frac{1}{2} + \frac{T_d}{T_s}\right)\left(V_{d0}\frac{I_{pk}}{\pi} + R_d\frac{I_{pk}^2}{4}\right) - \left(V_{d0}\frac{I_{pk}}{8} + R_d\frac{I_{pk}^2}{3\pi}\right) \tag{3.23}$$

where V_{d0} is the diode forward voltage drop at zero current, and R_d is the diode on-state resistance.

Assuming voltage and current changes linearly during switching, the IGBT turn-on and

turn-off losses can be approximated as:

$$P_{IGBT,on} = \int_{t_1}^{t_2} V_{CE} I_C dt = f_{sw} \frac{V_{pk} I_{pk}}{\pi} \left(\frac{t_{rise}}{4} + \frac{t_{d,on}}{2} \right), \tag{3.24}$$

$$P_{IGBT,off} = \int_{t_3}^{t_4} V_{CE} I_C dt = f_{sw} \frac{V_{pk} I_{pk}}{\pi} \left(\frac{t_{d,off}}{2} + \frac{0.95 t_{fall}}{3} \right), \tag{3.25}$$

where V_{pk} is peak phase voltage, t_{rise} is the rise time, t_{fall} is the fall time, $t_{d,on}$ is the turn-on delay time, and $t_{d,off}$ is the turn-off delay time. A more accurate approximation can be found in [72].

Diode turn-on losses can be calculated as [69]:

$$P_{diode,turn-on} = \frac{1}{4} Q_{rr} V_{Drr} f_{sw}, \tag{3.26}$$

where Q_{rr} is the diode reverse recovery charge, and V_{Drr} is the voltage across the diode during reverse recovery.

Gate charging losses can be calculated as [69]:

$$P_{gate} = Q_g V_{GE} f_{sw}, \tag{3.27}$$

where Q_g is the total gate charge, and V_{GE} is the IGBT gate-emitter voltage.

3.2.3 Flux Linkage

In 2D FEA, the calculated flux linkage does not capture the end-winding leakage inductance. This inductance can be estimated using analytical relationships, e.g., [60, 61]. In this chapter, the following relationship is used [60]:

$$L_{end} = \mu_0 R_e N_c^2 \left[\ln \frac{8R_e}{R} - 2 \right], \tag{3.28}$$

where L_{end} is the end-winding leakage inductance, μ_0 is the vacuum permeability, R_e is half of the winding arc length, N_c is the number of turns per coil, and R is the geometric mean distance of the coilside from itself.

Thus, the fundamental flux linkage with end-winding effect included can be compensated as

$$\tilde{\lambda}_1 = \tilde{\lambda'}_1 + L_{end}\tilde{I} \tag{3.29}$$

where $\tilde{(\cdot)}$ denotes a phasor quantity, $\tilde{\lambda'}_1$ is the fundamental flux linkage from the 2D FEA simulation, and $\tilde{I}$ is the phase current.

3.2.4 Demagnetization Check

To predict demagnetization in the electric machine, the maximum magnetic field intensity in the PM region needs to be calculated and compared with the intrinsic coercivity of the PM material times a safety factor. Thus, the maximum magnetic field intensity of the PM region for each operating point is also stored in the base design database for later use.

3.3 Design Scaling for Electric Machines

For the purpose of building FEA databases and generating efficiency maps, the torque, normalized losses, flux linkage, and magnetic field intensity of the base design are calculated over a wide range of operating points and stored in a "base design" database for use in the proposed scaling techniques. The base design is scaled using three independent techniques, which create the ability for powertrain designers to quickly adjust the torque-speed curve and efficiency maps in ways that are favorable to the vehicle powertrain. Each scaling technique is discussed in this section, while the entire scaling framework with detailed procedures is presented in Section 3.4.

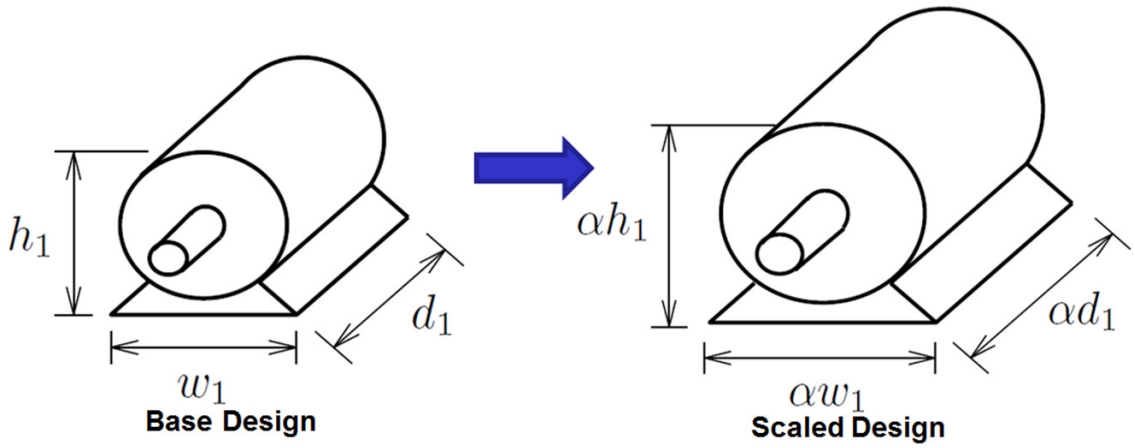

Figure 3.1: Dimensional scaling

3.3.1 Dimensional Scaling

The first scaling method, as illustrated in Fig. 3.1, is to proportionally scale all the dimensions of the base design by a factor of α as $\vec{r}_\alpha = \alpha\vec{r}_1$, where $\vec{r}$ denotes the coordinate system, subscript "1" is for the base design, and "α" is for the scaled design. In the scaled design, magnetic fields, flux densities, and electric potentials (voltages) are forced to remain consistent with the base design, as they are the fundamental limiting factors of the machine's performance capability.

$$\text{Flux density: } \vec{B}_\alpha\left(\vec{r}_\alpha, t_\alpha\right) = \vec{B}_1\left(\vec{r}_1, t_1\right), \tag{3.30}$$

$$\text{Field intensity: } \vec{H}_\alpha\left(\vec{r}_\alpha, t_\alpha\right) = \vec{H}_1\left(\vec{r}_1, t_1\right). \tag{3.31}$$

$$\text{Electric potential: } \phi_\alpha\left(\vec{r}_\alpha, t_\alpha\right) = \phi_1\left(\vec{r}_1, t_1\right). \tag{3.32}$$

The voltage will be adjusted by the second scaling method, as will be discussed later in Section 3.3.2. Under the above three constraints, it can be shown that the quantities in the scaled design and the base design are related as follows [44].

3.3.1.1 Time

To achieve the desired relationships in (3.30, 3.31), the time t, and rotor speed ω_r, must be scaled as follows:

$$t_\alpha = \alpha^2 t_1, \tag{3.33}$$

$$\omega_{r,\alpha} = \frac{1}{\alpha^2}\omega_{r,1}. \tag{3.34}$$

3.3.1.2 Electromagnetic Field Scaling

The electromagnetic field quantities of the base and scaled designs can be related as follows:

$$\text{Flux linkage:} \quad \lambda_\alpha(t_\alpha) = \alpha^2 \lambda_1(t_1), \tag{3.35}$$

$$\text{Current density:} \quad J_\alpha(\vec{r}_\alpha, t_\alpha) = \frac{1}{\alpha} J_1(\vec{r}_1, t_1), \tag{3.36}$$

$$\text{Current:} \quad I_\alpha(\vec{r}_\alpha, t_\alpha) = \alpha I_1(\vec{r}_1, t_1). \tag{3.37}$$

3.3.1.3 Electromagnetic Performance Scaling

The torque, total loss, and thus efficiency of the base and scaled designs are related as follows:

$$\text{Torque:} \quad \tau_{em,\alpha} = \alpha^3 \tau_{em,1}, \tag{3.38}$$

$$\text{Losses:} \quad P_{loss,\alpha} = \alpha P_{loss,1}, \tag{3.39}$$

$$\text{Efficiency:} \quad \eta_\alpha(\tau_{em,\alpha}, \omega_{r,\alpha}) = \eta_1(\tau_{em,1}, \omega_{r,1}). \tag{3.40}$$

Using (3.34, 3.38, 3.39), the efficiency maps of the scaled designs can be generated directly using the information in the base design database. Note that, according to (3.40), there is a direct mapping between the base design efficiency map and the scaled design efficiency map in dimensional scaling. The point $(\tau_{em,1}, \omega_{r,1}, \eta_1)$ on the base design efficiency map

directly corresponds to the point $(\tau_{em,\alpha}, \omega_{r,\alpha}, \eta_\alpha)$ on the scaled design efficiency map.

3.3.2 Number-of-Turns Scaling

The second scaling method is to scale the number of turns in the winding. The effective number of turns of a phase can be represented using a factor of N, as illustrated in Fig. 3.2.

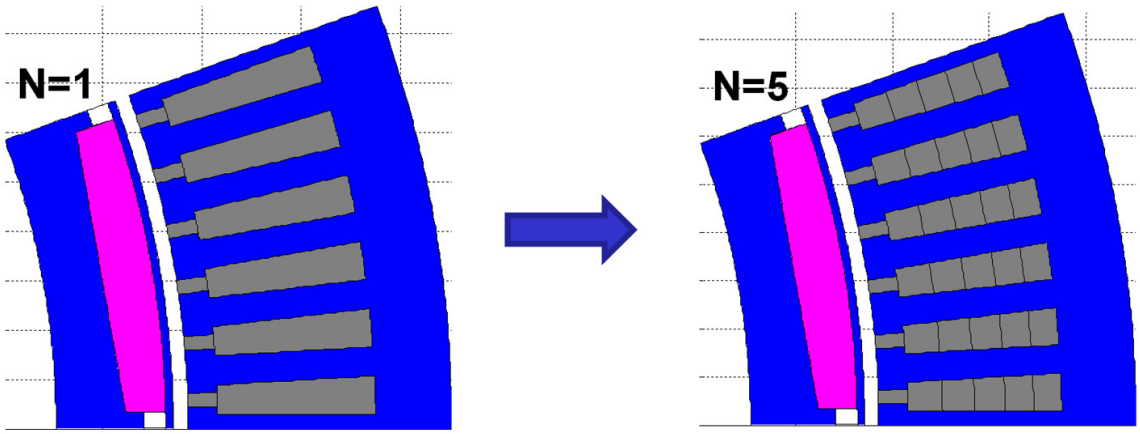

Figure 3.2: Number-of-turns scaling

The concept of effective number of turns N is used to represent the total flux linkage linking one phase, which affects the terminal voltage–current relationship. The terminal voltage–current relationship can be affected by several factors, e.g. the number of turns per coil, the winding connection scheme (parallel or series connection of the pole–pairs), and Δ/Y connection. Thus, the effective number of turns N is not limited to integer numbers. For example, for a base design with 18 poles (9 pole pairs) connected in series, 1 turn per coil, and a Y-winding configuration, the effective number of turns N can be scaled by the multiplication of the following three factors: 1) any natural numbers of turns per coil (1, 2, 3, ...); 2) pole-pair connection factors (1 for 9 pole pairs connected in series, $\frac{1}{3}$ for 3 in series, then in parallel, and $\frac{1}{9}$ for 9 in parallel); and 3) Y/Δ factor (1 for Wye, $\frac{1}{\sqrt{3}}$ for Δ).

The base design is considered to have 1 turn per coil (i.e. $N = 1$) in the number-of-turns scaling. After the turn scaling is applied, the total current in a slot of the scaled design is determined by the effective number of turns, combination of winding scheme (e.g., parallel

or series connection of poles, and Δ/Y connection) and the current information in the base design database. The operating points of the scaled design and the base design are related by the current density in a slot. The operating points which have the same current density distribution in the base design FEA database are used to calculate the performance of the scaled design. Since the scaled and the base design have the same current density distribution, the area of a single turn and the terminal current of the machine has the following scaling relationship:

$$A_N = \frac{A_1}{N}, \tag{3.41}$$

$$I_N = \frac{I_1}{N}, \tag{3.42}$$

where the subscript "1" is for the base design, and "N" is for the scaled design. Furthermore, the total length of all the turns, and thus the phase resistance, has the following scaling relationship:

$$l_N = Nl_1 \tag{3.43}$$

$$R_N = \rho_{slot}\frac{l_N}{A_N} = \rho_{slot}\frac{Nl_1}{\frac{A_1}{N}} = N^2 R_1, \tag{3.44}$$

where ρ is the resistivity of the winding material.

Since the "base" design database consists of position-dependent MS analysis, the time and rotor speed can be scaled easily to calculate the fundamental component of the phase voltage of the scaled design by using the scaling relationship (3.42,3.44) and $\lambda_N = N\lambda_1$:

$$\tilde{V}_N = \tilde{I}_N R_N + j\omega_e \tilde{\lambda}_N \tag{3.45}$$

$$= N\left(\tilde{I}_1 R_1 + j\omega_e \tilde{\lambda}_1\right). \tag{3.46}$$

The voltage constraint, which is imposed by the power electronics, can thus be checked for the scaled design.

3.3.3 Slot/Pole Scaling

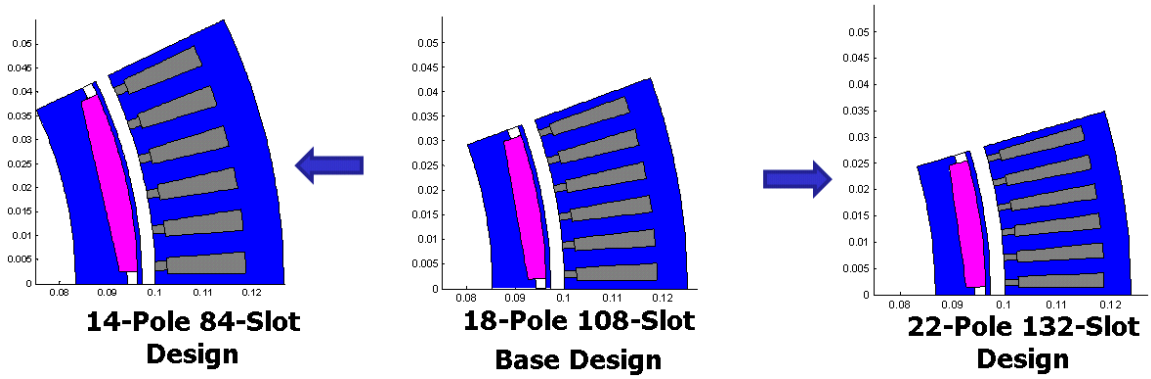

Figure 3.3: Slot/Pole scaling

The third scaling method, as illustrated in Fig. 3.3, is to proportionally scale the number of slots and the number of poles, while making the slot/pole ratio constant. To improve the performance of the scaled design, the thickness of the stator and rotor back-iron are adjusted by [60]

$$t_{N_{pole}} = t_{base}\frac{N_{base}}{N_{pole}}, \tag{3.47}$$

where N_{base} and N_{pole} are the number of poles in the base design and the scaled design, respectively, $t_{N_{base}}$ and t_{pole} are the back-iron thickness in the base design and the scaled design, respectively. By using a thinner back-iron when increasing the number of poles, the weight can be reduced. Since there is no straightforward way to relate the performance of the base design and the scaled design in slot/pole scaling, separate FEA databases need to be built for this scaling technique. The dimensional and number-of-turns scaling are then applied to each database.

As a summary, using the above three independent scaling techniques, new machine designs can be generated easily. In the first two scaling techniques, the performance of the scaled design can be calculated directly by using the pre-generated FEA database, without the necessity of re-solving the computationally intensive FEA for each scaled design. It is

noted that the proposed scaling techniques are general and can work with both 2D and 3D MS FEA database. 2D FEA is discussed in this dissertation only for illustration purposes.

3.4 Simulation

The process of the proposed simulation framework is presented in this section. There are three steps involved in the proposed techniques: 1) the pre-calculation of base design FEA databases, 2) the generation of scaled designs, and 3) efficiency map generation for the scaled designs.

3.4.1 Pre-calculation of Base Design FEA Database

In the database generation process, MS FEA is solved and post-processing techniques are used for a wide range of current magnitudes I and phase angles θ_I, as introduced in Section 3.2. The average torque over one period, normalized losses, flux linkage, and the maximum magnetic field intensity in the PM are calculated and stored in a database as two-dimensional lookup tables, with current magnitude and phase angle as inputs.

3.4.2 Scaled Design Generation

Scaled designs can be generated using the three scaling techniques proposed in Section 3.3. After a set of scaling parameters (α and N) is chosen, the pre-calculated databases are scaled correspondingly, according to the scaling relationships presented in Section 3.3.1 and 3.3.2. Post-processing is then used to estimate the losses at all rotor speeds (ω_r) by using the relationships presented in Section 3.2.2. The result is a set of data which contains torque (τ), losses (P_{loss}), voltage (V), and the maximum magnetic field intensity of the PM region (H_{max}) for all the (I,θ_I,ω_r) combinations. It is then used for calculating the efficiency map of the scaled design.

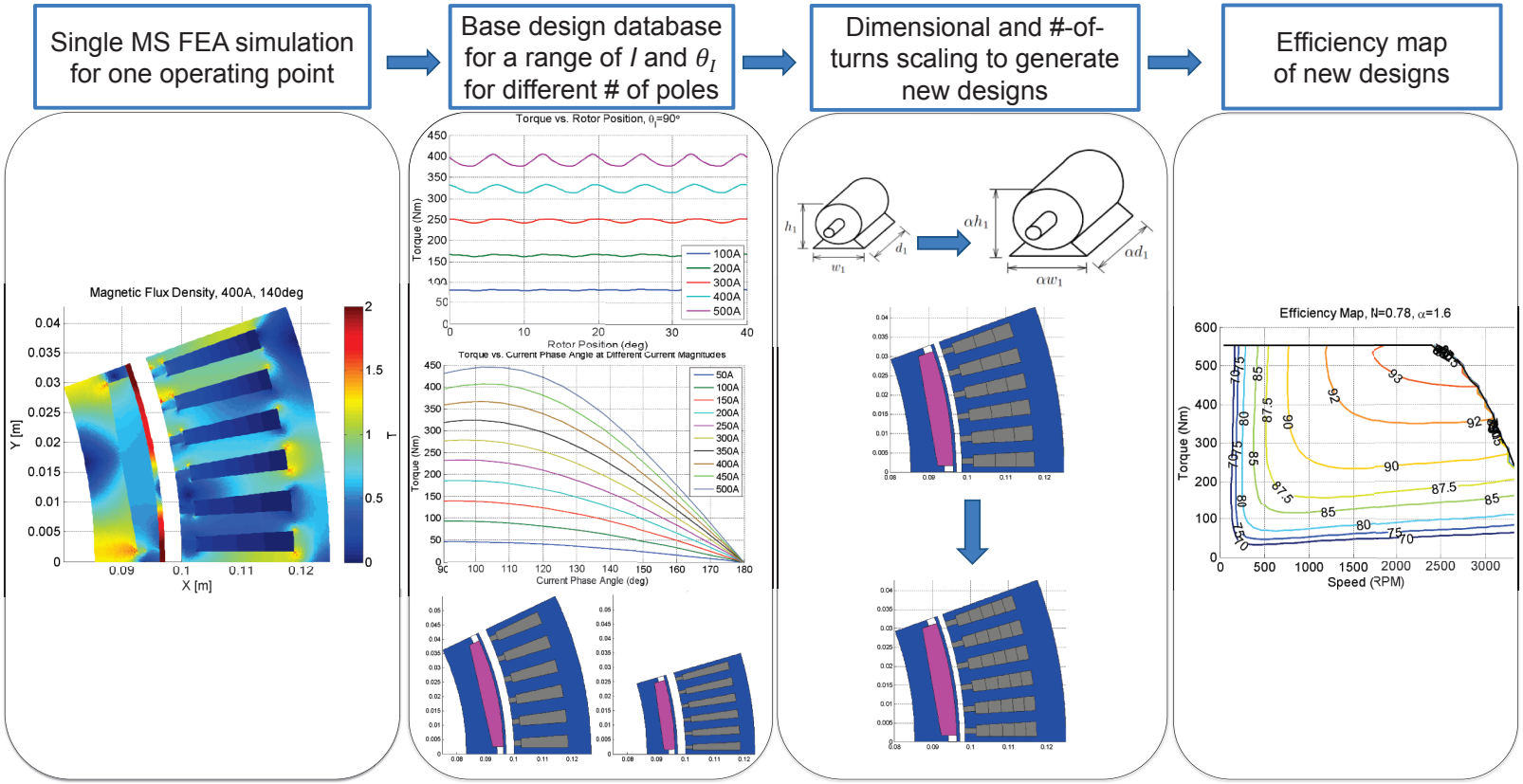

Figure 3.4: Flowchart of the overall scaling process

Algorithm 3.1: Optimal operating point search

Input: a point (τ, ω_r) on efficiency map
Data: τ, P_{loss}, V, H_{max}, V_{lim} and I_{lim}
Result: $(I_{opt}, \theta_{I,opt})$ and its efficiency η_{opt}

$\eta_{test} \leftarrow 0$;
Determine I_{min}, the smallest I that can produce τ (i.e. the min. current operating point);
for I=I_{min} **to** I_{lim} **do**
    Search for θ_I that can produce τ at I using interpolation;
    if *found* **then** `// τ is achievable at I`
        if $V \leq V_{lim}$ *and* $H_{max} < cH_{ci}$ **then**
            `// by interplolation`
            Calculate losses and efficiency at (I, θ_I);
            if $\eta(I, \theta_I) > \eta_{test}$ **then**
                $\eta_{test} \leftarrow \eta(I, \theta_I)$;
                $(I_{opt}, \theta_{I,opt}) \leftarrow (I, \theta_I)$;
            end
        end
    end
end
$\eta_{opt} \leftarrow \eta_{test}$;

3.4.3 Efficiency Map Generation

The optimal-efficiency operating points $(I_{opt}, \theta_{I,opt})$ need to be found for efficiency map calculation. The optimal-efficiency operating points are defined as the (I,θ_I) combination that minimizes losses for a given (τ,ω_r) while satisfying voltage and current constraints (V_{lim} and I_{lim} imposed by power electronics) without demagnetizing the permanent magnets (i.e. $H_{max} < cH_{ci}$, where H_{ci} is the intrinsic coercivity, and $c < 1$ is a safety factor). Algorithm 1 is used to find the optimal operating points. For a given torque and speed (i.e. a point on efficiency map), the smallest current magnitude that can produce the torque is determined first (i.e. the minimum current operating point). The current magnitude is then swept from this minimum value to the current limit in the algorithm. At each current magnitude, the phase angle that can produce the torque is determined through interpolation. The efficiency at such current magnitude and phase angle combination is then compared with the previous highest efficiency. By sweeping all the possible current magnitudes, the

efficiency found by Algorithm 1 is guaranteed to be optimal. After the optimal efficiencies $\eta_{opt}(\tau, \omega_r)$ are found for all the torque and speed combinations in the efficiency map, the efficiency contours can be drawn.

The flowchart of the overall simulation process is shown in Fig. 3.4. Among the four steps, the first two correspond to the database generation process, which are calculated beforehand. Only the last two steps are needed to run in the powertrain simulation/optimization.

3.5 Results

3.5.1 Base Design Efficiency Map Validation

A model of the UQM PowerPhase® 145, a 400Nm, 145kW surface-mount PMSM from UQM Technologies [54], is used in this section for illustration purposes. The geometry of the machine used in the 2D FEA is shown in Fig. 3.5. The losses are calculated using the relationships presented in Section 3.2.2. For winding conduction loss, the resistivity of copper is adjusted to $160°\mathrm{C}$, which is the winding temperature limit for continuous operation provided by the machine manufacturer. The core losses are calculated by Steinmetz's Equation (3.10), with coefficients $c_1 = 16.59, c_2 = 1.53, c_3 = 1.90$, which are determined by fitting the data from steel lamination datasheet. An empirical corrective coefficient $c_e = 2$ was used to account for the manufacturing process [65].

As an example, the loss density distribution solved by FEA at the operating point of $I = 400$A, $\theta_I = 140°$, 4000RPM is shown in Fig. 3.6. As discussed in Section 3.4.1, a wide range of current magnitudes and phase angles are simulated to build the base design database. Fig. 3.7 shows the rotor-position-dependent torque at different current magnitudes with $\theta_I = 90°$. The average torque within a period is used for the efficiency map calculation. Fig. 3.8 shows the torque vs. current phase angle curves at different current magnitudes. In practice, only the range of $90° \leq \theta_I \leq 180°$ (i.e. direct-axis current $I_d \leq 0$,

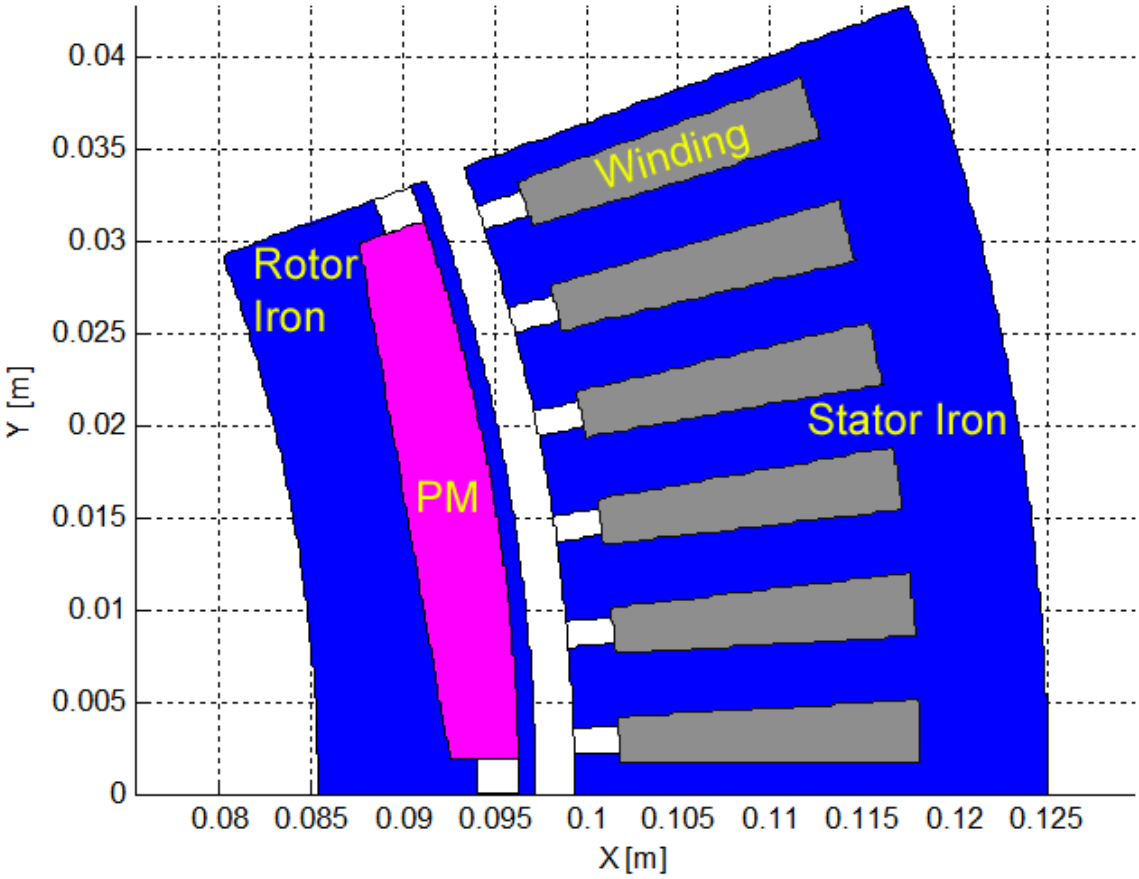

Figure 3.5: 2D geometry of UQM PowerPhase® 145.

quadrature-axis current $I_q \geq 0$) is of interest for the motoring mode of a PMSM. Thus, there is no need to sweep θ_I from 0° to 180° in the simulation.

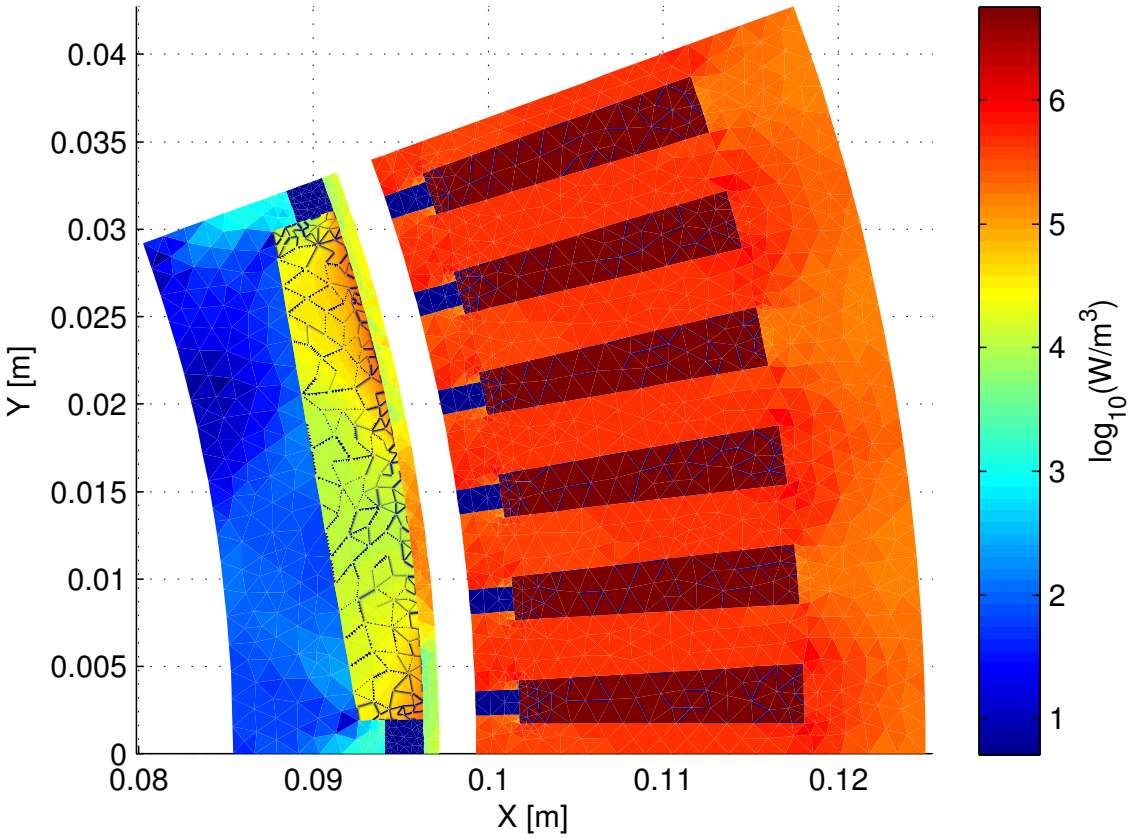

Figure 3.6: Loss distribution at 400A, 140°, 4000RPM (logarithmic scale)

Comparing the MS FEA results with MQS, torque, flux linkage, and core loss calculated from the two formulations are almost identical. MQS FEA is more accurate for AC winding resistance and PM eddy current loss calculation. But calculating AC winding resistance in MQS FEA requires modeling individual wires/strands in the slot, which dramatically increases the number of elements in the mesh. Thus, traditionally it is not uncommon to use DC resistance in MQS FEA; e.g., [42, 47]. If DC resistance is used, both MQS and MS FEA will have the same accuracy in the winding loss calculation. For PM eddy current losses, although MS FEA overestimates PM losses as discussed in Section 3.2.2.3, the total amount of PM losses is usually small, and so the impact on efficiency map calculation

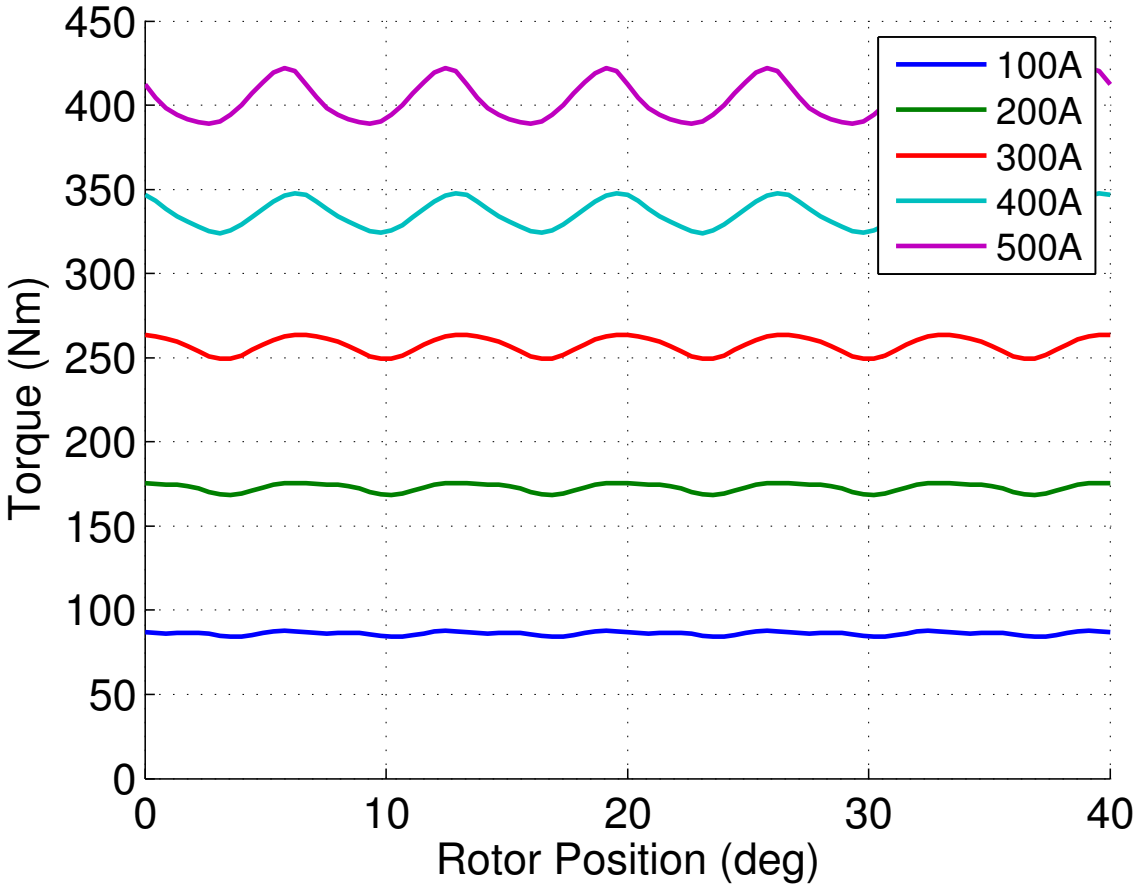

Figure 3.7: Torque vs. rotor position at different current magnitudes, $\theta_I = 90°$.

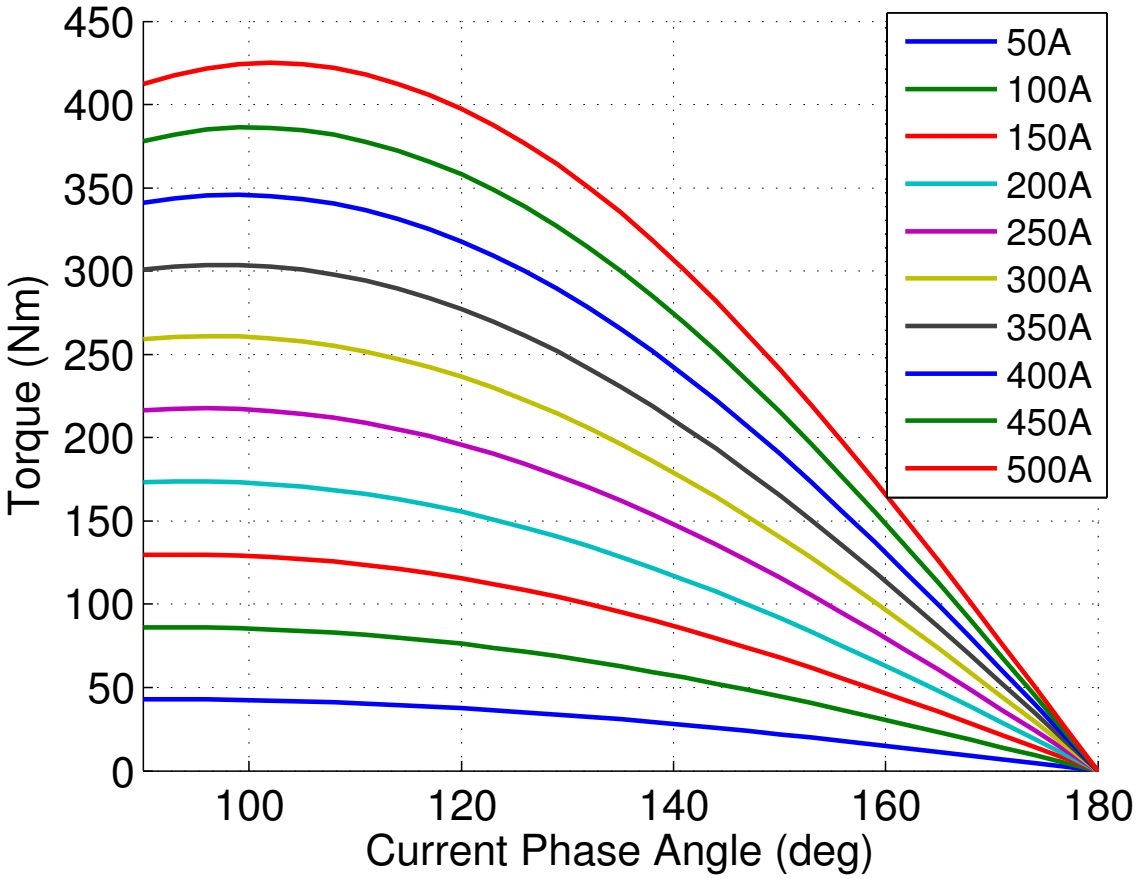

Figure 3.8: Torque vs. phase angle at different current magnitudes.

Table 3.1: Comparison of MS and MQS FEA at 8000RPM, 450A, 157.7°

	MS	MQS
Torque τ (Nm)	164.5	164.50
Peak flux linkage λ_{pk} (Vs)	0.02471	0.02512
Winding loss P_{wind} (W)	6484.3	6484.3
Core loss P_{core} (W)	2893.2	2889.8
PM loss P_{PM} (W)	56.4	41.1
P_{PM}/P_{mech}	0.04%	0.03%

Table 3.2: Comparison of MS and MQS FEA at 8000RPM, 250A, 178.9°

	MS	MQS
Torque τ (Nm)	4.47	4.45
Peak flux linkage λ_{pk} (Vs)	0.03773	0.03769
Winding loss P_{wind} (W)	2001.4	2001.4
Core loss P_{core} (W)	2662.4	2662.2
PM loss P_{PM} (W)	15.1	10.7
P_{PM}/P_{mech}	0.4%	0.3%

is negligible. For example, two operating points are simulated at the maximum speed of 8000RPM for the UQM machine using MS and MQS FEA, with results shown in Table 3.1 and 3.2. As can be seen in the tables, MS FEA overestimates PM loss by up to 41.1% at low torque. But the ratio of PM loss P_{PM} to output mechanical power $P_{mech} = \tau\omega_r$ is small, thus such overestimation in PM loss has negligible impact on efficiency calculation.

The efficiency map simulated using MS FEA and the techniques discussed in Section 3.4.3 is compared with the efficiency map provided in the UQM PowerPhase® 145 datasheet [54], which was determined through experimental measurements. The current and bus voltage limits used in the simulation are 500A and 340V, according to the datasheet, and six-step operation [73] is used in the field weakening region. As can be seen from Fig. 3.9, the simulated torque-speed curve and the overall shape of the efficiency contour lines matches well with the datasheet. The peak power calculated from the simulation (151.0kW) is 4.1% larger than the rated peak power of 145kW, while the peak torque in the constant torque operating region at low speeds calculated from the simulation (425.2Nm) is 6.3%

larger than the rated peak torque of 400Nm.

The over-estimation in peak torque at low speeds is possibly due to the uncertainty in B-H curve caused by the manufacturing process of the laminations. It is also possible that the datasheet map does not utilize the reluctance torque (although it is small for surface-mount PMSM) at low speeds, i.e. not in max torque per ampere (MTPA) operation. For example, at the current limit of 500A, torque is 412.3Nm when $I_d = 0A$, $I_q = 500A$, while increasing to 425.2Nm at MTPA operation ($I_d = -104A$, $I_q = 489A$). The over-estimation in efficiency is possibly due to 1) the neglect of AC winding resistance; 2) the core loss corrective coefficient due to manufacturing process ($c_e = 2$) used in this paper is conservative. A coefficient higher than 2 is often observed, as suggested in [65]. Better accuracy can be achieved by tuning c_e, since it is fundamentally difficult to determine it theoretically.

3.5.2 Scaled Design Examples

In this section, an MS FEA database that contains 151 current magnitudes and 31 phase angles are used in the scaling process. The same current and bus voltage limits of 500A and 340V are used as in Section 3.5.1 purely for comparison purposes. In practice, users can choose different limits according to their specific cases.

Using the proposed techniques, the torque-speed curve of the electric machine can be adjusted, and the high efficiency region ("sweet spots") on the efficiency map can be re-shaped according to different design specifications. For example, Fig. 3.10 shows a scaled design with dimensional scaling factor $\alpha = 1.6$ and effective number of turns $N = 0.78$ (7 turns, 9 parallel paths), and 18 poles. As shown in the figure, this design has good efficiency performance at mid speed, high torque regions around 510Nm, 2700RPM. By decreasing the number of turns while increasing the size of the machine, the scaled design has higher peak torque as the base design, and the sweet spots are moved upward. This is achieved at the price of using more materials, and thus a higher cost.

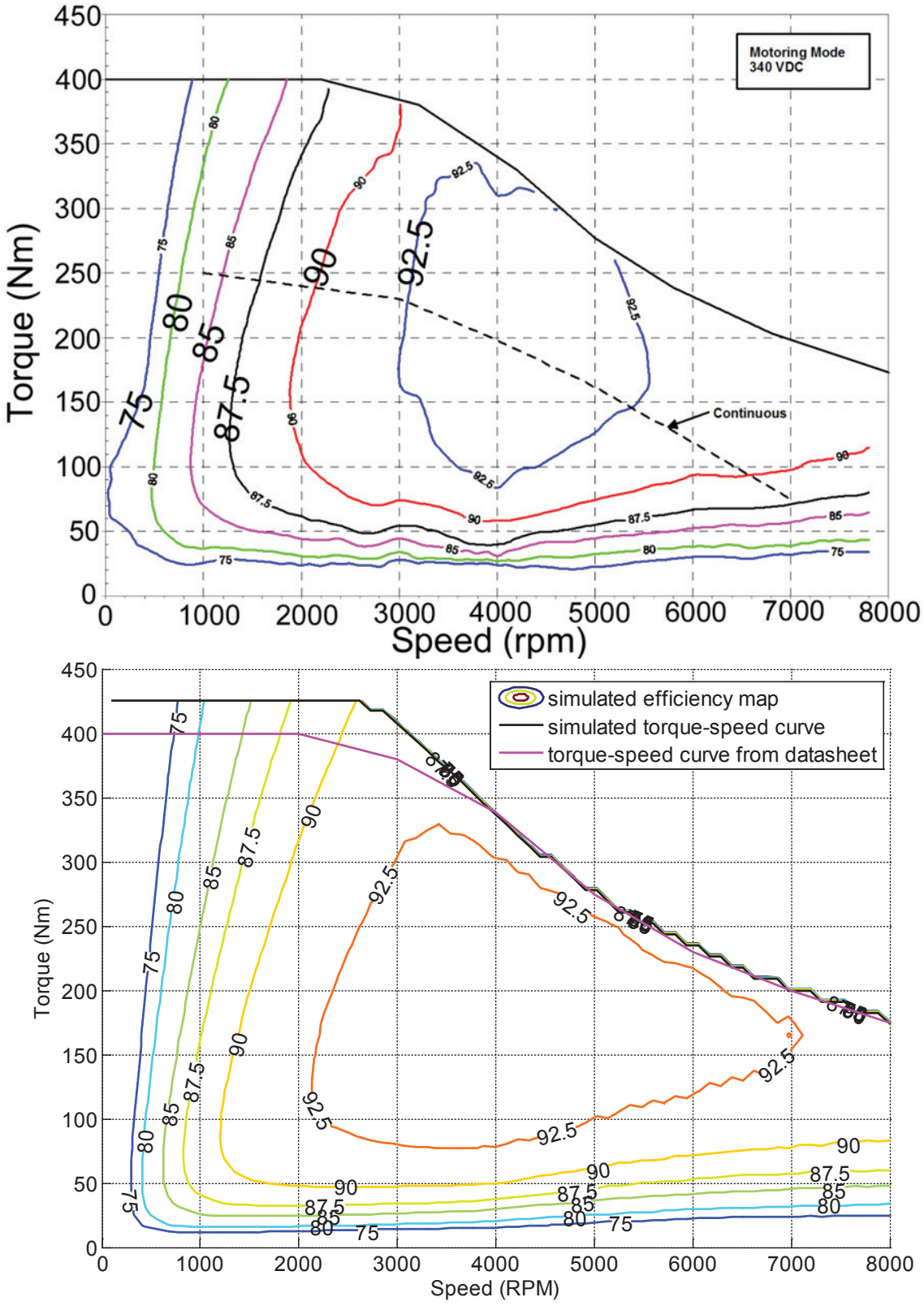

Figure 3.9: Datasheet [54] (top) and simulated (bottom) efficiency map comparison for UQM PowerPhase® 145

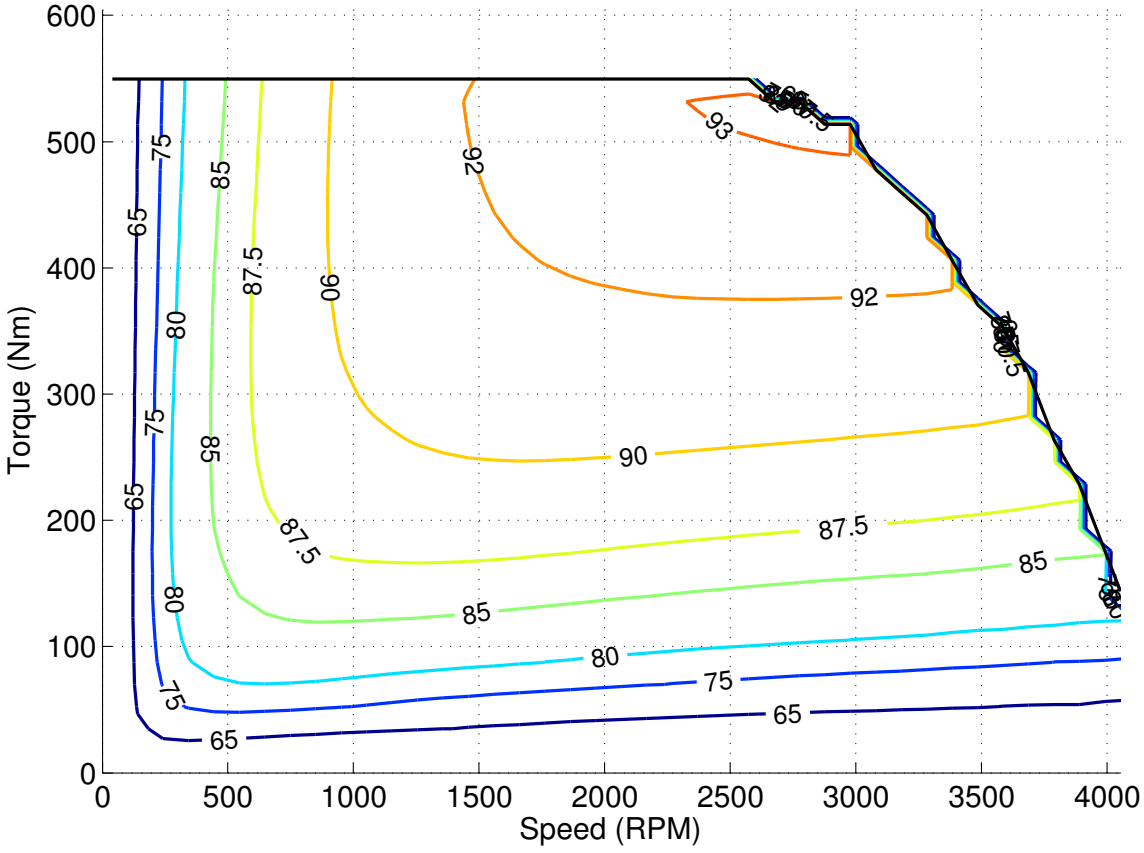

Figure 3.10: Efficiency map of the $\alpha = 1.6$, $N = 7/9$ design

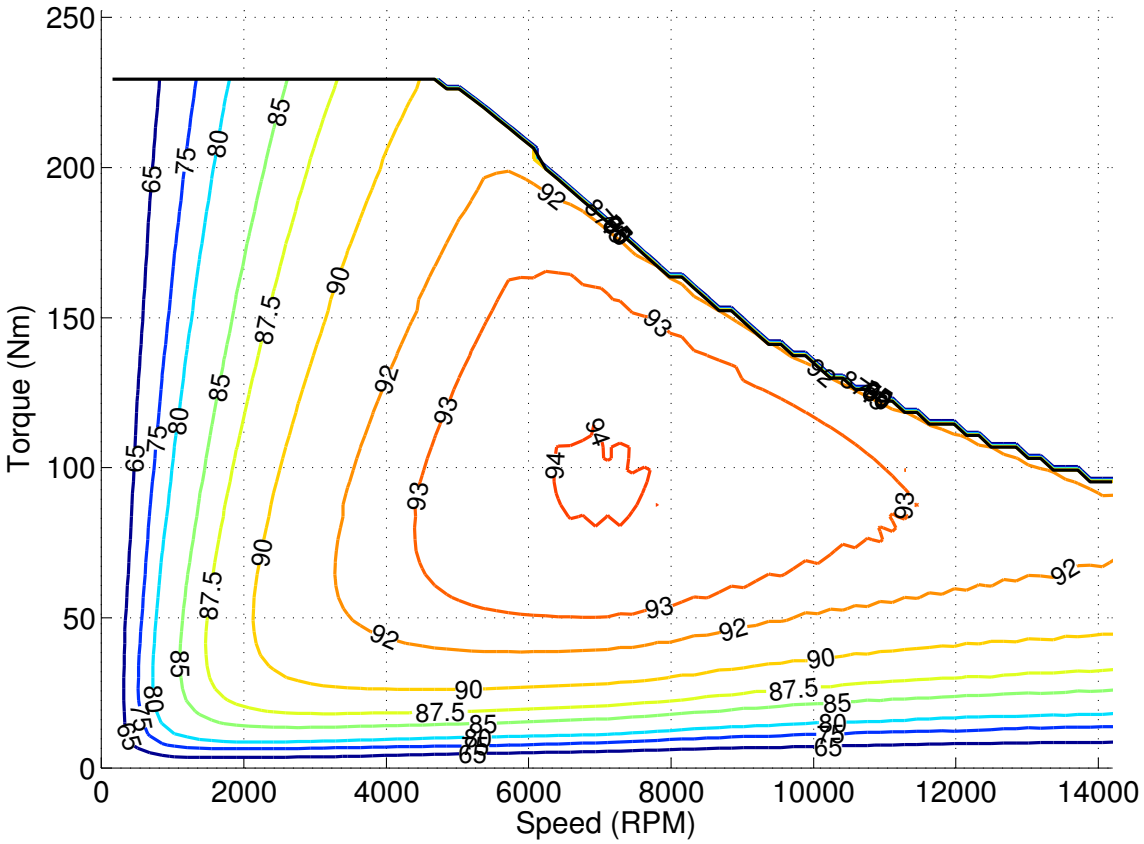

Figure 3.11: Efficiency map of the $\alpha = 0.8$, $N = 4/3$ design

Fig. 3.11 shows another design with $\alpha = 0.8$, $N = 1.33$ (4 turns, 3 parallel paths). As shown in the figure, this design has good efficiency performance at mid speed, low torque regions around 95Nm, 7000RPM. Fig. 3.12 shows another scaled design with $\alpha = 1.3$, $N = 2$, and 18 poles. As shown in the figure, by increasing the number of turns and size, much higher peak torque of 905Nm can be achieved while having sweet spots in the mid speed, mid torque range around 340Nm, 1750RPM.

It is noted that an arbitrarily scaled design may not be feasible in practice due to thermal and structural limitations. From the thermal perspective, when the number of turns increases, for the same terminal current magnitude, heat generation increases due to the increase in total slot current, while cooling capacity remains the same due to the same dimensions and thus the same cooling surface area. This may result in over-heating and the

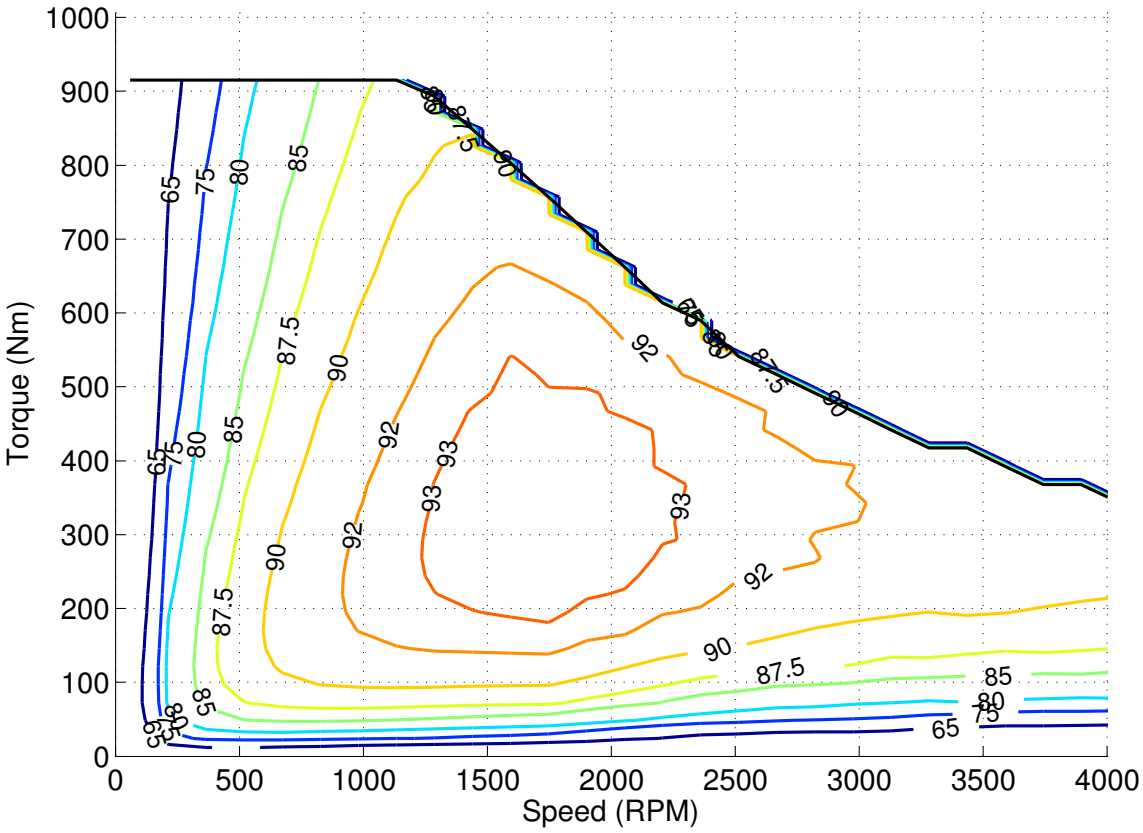

Figure 3.12: Efficiency map of the $\alpha = 1.3$, $N = 2$ design

predicted peak torque from electromagnetic FEA may be not practical to achieve. To accurately predict the peak torque and continuous torque operating regions (which are defined as the peak torque a design can produce for a short period of time and in steady-state, respectively), a scalable thermal model is needed to couple with the electromagnetic model. From the structural perspective, the rotor experiences centrifugal forces when rotating, and it is a major challenge in high-speed PMSM design to retain the PMs at high-speed operations [74]. Thus, when the scaled design has a larger speed range, the structural design may become invalid.

To address this concern, both analytical and numerical methods can be used for rotor stress analysis [74] and determining the feasibility of a scaled design from the structural perspective. It is also possible to develop a dimensional scaling framework similar to [44] based on the fundamental governing PDEs of structural analysis.

3.5.3 Computation Time

The simulations were run on a workstation with Intel Xeon E7-8860 @ 2.27GHz CPU. The computation time involved in the proposed techniques consists of two parts:

1. The pre-calculation of the FEA database which corresponds to the first two steps in Fig. 3.4.

2. The generation of scaled designs and their efficiency maps which corresponds to the last two steps in Fig. 3.4.

Since the FEA solutions are independent of one another for different operating points, the computation time for generating the base design database can be linearly reduced through parallel computing. Parallel computing can also linearly reduce the computation time for generating an efficiency map of the scaled design, since the process of finding the optimal efficiency operating points for a given torque and speed are also independent.

Thus, the units of "core-hour" and "core-minute" are used in the following results, which is calculated by multiplying the number of CPU cores used with computation time.

The average computation time is 16.9sec for a nonlinear 2D MS FEA solve of one combination of current amplitude and phase angle with 91 rotor positions. That corresponds to 22.0 core-hours for generating a base design database with 151 current amplitudes and 31 phase angles. It takes 66.0 core-hours in total to generate three databases for three different number of poles.

After the FEA database is built, it takes about 1 to 5 core-minutes to generate an efficiency map for a scaled design, depending on the chosen scaling parameters. Some scaled designs require more computation time, since more operating points need to be checked in the database. For example, under the same terminal current limit, a $N = 4$ design requires checking more current magnitudes than a $N = 2$ design, thus taking more computation time to generate its efficiency map. Nonetheless, the computation time of several core-minutes for generating a scaled machine design and its efficiency map is much faster than solving the FEA for the scaled design, and is fast enough for the purpose of powertrain level simulation and optimization.

3.6 Conclusion

Three scaling techniques, dimensional scaling, number-of-turns scaling, and slot/pole scaling, are proposed in this chapter and used to generate new designs of electric machines based on the finite element model of an existing base design. By using the proposed MS scalable model, the efficiency maps of the scaled designs can be efficiently generated, without the necessity of re-solving FEA for these designs, which dramatically reduces computation time. Results show that, in the scaled designs, the torque-speed curves can be adjusted and the efficiency maps can be re-shaped in ways favorable to powertrain design. These techniques can be also useful for powertrain optimization for given specifications or driving

cycles.

CHAPTER 4

Computationally-Efficient Electromagnetic-Thermal Coupled Scalable Model for Electric Machines

4.1 Introduction

The efficiency map of an electric machine is constrained by temperature, since the torque capability and losses are both affected by temperature. Furthermore, the continuous operating region, which is defined as the operating points where the machine can safely run at steady state without reaching the temperature limits of the winding insulation and PM materials, can provide useful information for powertrain design and optimization. To determine the continuous operating region, a thermal model is needed. Furthermore, an accurate prediction of demagnetization also requires temperature information in the PM, since the intrinsic coercivity of the PM material is affected by temperature.

Based on the work presented in Chapter 3, a CE EM-thermal coupled model based on 2D MS FEA and 3D thermal static FEA is developed to add the capability of continuous operating region prediction and temperature-dependent demagnetization check to the previous model.

4.2 Static Thermal Modeling

The PDE associated with thermal conduction in steady state is given as follows:

$$-\kappa \nabla^2 T = q_{loss}, \tag{4.1}$$

where T is the continuum temperature and κ is the thermal conductivity of the machine materials. Using FEA techniques, the machine geometry is meshed and the above PDE can be discretized into a differential equation as follows:

$$\mathbf{K}\vec{t} = \vec{q}, \tag{4.2}$$

where $\vec{t}$ is the nodal temperature vector of the finite element mesh, $\mathbf{K}$ is the finite element matrix which corresponds to thermal conductivity. The vector $\vec{q}$ corresponds to the excitation of the thermal model, and can be categorized as follows:

$$\vec{q} = \sum_k \vec{p}_k \odot \vec{f}_k + \sum_l h_l \left(\vec{t}_c - \vec{t}\right) \odot \vec{g}_l, \tag{4.3}$$

where $\odot$ denotes element-wise multiplication. The vectors $\vec{p}_k \odot \vec{f}_k$ correspond to different loss mechanisms of the machine, including conduction losses, core losses, and PM eddy-current losses, which are determined by the 2D magneto-static FEA. Vectors $\vec{p}_k$ are the nodal loss density vectors, and $\vec{f}_k$ are the normalized internal forcing vectors generated from FEA assembly. Likewise, the vectors $h_l \left(\vec{t}_c - \vec{t}\right)$ correspond to the heat flux density at each boundary node due to convective heat transfer on different boundaries of the machine, representing Neumann boundary conditions of the finite element model. Scalars h_l are the heat transfer coefficients on the convective boundaries, and $\vec{g}_l$ are the normalized boundary external forcing vectors generated from FEA assembly.

By combining (4.2) and (4.3), the static thermal model can be written as:

$$\left[\mathbf{K}+\sum_{l} diag\left(h_l\vec{g}_l\right)\right]\vec{t} \;=\; \sum_{k}\vec{p}_k\odot\vec{f}_k+\sum_{l}h_l\vec{t}_c\odot\vec{g}_l, \tag{4.4}$$

$$\mathbf{K}'\vec{t} \;=\; \vec{q}\Rightarrow\vec{t}=\mathbf{K}'^{-1}\vec{q}. \tag{4.5}$$

where $diag\left(\vec{v}\right)$ denotes a diagonal matrix with vector $\vec{v}$ in its diagonal entries, and $\mathbf{K}'=\mathbf{K}+\sum_{l} diag\left(h_l\vec{g}_l\right)$.

The continuous operating region of an efficiency map is determined by the temperature of the winding and PM regions. A 3D static thermal FEA model is used to predict the steady-state temperature in the winding and PM for each operating point in the efficiency map. The operating points whose steady-state temperatures do not exceed the winding insulation limit and the temperature limit of the PM material are deemed as continuous operating points.

Since the electric resistivity of copper is a function of temperature, and can increase by 54.07% with a temperature rise from $20°\mathrm{C}$ to $160°\mathrm{C}$, it is necessary to use the temperature-dependent winding conduction loss as the input to the thermal model to form an iterative algorithm:

$$\vec{p}_{cond,i+1}=\vec{p}_{cond,i}\odot\left(\vec{1}+\beta\Delta\vec{t}\right), \tag{4.6}$$

where $\vec{p}_{cond,i}$ is the nodal winding conduction loss density vector at temperature $\vec{t}_i$, and $\beta=0.003862\mathrm{K}^{-1}$ is the temperature coefficient of the electric resistivity of copper. The temperatures of the electromagnetic-thermal coupled model is calculated by iteratively solving $\vec{t}=\mathbf{K}'^{-1}\vec{q}(\vec{t})$ until convergence for each operating point, where the excitation vector $\vec{q}$ is temperature-dependent and updated at each iteration. LU decomposition of $\mathbf{K}'$ is pre-calculated and used for the matrix-vector solving to reduce the computation time. The iterative process is shown in Algorithm 4.1.

Similar to the previous model presented in Chapter 3, in this EM-thermal coupled

Algorithm 4.1: EM-thermal coupled analysis

Input: loss information from EM FEA, cooling parameters, FEA model.
Result: converged max. temperature in winding and PM.

initialization;
while *error* $>$ *tolerance* **do**
  $\vec{p}_{cond,i+1} \leftarrow \vec{p}_{cond,i} \odot \left(1 + \beta \vec{\Delta t}\right)$;
  Calculate $\vec{q}_{i+1}$ based on $\vec{p}_{cond,i+1}$;
  $\vec{t}_{i+1} \leftarrow \mathbf{K'}^{-1} \vec{q}_{i+1}$ using LU decomposition;
  $\Delta \vec{t} \leftarrow \vec{t}_{i+1} - \vec{t}_i$;
  $\vec{t}_i \leftarrow \vec{t}_{i+1}$;
  $error \leftarrow \|\Delta \vec{t}\|$;
end
$T_{winding} \leftarrow \max\left(\vec{t}_i \left(winding\_indecies\right)\right)$;
$T_{PM} \leftarrow \max\left(\vec{t}_i \left(PM\_indecies\right)\right)$;

model, torque, power losses, flux, magnetic field intensity, and temperature information over a range of current magnitudes and phase angles is calculated by the 2D MS FEA and 3D thermal static FEA for the base design, and a FEA database is constructed for later use.

4.3 Thermal Scaling

To be effectively integrated in the previous scalable MS model presented in Chapter 3, the thermal model also needs to be scalable. The temperature solution vector $\vec{t} = \mathbf{K'}^{-1} \vec{q}(\vec{t})$ in Section 4.2 can be decomposed into two components:

$$\vec{t} = \left[\mathbf{K} + \sum_l diag\left(h_l \vec{g}_l\right)\right]^{-1} \left(\sum_k \vec{p}_k \odot \vec{f}_k + \sum_l h_l \vec{t}_c \odot \vec{g}_l\right) \tag{4.7}$$

$$= \vec{t}_{loss} + \vec{t}_h \tag{4.8}$$

where $\vec{t}_{loss}$ is the temperature contribution from losses, and $\vec{t}_h$ is the contribution from boundary heat transfers.

The proposed thermal scaling happens after the dimensional scaling. When the dimensions are scaled by a factor of α, the 3D FEA thermal model is also scaled. From the

FEA assembly process [75], by using linear tetrahedral elements, the stiffness matrix $\mathbf{K}$ is proportional to α:

$$\mathbf{K} = [\mathbf{K_e}] = \left[\sum_{A,B=1}^{N_{shape}} \iiint_{V_e} \frac{\partial N_A}{\partial x_i} \kappa_{ij} \frac{\partial N_B}{\partial x_j} dV \right] \propto \frac{1}{\alpha} \frac{1}{\alpha} \alpha^3 = \alpha. \tag{4.9}$$

where $\mathbf{K_e}$ is the element-level stiffness matrix, $[*]$ denotes the FEA assembly process, N_A and N_B are shape functions, N_{shape} is the number of shape functions (4 for linear tetrahedral element), V_e is the volume of the element, $i, j = 1, 2, 3$ correspond to 3D coordinates, and κ_{ij} is the i, j-th component of the thermal conductivity tensor. In this section, the Einstein summation convention is used.

Similarly, the internal forcing vectors $\vec{f}_k$ are proportional to α^3:

$$\vec{f}_k = \left[\vec{f}_{int,e} \right] = \left[\sum_{A=1}^{N_{shape}} \iiint_{V_e} N_A dV \right] \propto \alpha^3. \tag{4.10}$$

where $\vec{f}_{int,e}$ is the element-level internal forcing vector.

The boundary external forcing vectors $\vec{g}_l$ are proportional to α^2:

$$\vec{g}_l = \left[\vec{f}_{ext,e} \right] = \left[\sum_{A=1}^{N_{shape}-1} \oint_{\Omega_e} N'_A ds \right] \propto \alpha^2, \tag{4.11}$$

where $\vec{f}_{int,e}$ is the element-level external forcing vector, and N'_A is the shape function for boundary surface elements.

Furthermore, the conduction loss density $\vec{p}_{cond}$ is proportional to J^2 according to Joule's law. Thus by using (3.36),

$$\vec{p}_{cond} \propto J^2 \propto \frac{1}{\alpha^2}. \tag{4.12}$$

The hysteresis core loss density $\vec{p}_{core}$ is a function of $\vec{B}$, $\vec{H}$ and electrical frequency f_e:

$$\vec{p}_{core} = f_e \oint \vec{H} d\vec{B}, \tag{4.13}$$

where $\vec{B}$ and $\vec{H}$ are unchanged during dimensional scaling according to (3.30), and $f_e \propto \frac{1}{\alpha^2}$ according to (3.34). Thus, $\vec{p}_{core} \propto \frac{1}{\alpha^2}$.

By assuming that the heat transfer coefficient on the boundary scales with $\frac{1}{\alpha}$, i.e. $h_{l,\alpha} = \frac{1}{\alpha} h_{l,1}$, we have:

$$\mathbf{K}' = \mathbf{K} + \sum_l diag\left(h_l \vec{g}_l\right) \propto \alpha, \tag{4.14}$$

$$\mathbf{K}'^{-1} \propto \frac{1}{\alpha}. \tag{4.15}$$

By combining these relationships, it can be shown that both $\vec{t}_{loss}$ and $\vec{t}_h$ are unchanged in dimensional scaling:

$$\vec{t}_{loss} = \mathbf{K}'^{-1} \left(\sum_k \vec{p}_{loss,k} \odot \vec{f}_{loss,k} \right) \propto \frac{1}{\alpha} \frac{1}{\alpha^2} \alpha^3 = 1, \tag{4.16}$$

$$\vec{t}_h = \mathbf{K}'^{-1} \left(\sum_l h_l \vec{g}_l \right) \propto \frac{1}{\alpha} \frac{1}{\alpha} \alpha^2 = 1. \tag{4.17}$$

As a result, the temperature in the scaled design can be determined directly and efficiently from the temperature solution of the base design without resolving FEA:

$$\begin{aligned} \vec{t}_\alpha &= \vec{t}_{loss,\alpha} + \vec{t}_{h,\alpha} \\ &= \vec{t}_{loss,1} + \vec{t}_{h,1} \\ &= \vec{t}_1. \end{aligned} \tag{4.18}$$

Note that the assumption on cooling capability $h_l \propto \frac{1}{\alpha}$ is not unfounded, since when the dimensions of the machine increase, the heat generation increases linearly according to

Section 3.39, while the area of cooling surface increases quadratically. Thus, smaller heat transfer coefficients for larger machines would be enough to cool the machine down to the same temperature. Similarly, for smaller machines, better cooling capability is required to maintain the same temperature as the base design, which matches intuition.

4.4 Simulation

The process of the proposed EM-thermal coupled scaling is presented in this section. Since most of the process is same as presented in Section 3.4, only the part related to the coupled scalable thermal model is discussed.

4.4.1 Pre-calculation of Base Design FEA Database

In the database generation process, the MS FEA database is generated first, in the same way as discussed in Section 4.4.1. The thermal FEA database is optional and only necessary when the user needs the feature of estimating the continuous operating region. For the same range of current magnitude and phase angle used in the MS FEA database generation, the iterative static thermal FEA algorithm (Algorithm 4.1) is conducted over a range of rotor speeds. This is due to the fact that, unlike the speed-independent MS FEA, the thermal model is speed-dependent due to the air-gap heat transfer as shown in Section 4.2. The initial loss information used in the thermal FEA is from the previously generated MS FEA database, with normalized core losses and eddy-current losses adjusted to the corresponding rotor speed in post-processing using (3.9) and (3.21). Finally, the nodal temperature vectors, calculated by the thermal FEA, are stored in a database as 3D lookup tables, with current magnitude, phase angle, and rotor speeds as inputs.

4.4.2 Efficiency Map Generation and Continuous Operating Region Estimation

In addition to the efficiency map generation process presented in Section 3.4.3, the continuous operating region can be estimated using the proposed scalable thermal model. The continuous operating region inside an efficiency map is determined by the temperature of the winding and PM region. The operating points whose steady-state temperature do not exceed the winding insulation limit and the temperature limit of the PM material are deemed as continuous operating points. Algorithm 1 is thus amended by adding the calculation of temperatures at the optimal operating points, as shown in Line 10 and 11 of Algorithm 4.2. By using the temperature information ($T_{opt,wind}(\tau, \omega_r)$ and $T_{opt,PM}(\tau, \omega_r)$) determined in Algorithm 4.2, the continuous operating region can be drawn as the intersection of the areas that are within the winding insulation limit and the PM temperature limit. The flowchart of the overall EM-thermal coupled scaling process is shown in Fig. 4.1.

Algorithm 4.2: Optimal operating point search with temperature calculation

Input: an operating point (τ, ω_r) on efficiency map

Data: the FEA database that contains torque, voltage, loss, field intensity, and temperature information for each (I, θ_I) combination at ω_r; V_{lim} and I_{lim} imposed by inverter

Result: the optimal operating point $(I_{opt}, \theta_{I,opt})$, its efficiency η_{opt}, and max. temperature in winding ($T_{opt,wind}$) and PM region ($T_{opt,PM}$)

$\eta_{test} \leftarrow 0$;
Determine I_{min}, the smallest I that can produce τ (i.e. the min. current operating point);
for I=I_{min} **to** I_{lim} **do**
    Search for θ_I that can produce τ at I using interpolation;
    if *found* **then** `// τ is achievable at I`
        if $V(I, \theta_I) \leq V_{lim}$ *and* $H(I, \theta_I) < H_{ci}$ **then**
            `// by using interplolation`
            Calculate losses and efficiency at (I, θ_I);
            if $\eta(I, \theta_I) > \eta_{test}$ **then**
                $\eta_{test} \leftarrow \eta(I, \theta_I)$;
                $T_{opt,wind} \leftarrow T_{wind}(I, \theta_I)$;
                $T_{opt,PM} \leftarrow T_{PM}(I, \theta_I)$;
                $(I_{opt}, \theta_{I,opt}) \leftarrow (I, \theta_I)$;
            end
        end
    end
end
$\eta_{opt} \leftarrow \eta_{test}$;

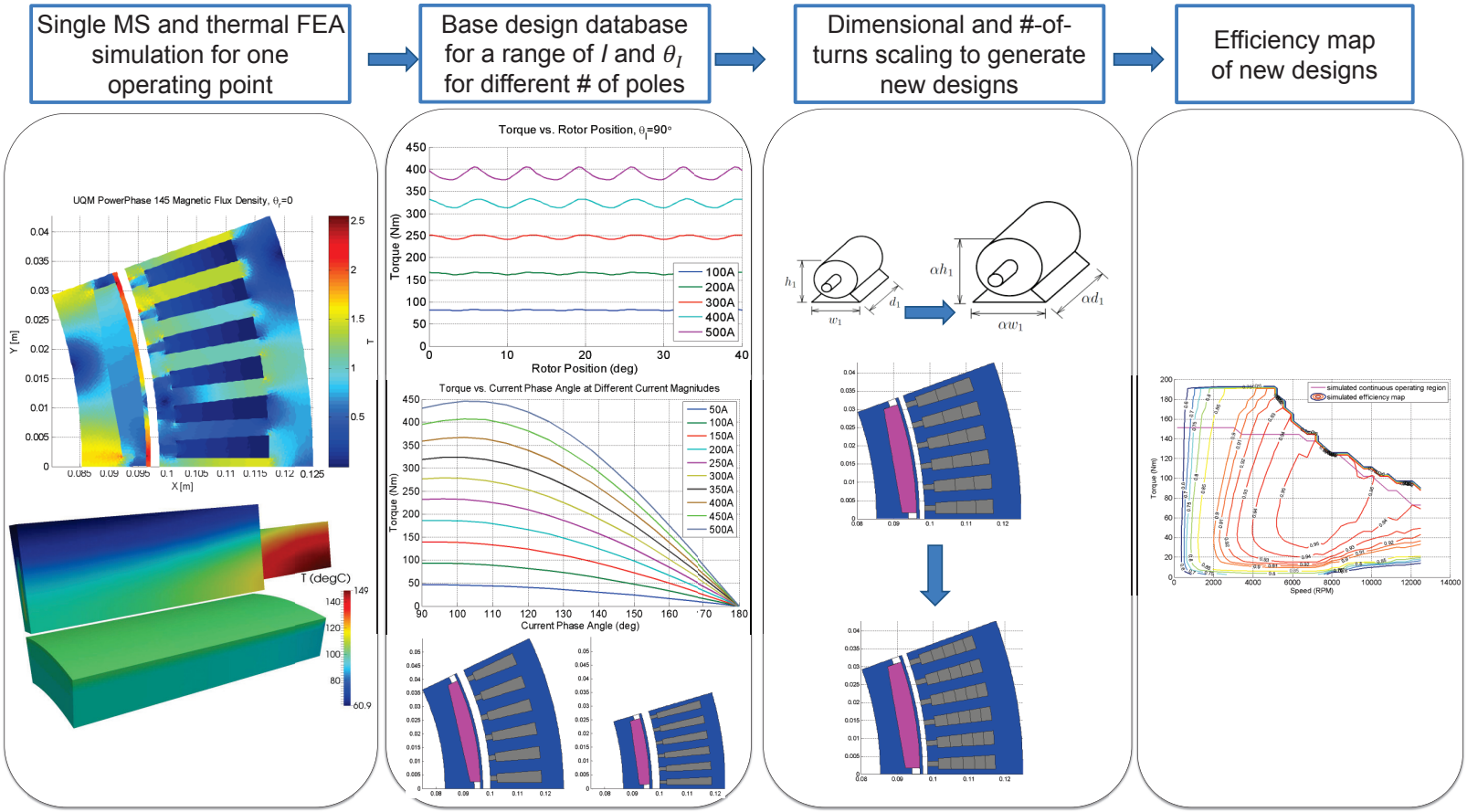

Figure 4.1: Flowchart of the overall EM-thermal coupled scaling process

4.5 Results

4.5.1 Base Design Efficiency Map Validation

The same UQM PowerPhase 145 machine model is simulated by using the proposed techniques. As an example, the loss and temperature distribution solved by FEA at the operating point of $I = 146.9$A, $\theta_I = 141.6°$, 4050RPM is shown in Fig. 4.2.

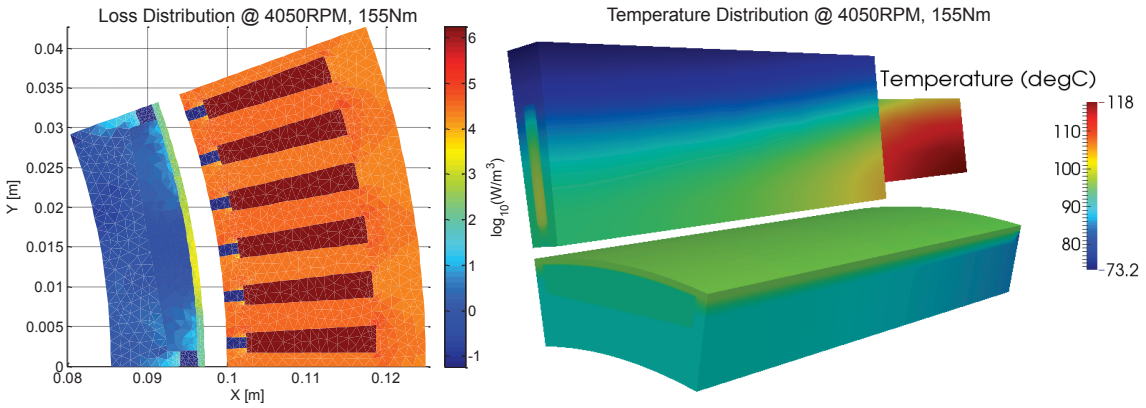

Figure 4.2: Loss (left) and temperature (right) distribution at 146.9A, $141.6°$, 4050RPM

The efficiency map is then simulated, where the estimated continuous operating region is determined by the intersection of the area covered by the $160°$C maximum winding temperature contour and the $150°$C maximum PM temperature contour for this machine based on information from the manufacturer. The winding temperature contour is shown in Fig. 4.3 and the PM temperature contour is shown in Fig. 4.4.

The simulated efficiency map is compared with the datasheet map, as shown in Fig. 4.5. As shown in the figure, the overall shape of the predicted continuous operating region matches with that in the datasheet map. The overestimation of the continuous region is possibly due to that the operating points used in the datasheet were not in MTPA operation thus requiring more currents to produce the same amount of torque.

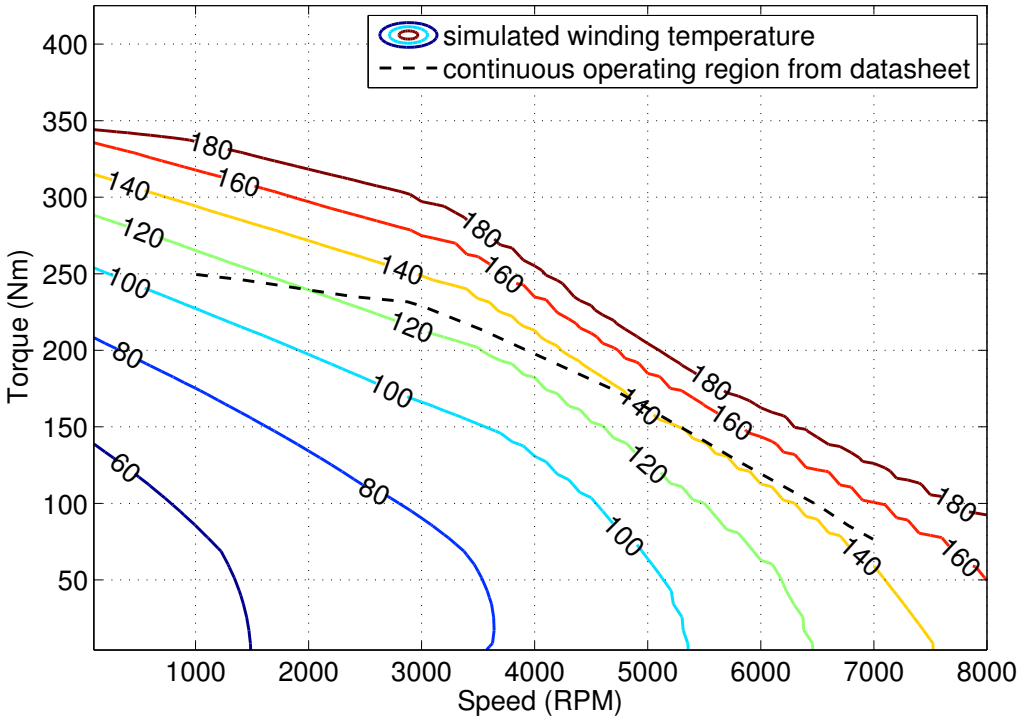

Figure 4.3: Simulated winding temperature contour map of UQM PowerPhase® 145

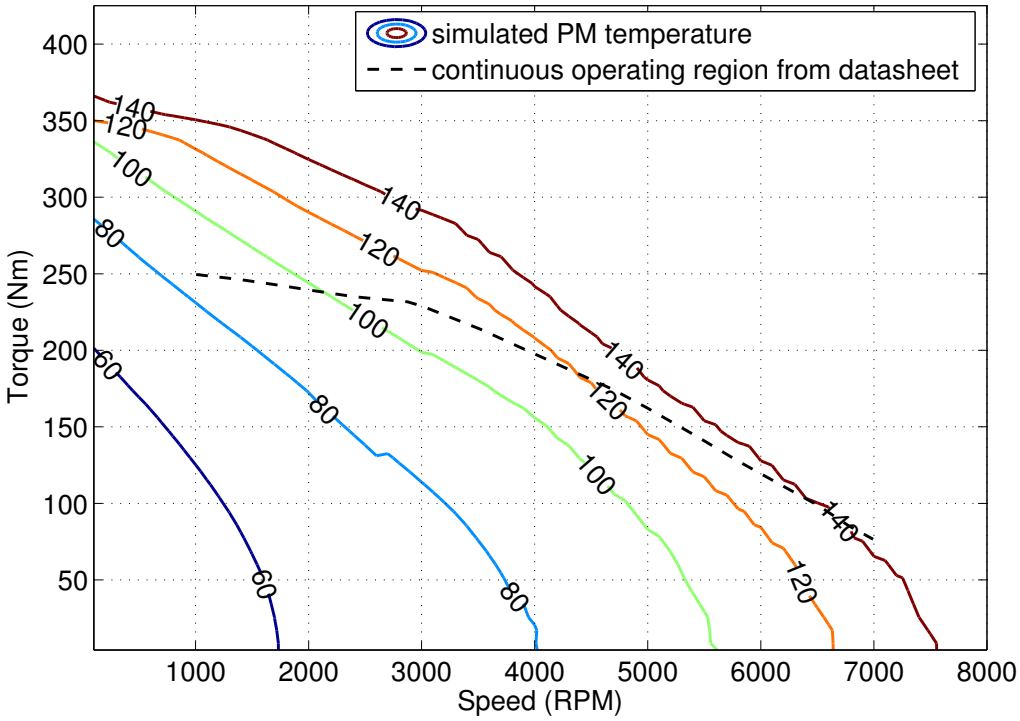

Figure 4.4: Simulated PM temperature contour map of UQM PowerPhase® 145

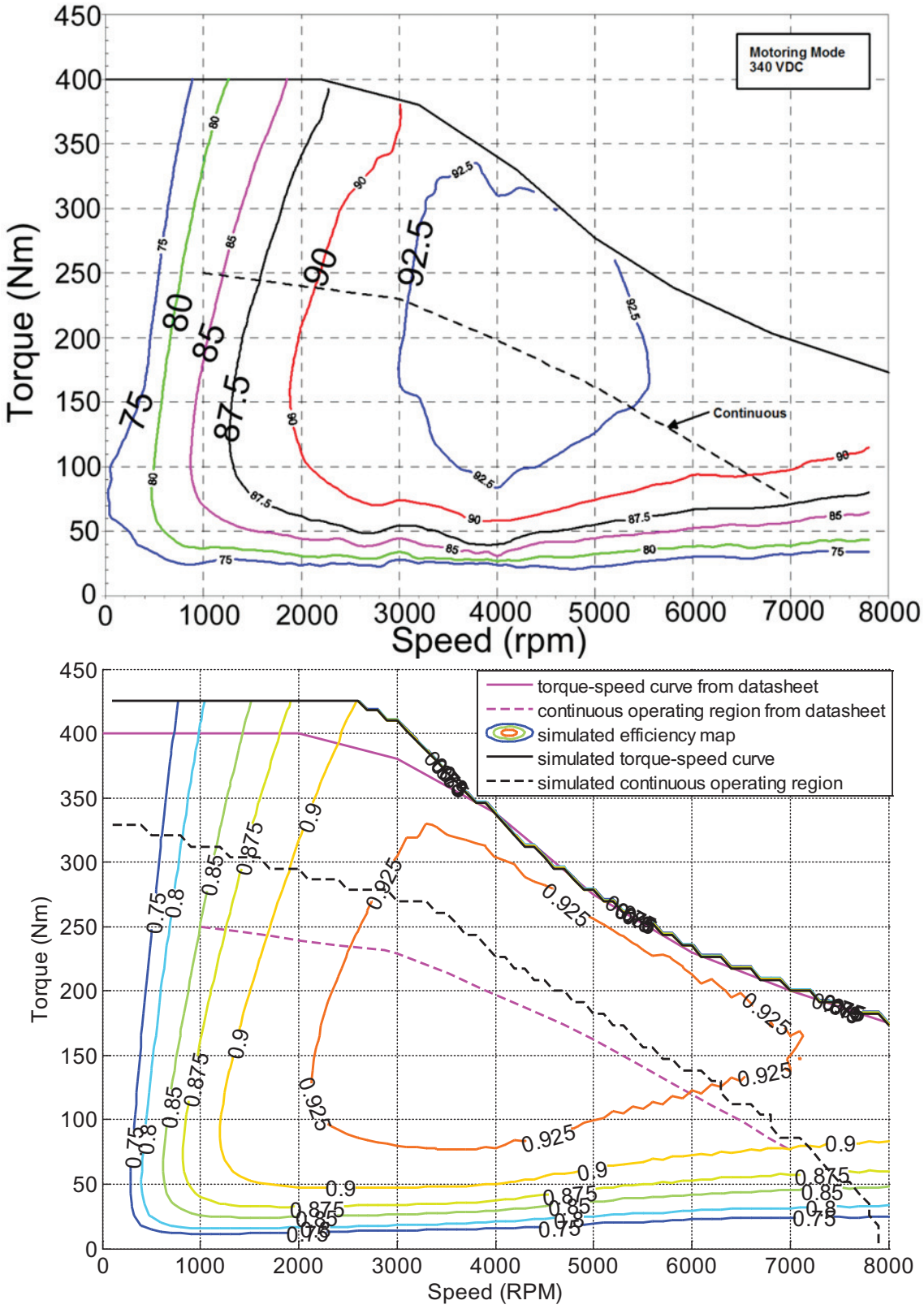

Figure 4.5: Datasheet [54] (top) and simulated (bottom) efficiency map and continuous operating region comparison for UQM PowerPhase® 145

4.5.2 Scaled Design Examples

In this section, an FEA database that contains 151 current magnitudes, 31 phase angles, and 6 rotor speeds are used in the scaling process. The same current and bus voltage limits of 500A and 340V are used as in Section 3.5.1 purely for comparison purposes. In practice, users can choose different limits according to their specific cases.

By using the proposed EM-thermal coupled scaling techniques, the torque-speed curve of the electric machine can be adjusted, and the high efficiency region ("sweet spots") and the continuous operating region on the efficiency map can be reshaped. For example, Fig. 4.6 shows a scaled design with dimensional scaling factor $\alpha = 1.2$ and effective number of turns $N = 1.11$ (10 turns, 9 parallel paths), and 18 poles. As shown in the figure, this design has good efficiency performance at mid speed, high torque regions around 350Nm, 4000RPM. Furthermore, by decreasing the number of turns while increasing the size of the machine, this scaled design has a better thermal performance, whose continuous operating region spans most of the area under the peak torque-speed curve. Furthermore, the simulation results suggest that this design can safely operate at its peak torque in steady state without hitting temperature limits.

Fig. 4.7 shows another design with $\alpha = 0.8$, $N = 2.33$ (7 turns, 3 parallel paths), and 18 poles. As shown in the figure, this design has good efficiency performance at mid speed, low torque regions around 40Nm, 5000RPM while having a peak torque of 200Nm. Furthermore, the highest efficiency region (the 94% contour line) is completely inside the continuous operating region, which suggests that this scaled design can safely operate at its highest efficiency in steady state without hitting temperature limits.

4.5.3 Computation Time

The average computation time for solving a given combination of current amplitude, phase angle, and rotor speed in 3D static thermal FEA on a workstation with Intel Xeon E7-8860 @ 2.27GHz CPU is 5.07sec. The total computation time to build the thermal

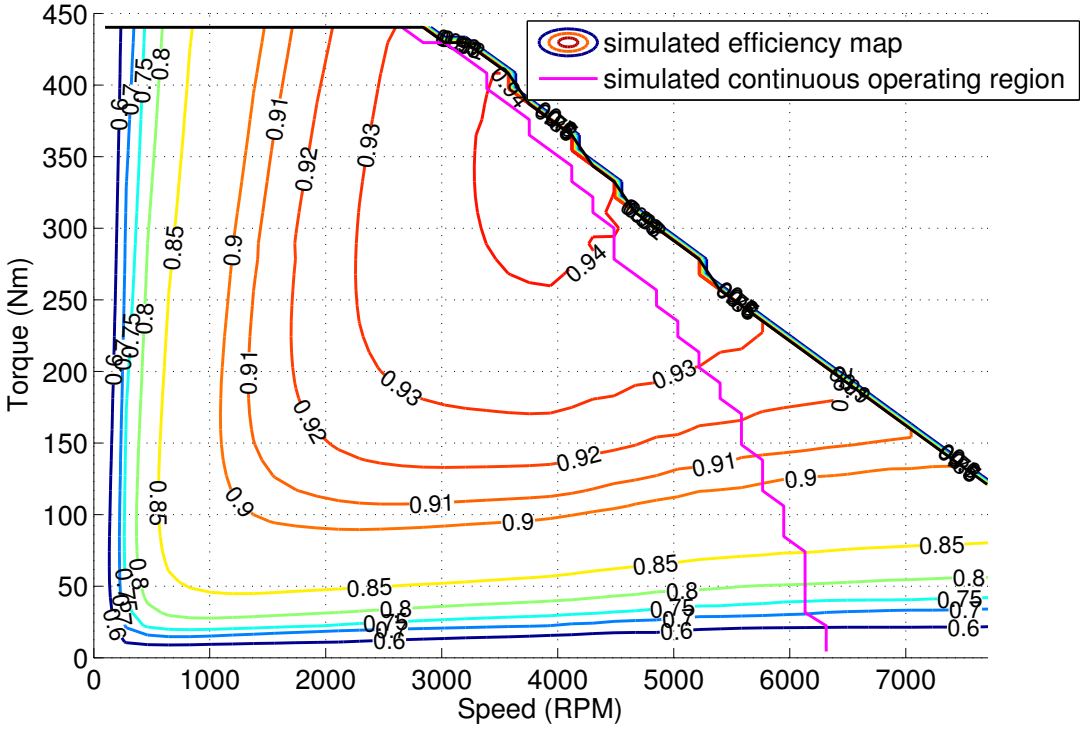

Figure 4.6: Efficiency map and continuous operating region of the $\alpha 1.2$, $N = 10/9$, 18-pole design

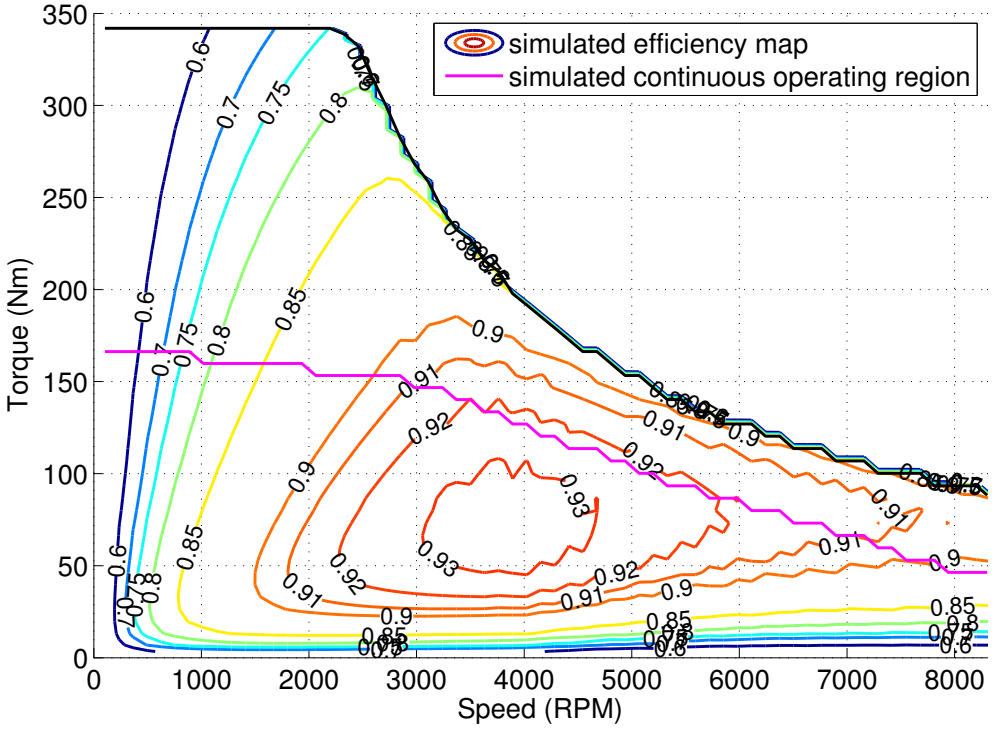

Figure 4.7: Efficiency map and continuous operating region of the $\alpha = 0.8$, $N = 7/3$, 18-pole design

FEA database is not a simple multiplication of the time for single solve by the total number of operating points in terms of current magnitudes, phase angles, and rotor speeds. For the purpose of estimating the continuous operating region, the computation time is much shorter than the multiplication, since there is no need to calculate the temperatures for the operating points that are above the thermal limit. During the database generation process, once the current magnitude reaches a level where all the current phase angles fail to satisfy the thermal constraint, it is safe to stop the thermal FEA solver, since all the current magnitudes above such a level would also exceed the temperature limit.

Using this strategy, after the EM FEA database discussed in Section 3.5.3 is generated, it takes 14.4 core-hours to generate a 151 current amplitudes, 31 phase angles, and 6 rotor speeds thermal FEA database for one slot/pole combination. Among these 28086 ($151 \times 31 \times 6$) operating points, 17856 were skipped. After the databases are generated, the continuous operating region estimation requires little computation time (additional ~ 2 core-minutes after the efficiency map is generated). In total, it only takes several core-minutes to calculate the efficiency map and the continuous operating region of a scaled design.

4.6 Conclusion

In this chapter, the 2D CE scalable MS FE-based model presented in Chapter 3 is coupled with a 3D CE scalable thermal static FE-based model. An iterative approach is used to predict the converged temperature for each operating point under steady-state operation. Furthermore, through the use of thermal scaling relationships, the continuous operating region of the scaled design can be estimated using the pre-calculated FEA database, without the necessity to re-solve the computationally intensive 3D thermal FEA. The proposed EM-thermal coupled scalable model can provide more insights and information for powertrain-level simulation/optimization, and is useful in vehicle thermal management.

CHAPTER 5

Conclusion and Future Work

5.1 Conclusion

Computationally-efficient electromagnetic and thermal models of electric machines are presented in this dissertation.

A CE 3D FE-based dynamic thermal model is proposed, developed, and presented in Chapter 2. By applying orthogonal decomposition and eigenmode-based MOR, the full-order 3D FEA model can be reduced to a ROM with a small number of states based on the proposed "normalized extent of excitation" calculation. Results show that the proposed model can dramatically reduce the computation time by over 4 orders of magnitude comparing with a full-order dynamic thermal FEA model while maintaining satisfactory accuracy. Experimental results show that a ROM with 7 stator states and 4 rotor states can accurately capture the temperature response in the testing machine compared with measurements. A ratio of approximately 80000 between simulation time and real time was observed, which is fast enough for real-time implementation in embedded controllers. Such a CE thermal model can be useful in real-time condition monitoring, model-based controls, system-level simulation, and thermal protection/management. Moreover, the MOR process only requires calculating a small subset of eigenvectors of the full-order 3D FEA model, and does not depend on the inputs to the system. Thus, the ROM generation process is also fast. As a result, the combined computation time for generating and simulating the ROM is still about

3 times faster than simulating the full-order model. This can bring benefits to applications that require the generation of new full-order models at each iteration (e.g. electric machine design optimization).

In Chapter 3, a 2D CE scalable MS FE-based model is proposed, developed, and presented. Results show that the model can quickly generate new machine designs based on a given base design through three independent scaling techniques (dimensional scaling, number-of-turns scaling, and number-of-poles scaling). The scalable model can quickly predict the efficiency map of the scaled design using the pre-calculated FEA database. This avoids re-solving the computationally intensive FEA again for the scaled design, and takes only several core-minutes to generate the efficiency map for the scaled design. The proposed scalable model is feasible to be used in powertrain-level or system-level simulation/optimization, and allows powertrain designers to adjust the torque-speed curves and the shape of the efficiency map in ways favorable to overall powertrain performance.

In Chapter 4, the 2D CE scalable MS FE-based model is coupled with a 3D CE scalable thermal static FEA model. An iterative approach is used to predict the converged temperature for each operating point under steady-state operation. Furthermore, through the use of thermal scaling relationships, the continuous operating region of the scaled design can be estimated using the pre-calculated FEA database, without the necessity to re-solve the computationally intensive 3D thermal FEA. The proposed EM-thermal coupled scalable model can provide more insights and information for powertrain-level simulation/optimization, and is useful in vehicle thermal management.

5.2 Future Work

In this section, some of the future work directly related to this dissertation is presented.

5.2.1 CE Thermal Modeling

5.2.1.1 Error Estimation

The orthogonal decomposition based MOR technique presented in Chapter 2 is guaranteed to be stable, since all the eigenmodes in the full-order system are stable. However, the error induced by this MOR technique is not evaluated quantitatively in this dissertation. There has been some previous work for evaluating the error bound for other MOR techniques [76] (e.g. for Balanced Truncation MOR [77, 78] and alternating direction implicit (ADI) method [79]). It would be helpful to derive a quantitative relationship between error bound and the dynamic eigenmodes in the presented ROM, as this can provide insights for selecting the number of dynamic states in the ROM.

5.2.1.2 Applications of the Developed ROM

The CE reduced-order thermal model presented in Chapter 2 can be valuable in various applications, such as real-time thermal observers, model-based control, cooling system design, and thermal management.

Thermal Observer Implementation The initial condition in the CE ROM presented in Chapter 2 is a uniform temperature field T_0 across the entire machine. If the model is implemented as a real-time temperature monitor, it needs to start from a uniform temperature distribution and run continuously. To accommodate arbitrary initial conditions in temperature distribution, a thermal observer utilizing the CE ROM can be developed. By using temperature measurements from physical sensors, the ROM can converge to current states quickly after start. This would make the ROM more useful in real-time operations.

Model-based Control The CE ROM can be used in model-based control to allow temperature tracking by using actuators (fan, pump, compressor, etc) in cooling system. This can avoid over-cooling and reduce cooling power consumption. For example, the proposed

electric machine ROM was used in a vehicle thermal management system [15] which allows temperature tracking for stator peak temperature by using a Linear-Quadratic Regular (LQR). Future work includes multiple temperature tracking and high-reliability peak torque operation.

5.2.1.3 Computational Fluid Dynamics

One important perspective in thermal modeling of electric machines is the accurate calculation of convective heat transfer on machine boundaries. As discussed in Chapter 2.5, determining accurate heat transfer coefficients on the end-turn surface and rotor end surface due to rotor rotation at different speeds often requires detailed CFD simulation [58, 80–82] or complex experimental setups [5, 57, 59]. Since experimental setups are expensive and time-consuming to build, CFD is often preferred to save cost and shorten the turn-around time in design optimization.

CFD is the application of a variety of numerical methods to solve the equations that govern the flow dynamics, which is extremely computationally intensive (much more intensive than thermal conduction FEA) due to the highly nonlinear nature of the governing equations. Thus, it is not practical for use in a CE thermal model, or in design optimization. To address this issue, there have been several attempts to use CFD in a CE manner. For example, a limited CFD analysis was conducted only for the coolant in cooling channels and end-turn surface and combined with a LP model in [5]. This reduced the computation time of CFD to less than 30 minutes on a PC with 4GB memory and a Core 2 Duo 3.16 GHz CPU. CFD results have also been used in system identification studies serving as input data to build reduced-order models for electric machines [19] and batteries [83, 84].

As a result, future work is to investigate the possibility of conducting MOR on CFD. Although there have been numerous attempts on accelerating the solving of general CFD equations, there is no existing literature aiming specifically on the MOR of CFD for electric machines.

5.2.2 CE EM Modeling

5.2.2.1 Improvement for the Existing MS Scalable Model

More Degrees of Design Freedom In powertrain-level simulation/optimization, it is crucial to have enough degrees of design freedom to allow flexibility in re-shaping the efficiency map. Three design scaling techniques are used in this dissertation providing three design variables. More variables are desired to provide more freedom. The difficulty is to find an analytical relationship that can relate the base design and the modified design to avoid re-solving FEA.

Analytical AC Resistance Estimation One of the drawback of using MS FEA is the underestimation of winding conduction loss by neglecting skin and proximity effects. It is thus beneficial to develop an analytical AC resistance estimation method that can be integrated in the dimensional and number-of-turns scaling to allow quick estimation of AC resistance. Some analytical relationships and CE methods have been reported in the literature [85–88], and might be suitable to be used in the proposed scaling framework. It is also possible to develop a new analytical AC resistance estimation method that fits the proposed scaling techniques better.

Error Estimation It would be helpful to investigate how the error in efficiency between MS FEA simulation and experimental measurements of a prototype machine propagates in the proposed scaling techniques.

5.2.2.2 MOR of MQS FEA

MOR of MQS FEA is more difficult than the MOR of thermal conduction FEA presented in Chapter 2, since the assumption of linear material properties is no longer enough to capture the physics. Most of the nonlinearity in EM FEA comes from the nonlinear B-H curve in lamination, which has to be accurately captured to produce accurate results.

Traditionally, there has been much work on reducing full-order nonlinear dynamic systems into a reduced linear part (by using linear MOR techniques) plus a full-order nonlinear part. This method is effective only when the nonlinear part of the dynamic system is small, for example, in power systems or electronic circuits where there are only a few nonlinear components. Chaniotis and Pai [89] proposed to use Krylov-subspace based linear MOR techniques to reduce the linear part of the power system and couple the reduced linear model with nonlinear generators. However, these techniques are not suitable for tackling the distributed nature of the nonlinearity inside electric machines, since the laminations contribute to a large portion of the system dynamic equations.

Proper Orthogonal Decomposition (POD) is a nonlinear MOR technique based on the Karhunen-Loève (KL) transform. It has been used in electromagnetic [90] and thermal [91] ROMs in the literatures, although not for electric machines. To use POD, full-order nonlinear models are simulated with typical input commands to construct a series of "snapshots". Thus, the accuracy of POD-based ROM depends on the training commands. Furthermore, there are no formal rules on how to select "good" training commands [16].

A trajectory piecewise linear approach [92, 93] has been proposed for nonlinear MOR. The nonlinear material properties are modeled as piecewise linear curves. Thus, a nonlinear model can be decomposed into several piecewise linear models. MOR is then applied to each linear model. Depending on the operating points, the ROM switches between different piecewise linear models. This technique has been used in power electronic circuits [94, 95], where nonlinear inductors are modeled using switched linear inductors.

To date, there has not been any MOR for MQS FEA of electric machines reported in the literature. Thus, future work is to develop such a technique that can accurately capture the distributed nonlinearity inside the machine. Furthermore, if a good physics-based reduced-order MQS model is developed, it would allow an easy coupling with the presented reduced-order thermal model. Such a CE MQS-thermal coupled model would be valuable for various applications (e.g. machine design optimization, system-level simulation/opti-

mization, real-time control, model-based control, etc). In the following paragraphs, some initial thoughts and preliminary investigation on the development of a CE MQS FEA model is presented.

The idea is to decompose the full-order MQS model into linear, dynamic components and nonlinear, static components for stator and rotor, respectively. The stator and rotor are then coupled through a traveling-wave air-gap model. Eigenmode-based model order reduction techniques are applied to the linear, dynamic part of the model, while a computationally-efficient mapping between selected dynamic eigenmodes and specific magnetization patterns in the machine is developed to reduce the order of the nonlinear static part. Finally, the electrical variables are presented by a set of time-varying Fourier coefficients that will be constant under steady-state operating conditions. The block diagram of the proposed ROM is shown in Fig. 5.1.

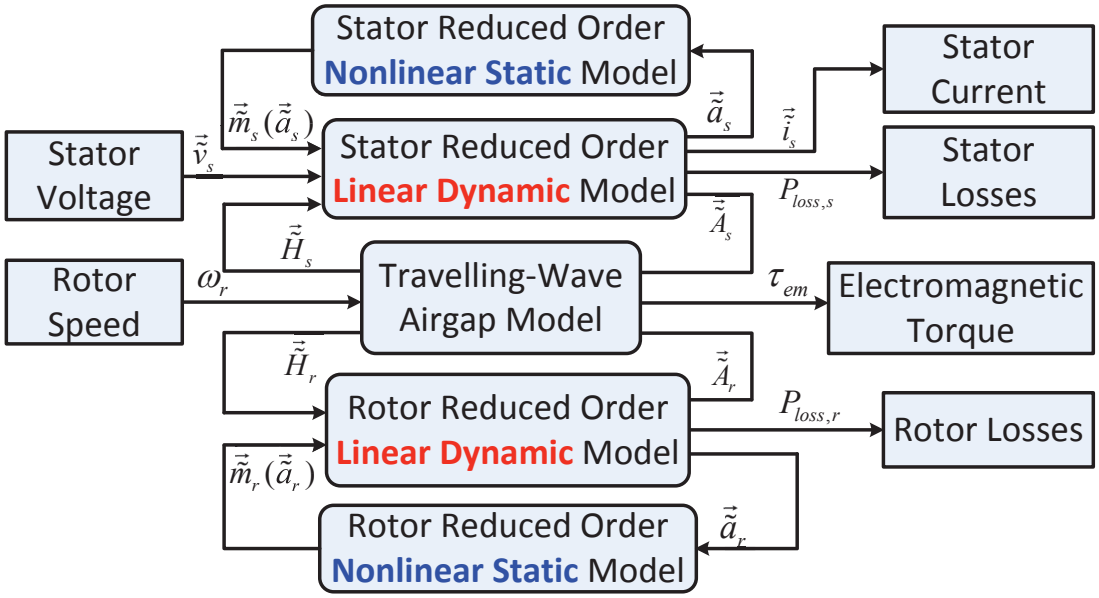

Figure 5.1: The idea of a MQS ROM for electric machines

A locked-rotor scenario with nonlinear magnetic material properties has been investigated first. This corresponds to the reduced-order linear dynamic blocks and the reduced-order nonlinear static blocks shown in Fig. 5.1 without the air-gap model. After discretizing

the nonlinear PDEs of the machine dynamics using FEA, the resulting nonlinear ODEs are given by:

$$\begin{bmatrix} \mathbf{C_{r11}} & \mathbf{0} & \mathbf{0} \\ \mathbf{0} & \mathbf{0} & \mathbf{0} \\ \mathbf{C_{r31}} & \mathbf{0} & \mathbf{0} \end{bmatrix} \begin{bmatrix} \dot{\vec{x}}_{r1} \\ \dot{\vec{x}}_{r2} \\ \dot{\vec{x}}_{r3} \end{bmatrix} + \begin{bmatrix} \mathbf{K_{r11}} & \mathbf{K_{r12}} & \mathbf{K_{r13}} \\ \mathbf{K_{r21}} & \mathbf{K_{r22}} & \mathbf{0} \\ \mathbf{0} & \mathbf{0} & \mathbf{K_{r33}} \end{bmatrix} \begin{bmatrix} \vec{x}_{r1} \\ \vec{x}_{r2} \\ \vec{x}_{r3} \end{bmatrix} + \begin{bmatrix} \mathbf{0} & \mathbf{0} & \mathbf{0} \\ \mathbf{0} & \mathbf{K_{ag}} & \mathbf{0} \\ \mathbf{0} & \mathbf{0} & \mathbf{0} \end{bmatrix} \begin{bmatrix} \vec{x}_{s1} \\ \vec{x}_{s2} \\ \vec{x}_{s3} \end{bmatrix} = \begin{bmatrix} \vec{f}_{r1} \\ -\vec{i}_{mr}\left(\vec{x}_{r2}\right) \\ 0 \end{bmatrix}, \tag{5.1}$$

$$\begin{bmatrix} \mathbf{C_{s11}} & \mathbf{0} & \mathbf{0} \\ \mathbf{0} & \mathbf{0} & \mathbf{0} \\ \mathbf{C_{s31}} & \mathbf{0} & \mathbf{0} \end{bmatrix} \begin{bmatrix} \dot{\vec{x}}_{s1} \\ \dot{\vec{x}}_{s2} \\ \dot{\vec{x}}_{s3} \end{bmatrix} + \begin{bmatrix} \mathbf{K_{s11}} & \mathbf{K_{s12}} & \mathbf{K_{s13}} \\ \mathbf{K_{s21}} & \mathbf{K_{s22}} & \mathbf{0} \\ \mathbf{0} & \mathbf{0} & \mathbf{K_{s33}} \end{bmatrix} \begin{bmatrix} \vec{x}_{s1} \\ \vec{x}_{s2} \\ \vec{x}_{s3} \end{bmatrix} + \begin{bmatrix} \mathbf{0} & \mathbf{0} & \mathbf{0} \\ \mathbf{0} & \mathbf{K_{ag}^{T}} & \mathbf{0} \\ \mathbf{0} & \mathbf{0} & \mathbf{0} \end{bmatrix} \begin{bmatrix} \vec{x}_{r1} \\ \vec{x}_{r2} \\ \vec{x}_{r3} \end{bmatrix} = \begin{bmatrix} 0 \\ -\vec{i}_{ms}\left(\vec{x}_{s2}\right) \\ \vec{f}_{s3} \end{bmatrix}, \tag{5.2}$$

where $\vec{x}_1$ and $\vec{x}_2$ corresponds to the magnetic vector potentials (MVPs) of the electrically conducting (e.g. copper and PM) and non-conducting (e.g. lamination) nodes, respectively. For rotor, $\vec{x}_{r3}$ corresponds to the electric potential of the PM region. For stator, $\vec{x}_{s3}$ has a length of $N_{s3} = \frac{N_{turns}N_{slots}}{N_{poles}} + 2N_{phase}$ which consists of $\frac{N_{turns}N_{slots}}{N_{poles}}$ electric potentials for each turn in each slot, N_{phase} phase voltages, and N_{phase} line currents. For a typical PM machine, the only excitation to the rotor is $\vec{f}_{r1}$, which corresponds to the magnetization of PM, and the only excitation to the stator is $\vec{f}_{s3}$, which corresponds to the input line current for a current-driven problem, or the input phase voltage for a voltage-driven problem. The equivalent magnetization currents $\vec{i}_{mr}\left(\vec{x}_{r2}\right)$ and $\vec{i}_{ms}\left(\vec{x}_{s2}\right)$ correspond to nonlinear behavior

of the soft magnetic materials (e.g. laminated iron).

From the second and third row of (5.1), we have

$$\begin{aligned}\vec{x}_{r2} &= -\mathbf{K_{r22}^{-1}}\left(\mathbf{K_{r21}}\vec{x}_{r1}+\mathbf{K_{ag}}\vec{x}_{s2}+\vec{i}_{mr}\right),\\ \vec{x}_{r3} &= -\mathbf{K_{r33}^{-1}}\mathbf{C_{r31}}\dot{\vec{x}}_{r1}.\end{aligned} \tag{5.3}$$

Substitute (5.3) into the first row of (5.1):

$$\begin{aligned}&\left(\mathbf{C_{r11}}-\mathbf{K_{r13}}\mathbf{K_{r33}^{-1}}\mathbf{C_{r31}}\right)\dot{\vec{x}}_{r1}+\left(\mathbf{K_{r11}}-\mathbf{K_{r12}}\mathbf{K_{r22}^{-1}}\mathbf{K_{r21}}\right)\vec{x}_{r1}\\ &\qquad=\vec{f}_{r1}+\mathbf{K_{r12}}\mathbf{K_{r22}^{-1}}\mathbf{K_{ag}}\vec{x}_{s2}+\mathbf{K_{r12}}\mathbf{K_{r22}^{-1}}\vec{i}_{mr}\end{aligned} \tag{5.4}$$

By solving the generalized eigenvector problem

$$\left(\mathbf{K_{r11}}-\mathbf{K_{r12}}\mathbf{K_{r22}^{-1}}\mathbf{K_{r21}}\right)\vec{v}_i=\lambda\left(\mathbf{C_{r11}}-\mathbf{K_{r13}}\mathbf{K_{r33}^{-1}}\mathbf{C_{r31}}\right)\vec{v}_i \tag{5.5}$$

and only model a few eigenmodes as dynamic modes while assuming the other modes converge to steady states instantaneously, (5.4) can be reduced to

$$\mathbf{c_r}\dot{\vec{y}}_r+\mathbf{k_r}\vec{y}_r=\mathbf{M_{r1}}\vec{x}_{s2}+\mathbf{M_{r2}}\vec{f}_{r1}+\mathbf{M_{mr1}}\vec{i}_{mr}, \tag{5.6}$$

$$\vec{x}_{r1}=\mathbf{V_{dr}}\vec{y}_r+\mathbf{M_{r3}}\vec{x}_{s2}+\mathbf{M_{r4}}\vec{f}_{r1}+\mathbf{M_{mr2}}\vec{i}_{mr}. \tag{5.7}$$

where

$$\mathbf{c_r} = \mathbf{V_{dr}^T}\left(\mathbf{C_{r11}} - \mathbf{K_{r13}K_{r33}^{-1}C_{r31}}\right)\mathbf{V_{dr}}, \tag{5.8}$$

$$\mathbf{k_r} = \mathbf{V_{dr}^T}\left(\mathbf{K_{r11}} - \mathbf{K_{r12}K_{r22}^{-1}K_{r21}}\right)\mathbf{V_{dr}}, \tag{5.9}$$

$$\mathbf{M_{r1}} = \mathbf{V_{dr}^T K_{r12} K_{r22}^{-1} K_{ag}}, \tag{5.10}$$

$$\mathbf{M_{r2}} = \mathbf{V_{dr}^T}, \tag{5.11}$$

$$\mathbf{M_{mr1}} = \mathbf{V_{dr}^T K_{r12} K_{r22}^{-1}}, \tag{5.12}$$

$$\mathbf{M_{r3}} = \mathbf{S_r K_{r12} K_{r22}^{-1} K_{ag}}, \tag{5.13}$$

$$\mathbf{M_{r4}} = \mathbf{S_r} = \left(\mathbf{K_{r11}} - \mathbf{K_{r12}K_{r22}^{-1}K_{r21}}\right)^{-1} - \mathbf{V_{dr}k_r^{-1}V_{dr}^T}, \tag{5.14}$$

$$\mathbf{M_{mr2}} = \mathbf{S_r K_{r12} K_{r22}^{-1}}. \tag{5.15}$$

By applying the similar model order reduction techniques to the stator, we have

$$\begin{bmatrix} \mathbf{c_r} & \mathbf{0} \\ \mathbf{0} & \mathbf{c_s} \end{bmatrix} \begin{bmatrix} \dot{\vec{y}}_r \\ \dot{\vec{y}}_s \end{bmatrix} + \begin{bmatrix} \mathbf{k_r} & \mathbf{0} \\ \mathbf{0} & \mathbf{k_s} \end{bmatrix} \begin{bmatrix} \vec{y}_r \\ \vec{y}_s \end{bmatrix} = \begin{bmatrix} \mathbf{M_{r2}} & \mathbf{0} \\ \mathbf{0} & \mathbf{M_{s2}} \end{bmatrix} \begin{bmatrix} \vec{f}_{r1} \\ \vec{f}_{s3} \end{bmatrix} + \begin{bmatrix} \mathbf{0} & \mathbf{M_{r1}} \\ \mathbf{M_{s1}} & \mathbf{0} \end{bmatrix} \begin{bmatrix} \vec{x}_{r2} \\ \vec{x}_{s2} \end{bmatrix} + \begin{bmatrix} \mathbf{M_{mr1}} & \mathbf{0} \\ \mathbf{0} & \mathbf{M_{ms1}} \end{bmatrix} \begin{bmatrix} \vec{i}_{mr} \\ \vec{i}_{ms} \end{bmatrix} \tag{5.16}$$

$$\begin{bmatrix} \vec{x}_{r1} \\ \vec{x}_{s1} \end{bmatrix} = \begin{bmatrix} \mathbf{V_{dr}} & \mathbf{0} \\ \mathbf{0} & \mathbf{V_{ds}} \end{bmatrix} \begin{bmatrix} \vec{y}_r \\ \vec{y}_s \end{bmatrix} + \begin{bmatrix} \mathbf{M_{r4}} & \mathbf{0} \\ \mathbf{0} & \mathbf{M_{s4}} \end{bmatrix} \begin{bmatrix} \vec{f}_{r1} \\ \vec{f}_{s3} \end{bmatrix} + \begin{bmatrix} \mathbf{0} & \mathbf{M_{r3}} \\ \mathbf{M_{s3}} & \mathbf{0} \end{bmatrix} \begin{bmatrix} \vec{x}_{r2} \\ \vec{x}_{s2} \end{bmatrix} + \begin{bmatrix} \mathbf{M_{mr2}} & \mathbf{0} \\ \mathbf{0} & \mathbf{M_{ms2}} \end{bmatrix} \begin{bmatrix} \vec{i}_{mr} \\ \vec{i}_{ms} \end{bmatrix} \tag{5.17}$$

By using the second row in (5.1) and (5.2) and substituting them into (5.16), the reduced

order model is

$$\mathbf{c}\begin{bmatrix}\dot{\vec{y}}_r\\ \dot{\vec{y}}_s\end{bmatrix}+\mathbf{k}\begin{bmatrix}\vec{y}_r\\ \vec{y}_s\end{bmatrix}=\mathbf{F_f}\begin{bmatrix}\vec{f}_{r1}\\ \vec{f}_{s3}\end{bmatrix}+\mathbf{F_i}\begin{bmatrix}\vec{i}_{mr}\\ \vec{i}_{ms}\end{bmatrix} \tag{5.18}$$

The discrete time, nonlinear form of (5.18), $\mathbf{c}\dot{\vec{y}}+\mathbf{k}\vec{y}=\mathbf{F_f}\vec{f}+\mathbf{F_i}\vec{i}_m$, can be then written as

$$\vec{r}\left(\vec{y}_{n+1}\right)=\left(\frac{\mathbf{c}}{h}+\mathbf{k}\right)\vec{y}_{n+1}-\frac{\mathbf{c}}{h}\vec{y}_n-\mathbf{F_f}\vec{f}_{n+1}-\mathbf{F_i}\vec{i}_{m,n+1}=0, \tag{5.19}$$

and solved by using Newton–Raphson Iteration:

$$\mathbf{J}\Delta\vec{y}=-\vec{r}\left(\vec{y}\right) \tag{5.20}$$

where the Jacobian matrix $\mathbf{J}=\frac{\partial\vec{r}}{\partial\vec{y}}=\frac{\mathbf{c}}{h}+\mathbf{k}-\mathbf{F_i}\frac{\partial\vec{i}_m}{\partial\vec{x}_2}\mathbf{T_1V_1}$ is a small matrix who has the same number of rows as the total number of dynamic states modeled in the reduced order model.

The nonlinear mapping between equivalent current and the MVPs of the non-conducting region, $\begin{bmatrix}\vec{i}_{mr}\\ \vec{i}_{ms}\end{bmatrix}=\vec{g}\left(\begin{bmatrix}\vec{x}_{r2}\\ \vec{x}_{s2}\end{bmatrix}\right)$, is governed by the following nonlinear equation:

$$\begin{bmatrix}\vec{x}_{r2}\\ \vec{x}_{s2}\end{bmatrix}-\mathbf{T_1V_1}\begin{bmatrix}\vec{y}_r\\ \vec{y}_s\end{bmatrix}-\mathbf{T_1S_1}\begin{bmatrix}\vec{f}_{r1}\\ \vec{f}_{s3}\end{bmatrix}-\left(\mathbf{T_1S_2}+\mathbf{T_2}\right)\vec{g}\left(\begin{bmatrix}\vec{x}_{r2}\\ \vec{x}_{s2}\end{bmatrix}\right)=\vec{0}. \tag{5.21}$$

Thus, $\begin{bmatrix}\vec{i}_{mr}\\ \vec{i}_{ms}\end{bmatrix}$ can be solved as a function of $\begin{bmatrix}\vec{y}_r\\ \vec{y}_s\end{bmatrix}$ and $\begin{bmatrix}\vec{f}_{r1}\\ \vec{f}_{s3}\end{bmatrix}$.

There are several techniques to reduce the computation burden of nonlinearity. For the sake of easy implement, the preliminary technique we use in this year is a multi-dimensional look-up table, whose inputs are machine excitations (e.g. current ampli-

tude and phase angle) and reduced order state variables $\begin{bmatrix} \vec{y}_r \\ \vec{y}_s \end{bmatrix}$, and outputs are $\mathbf{F_i}\vec{i}_m$, $\mathbf{F_i}\frac{\partial \vec{i}_m}{\partial \vec{x}_2}\mathbf{T_1}\mathbf{V_1}$, and torque. This look-up table can be constructed by solving (5.21) and then used to solve (5.19). The flowchart of the MOR process using look-up table is shown in Fig. 5.2.

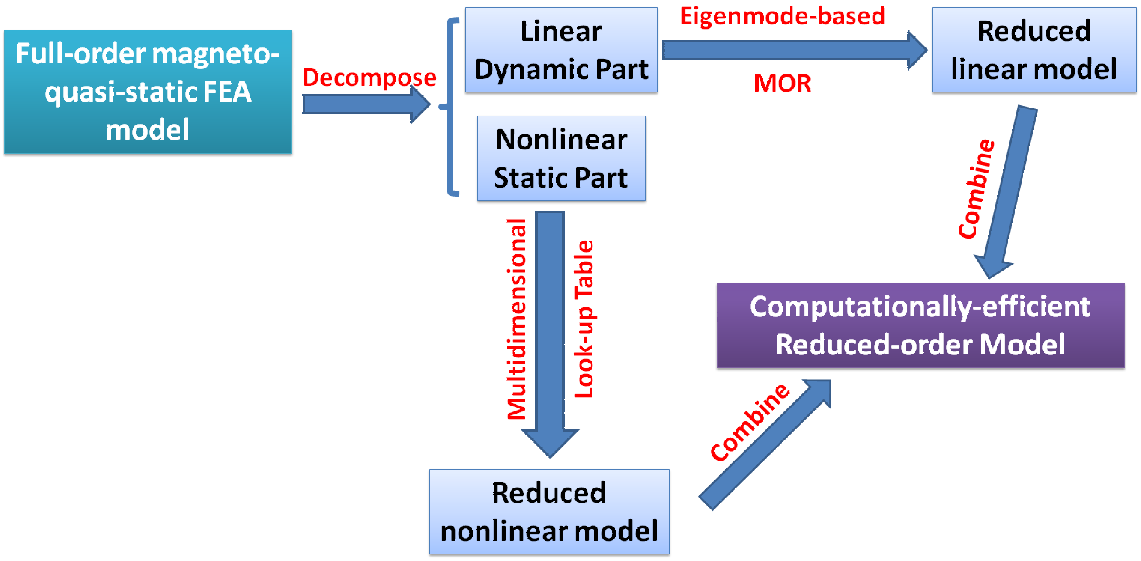

Figure 5.2: Flowchart of the MOR process using look-up table

By using the above approach, a full-order nonlinear FEA model can be reduced by using eigenmode-based MOR for the linear part and look-up table for the nonlinear part. For comparison purposes, four models (a full linear, a reduced linear, a full nonlinear, and a reduced nonlinear model) have been simulated for the UQM PowerPhase 145 machine, and the resulted torque are presented in Table 5.1 and Fig. 5.3. As can be seen in the table and figure, nonlinearity has significant contributions to torque [1] and thus has to be modeled to produce correct results. The reduced nonlinear model matched well with the full-order nonlinear model, and can reduce the computation time by more than one order

[1]Note that the linear models produce a much less torque than that of the nonlinear models in Fig. 5.3. This is because that the PM flux is shorted in the rotor containment ring when the ring is modeled as a linear material. There would be little flux going into the stator, resulting much less torque compared to the nonlinear models. For the nonlinear model, the containment ring is saturated, which allows flux to go into stator through air gap.

of magnitude from 23.7sec to 1.41sec.

Note that the reduced linear + reduced nonlinear model is significantly slower than the reduced-order linear model by about two orders of magnitude, which suggests that the nonlinear look-up table takes the majority of computation time. By replacing the look-up table with a more efficient nonlinear MOR reduction technique, the computation time of the proposed ROM can be further reduced. Future work involves improving the nonlinear MOR, adding the traveling-wave air-gap model, and complete the proposed framework shown in Fig. 5.1.

Table 5.1: Comparison of four different MQS models

Models	Number of States (Stator+Rotor)	Computation Time	RMSE (Nm)
Full-order nonlinear	1301+599	23.7sec	N/A
Reduced linear + reduced nonlinear	1+1	1.41sec	1.24
Full-order linear	1301+599	6.77sec	124.63
Reduced-order linear	1+1	16.2ms	124.64

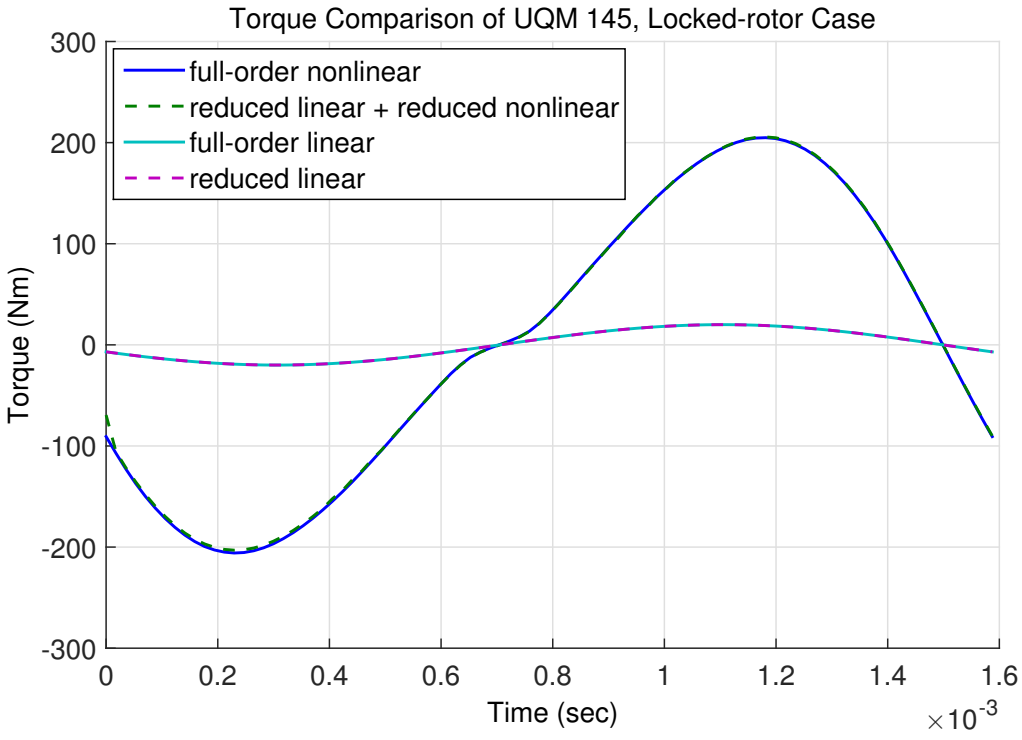

Figure 5.3: Torque comparison of four different MQS models

Appendix

Publications during Ph.D. Study

1. **K. Zhou**, A. Ivanco, Z. Filipi, and H. Hofmann, "Finite-Element-Based Computationally-Efficient Scalable Electric Machine Model Suitable for Electrified Powertrain Simulation and Optimization," *Industry Applications, IEEE Transactions on*, vol.PP, no.99, pp.1,1, to appear in Nov./Dec. 2015.

2. **K. Zhou**, J. Pries, and H. Hofmann, "Computationally-Efficient 3D Finite-Element-Based Dynamic Thermal Models of Electric Machines," *Transportation Electrification, IEEE Transactions on*, accepted.

3. X. Tao, **K. Zhou**, A. Ivanco, J. Wagner, H. Hofmann, and Z. Filipi, "A Hybrid Electric Vehicle Thermal Management System - Nonlinear Controller Design," SAE Technical Paper 2015-01-1710, 2015.

4. D. Reed, **K. Zhou**, H. Hofmann, and J. Sun, "A Stator Current Locus Approach for Induction Machine Parameter Estimation," in *Transportation Electrification Conference and Expo - Asia Pacific (ITEC Asia-Pacific), 2014 IEEE*, August 2014.

5. J. Hou, D. Reed, **K. Zhou**, H. Hofmann, and J. Sun, "Modeling and Test-bed Development for an Electric Drive System with Hybrid Energy Storage," in *Electric Machines Technology Symposium (EMTS), 2014 ASNE*, May 2014.

6. A. Ivanco, **K. Zhou**, H. Hofmann, and Z. Filipi, "A Framework for Optimization of the Traction Motor Design Based on the Series-HEV System Level Goals," SAE Technical Paper 2014-01-1801, 2014.

7. **K. Zhou**, A. Ivanco, Z. Filipi, and H. Hofmann, "Finite-Element-Based Computationally Efficient Electric Machine Model Suitable for Integration in Electrified Vehicle Powertrain Design Optimization," in *Applied Power Electronics Conference and Exposition (APEC), 2014 Twenty-Ninth Annual IEEE*, pp. 1598–1603, March 2014.

8. **K. Zhou**, J. Pries, and H. Hofmann, "Computationally-efficient 3D finite-element-based dynamic thermal models of electric machines," in *Electric Machines & Drives Conference (IEMDC), 2013 IEEE International*, pp. 839–846, May 2013.

9. **K. Zhou**, J. Pries, and H. Hofmann, Y. Kim, T.-K. Lee, and Z. Filipi, "Computationally-efficient finite-element-based thermal models of electric machines," in *Vehicle Power and Propulsion Conference (VPPC), 2011 IEEE*, pp. 1-6, Sept. 2011.

BIBLIOGRAPHY

[1] "Electrification roadmap - revolutionizing transportation and achieving energy security," Electrification Coalition, Washington, DC, U.S., Tech. Rep., Nov. 2009. [Online]. Available: http://www.electrificationcoalition.org/policy/electrification-roadmap

[2] "Transportation energy futures: Project overview and findings," U.S. Department of Energy, Tech. Rep. NREL/PR-6A20-56270, Mar. 2013. [Online]. Available: http://www.nrel.gov/analysis/transportation_futures/index.html

[3] P. Mellor, D. Roberts, and D. Turner, "Lumped parameter thermal model for electrical machines of TEFC design," *IEE PROC-B*, vol. 138, no. 5, pp. 205–218, Sep. 1991.

[4] A. EL-Refaie, N. Harris, T. Jahns, and K. Rahman, "Thermal analysis of multibarrier interior PM synchronous machine using lumped parameter model," *IEEE Trans. Energy Convers.*, vol. 19, no. 2, pp. 303–309, Jun. 2004.

[5] S. Nategh, H. Zhe, A. Krings, O. Wallmark, and M. Leksell, "Thermal modeling of directly cooled electric machines using lumped parameter and limited CFD analysis," *IEEE Trans. Energy Convers.*, vol. 28, no. 4, pp. 979–990, Dec. 2013.

[6] P. Zhang, Y. Du, T. Habetler, and B. Lu, "A survey of condition monitoring and protection methods for medium-voltage induction motors," *IEEE Trans. Ind. Appl.*, vol. 47, no. 1, pp. 34–46, Jan.–Feb. 2011.

[7] W. Wu, J. Dunlop, S. Collocott, and B. Kalan, "Design optimization of a switched reluctance motor by electromagnetic and thermal finite-element analysis," *IEEE Trans. Magn.*, vol. 39, no. 5, pp. 3334–3336, Sep. 2003.

[8] B. Funieru and A. Binder, "Thermal design of a permanent magnet motor used for gearless railway traction," in *Proc. 2008 34th Annu. Conf. IEEE Ind. Electron. (IECON)*, Nov. 2008, pp. 2061–2066.

[9] J. Fan, C. Zhang, Z. Wang, and E. Strangas, "Thermal analysis of water cooled surface mount permanent magnet electric motor for electric vehicle," in *Proc. 2010 Int. Conf. Elect. Mach. Syst. (ICEMS)*, Oct. 2010, pp. 1024–1028.

[10] V. Buyukdegirmenci and P. Krein, "Machine characterization for short-term or instantaneous torque capabilities: An approach based on transient thermal response," in *Proc. 2013 IEEE Int. Elect. Mach. & Drives Conf. (IEMDC)*, May 2013, pp. 801–808.

[11] C. Kral, A. Haumer, and S. B. Lee, "A practical thermal model for the estimation of permanent magnet and stator winding temperatures," *IEEE Trans. Power Electron.*, vol. 29, no. 1, pp. 455–464, Jan. 2014.

[12] M. Valenzuela and P. Reyes, "Simple and reliable model for the thermal protection of variable-speed self-ventilated induction motor drives," *IEEE Trans. Ind. Appl.*, vol. 46, no. 2, pp. 770–778, Mar. 2010.

[13] J. Legranger, G. Friedrich, S. Vivier, and J. Mipo, "Combination of finite-element and analytical models in the optimal multidomain design of machines: Application to an interior permanent-magnet starter generator," *IEEE Trans. Ind. Appl.*, vol. 46, no. 1, pp. 232–239, Jan. 2010.

[14] A. Ivanco, K. Zhou, H. Hofmann, and Z. Filipi, "A framework for optimization of the traction motor design based on the series-HEV system level goals," *SAE Technical Paper 2014-01-1801*, Apr. 2014.

[15] X. Tao, K. Zhou, A. Ivanco, J. R. Wagner, H. Hofmann, and Z. Filipi, "A hybrid electric vehicle thermal management system - nonlinear controller design," *SAE Technical Paper 2015-01-1710*, Apr. 2015.

[16] T. Bechtold, E. B. Rudnyi, and J. G. Korvink, "Dynamic electro-thermal simulation of microsystems – a review," *J. Micromech. Microeng.*, vol. 15, no. 11, p. R17, Nov. 2005.

[17] Z. Gao, R. Colby, T. Habetler, and R. Harley, "A model reduction perspective on thermal models for induction machine overload relays," *IEEE Trans. Ind. Electron.*, vol. 55, no. 10, pp. 3525–3534, Oct. 2008.

[18] P. Zhang, Y. Du, and T. G. Habetler, "A transfer-function-based thermal model reduction study for induction machine thermal overload protective relays," *IEEE Trans. Ind. Appl.*, vol. 46, no. 5, pp. 1919–1926, Sep.–Oct. 2010.

[19] N. Jaljal, J. Trigeol, and P. Lagonotte, "Reduced thermal model of an induction machine for real-time thermal monitoring," *IEEE Trans. Ind. Electron.*, vol. 55, no. 10, pp. 3535–3542, Oct. 2008.

[20] G. Demetriades, H. de la Parra, E. Andersson, and H. Olsson, "A real-time thermal model of a permanent-magnet synchronous motor," *IEEE Trans. Power Electron.*, vol. 25, no. 2, pp. 463–474, Feb. 2010.

[21] S. Karagol and M. Bikdash, "Generation of equivalent-circuit models from simulation data of a thermal system," *IEEE Trans. Power Electron.*, vol. 25, no. 4, pp. 820–828, Sep. 2010.

[22] Y. Gerstenmaier and G. Wachutka, "Time dependent temperature fields calculated using eigenfunctions and eigenvalues of the heat conduction equation," *Microelectronics J.*, vol. 32, no. 1011, pp. 801 – 808, Oct. 2001.

[23] K. Zhou, J. Pries, H. Hofmann, Y. Kim, T.-K. Lee, and Z. Filipi, "Computationally-efficient finite-element-based thermal models of electric machines," in *Proc. 2011 IEEE Vehicle Power & Propulsion Conf. (VPPC)*, Sep. 2011, pp. 1–6.

[24] J. Pries, "Computationally efficient steady-state simulation algorithms for finite-element models of electric machines," Ph.D. Dissertation, Univ. of Michigan, Dept. Elect. Eng. Comput. Sci., Ann Arbor, MI, U.S., 2015.

[25] D. Ionel, M. Popescu, M. McGilp, T. Miller, and S. Dellinger, "Assessment of torque components in brushless permanent-magnet machines through numerical analysis of the electromagnetic field," *IEEE Trans. Ind. Appl.*, vol. 41, no. 5, pp. 1149–1158, Sep. 2005.

[26] M. Barcaro, N. Bianchi, and F. Magnussen, "Average and oscillating torque determination in fractional-slot PM motors," in *Proc. 2010 19th Int. Conf. Elect. Mach. (ICEM)*, Sep. 2010, pp. 1–7.

[27] D. Ionel and M. Popescu, "Finite-element surrogate model for electric machines with revolving field - application to IPM motors," *IEEE Trans. Ind. Appl.*, vol. 46, no. 6, pp. 2424–2433, Nov. 2010.

[28] D. Ionel and M. Popescu, "Ultrafast finite-element analysis of brushless PM machines based on space-time transformations," *IEEE Trans. Ind. Appl.*, vol. 47, no. 2, pp. 744–753, Mar. 2011.

[29] G. Sizov, D. Ionel, and N. Demerdash, "Modeling and parametric design of permanent-magnet ac machines using computationally efficient finite-element analysis," *IEEE Trans. Ind. Electron.*, vol. 59, no. 6, pp. 2403–2413, Jun. 2012.

[30] P. Zhang, G. Sizov, J. He, D. Ionel, and N. Demerdash, "Calculation of magnet losses in concentrated-winding permanent-magnet synchronous machines using a computationally efficient finite-element method," *IEEE Trans. Ind. Appl.*, vol. 49, no. 6, pp. 2524–2532, Nov. 2013.

[31] T. Miller, M. Popescu, C. Cossar, M. McGilp, M. Olaru, A. Davies, J. Sturgess, and A. Sitzia, "Embedded finite-element solver for computation of brushless permanent-magnet motors," *IEEE Trans. Ind. Appl.*, vol. 44, no. 4, pp. 1124–1133, Jul. 2008.

[32] F. Marignetti, V. Delli Colli, and Y. Coia, "Design of axial flux PM synchronous machines through 3-D coupled electromagnetic thermal and fluid-dynamical finite-element analysis," *IEEE Trans. Ind. Electron.*, vol. 55, no. 10, pp. 3591–3601, Oct. 2008.

[33] R. Wrobel, J. Goss, A. Mlot, and P. Mellor, "Design considerations of a brushless open-slot radial-flux PM hub motor," *IEEE Trans. Ind. Appl.*, vol. 50, no. 3, pp. 1757–1767, May 2014.

[34] L. Alberti, N. Bianchi, M. Morandin, and J. Gyselinck, "Finite-element analysis of electrical machines for sensorless drives with signal injection," in *Proc. 2012 IEEE Energy Conversion Congr. and Expo. (ECCE)*, Sep. 2012, pp. 861–868.

[35] V. Ruuskanen, J. Nerg, J. Pyrhonen, S. Ruotsalainen, and R. Kennel, "Drive cycle analysis of a permanent-magnet traction motor based on magnetostatic finite-element analysis," *IEEE Trans. Veh. Technol.*, vol. 64, no. 3, pp. 1249–1254, Mar. 2015.

[36] S. Lukic and A. Emadi, "Modeling of electric machines for automotive applications using efficiency maps," in *Proc. 2003 Elect. Insulation Conf. and Elect. Manufacturing Coil Winding Technology Conf.*, Sep. 2003, pp. 543–550.

[37] S. Lukic and A. Emadi, "Effects of drivetrain hybridization on fuel economy and dynamic performance of parallel hybrid electric vehicles," *IEEE Trans. Veh. Technol.*, vol. 53, no. 2, pp. 385–389, Mar. 2004.

[38] S. Williamson, M. Lukic, and A. Emadi, "Comprehensive drive train efficiency analysis of hybrid electric and fuel cell vehicles based on motor-controller efficiency modeling," *IEEE Trans. Power Electron.*, vol. 21, no. 3, pp. 730–740, May 2006.

[39] J. Estima and A. Marques Cardoso, "Efficiency analysis of drive train topologies applied to electric/hybrid vehicles," *IEEE Trans. Veh. Technol.*, vol. 61, no. 3, pp. 1021–1031, Mar. 2012.

[40] X. Liu, D. Wu, Z. Zhu, A. Pride, R. Deodhar, and T. Sasaki, "Efficiency improvement of switched flux PM memory machine over interior PM machine for EV/HEV applications," *IEEE Trans. Magn.*, vol. 50, no. 11, pp. 1–4, Nov. 2014.

[41] K. Kiyota, H. Sugimoto, and A. Chiba, "Comparison of energy consumption of SRM and IPMSM in automotive driving schedules," in *Proc. 2012 IEEE Energy Conversion Congr. and Expo. (ECCE)*, Sep. 2012, pp. 853–860.

[42] E. Dlala, M. Solveson, S. Stanton, Z. Tang, M. Christini, R. Ong, and B. Peaslee, "Efficiency map simulations for an interior pm motor with experimental comparison and investigation of magnet size reduction," in *Proc. 2013 IEEE Int. Elect. Mach. & Drives Conf. (IEMDC)*, May 2013, pp. 23–29.

[43] K.-T. Hsieh and B. Kim, "One kind of scaling relations on electromechanical systems," *IEEE Trans. Magn.*, vol. 33, no. 1, pp. 240–244, Jan. 1997.

[44] J. Pries and H. Hofmann, "Magnetic and thermal scaling of electric machines," *Int. J. of Vehicle Design*, vol. 61, no. 1, pp. 219–232, 2013.

[45] K. Upendra and A. Grauers, "Requirements on electric machines for road vehicles – a preliminary study with focus on thermal limits under transient load," Swedish Hybrid Vehicle Centre, Chalmers Univ. of Technology, Tech. Rep., May 2014.

[46] L. Li, W. Fu, S. Niu, S. Ho, and Y. Li, "A quantitative comparison study of power electronic driven flux-modulated machines using magnetic field and thermal field co-simulation," *IEEE Trans. Ind. Electron.*, vol. PP, no. 99, pp. 1–1, 2015.

[47] W. Jiang and T. Jahns, "Coupled electromagnetic–thermal analysis of electric machines including transient operation based on finite-element techniques," *IEEE Trans. Ind. Appl.*, vol. 51, no. 2, pp. 1880–1889, Mar. 2015.

[48] B. Zhang, R. Qu, J. Wang, J. Li, W. Xu, and Y. Chen, "Electromagnetic–Thermal Coupling Analysis of Permanent Magnet Synchronous Machines for Electric Vehicle Applications Based on Improved $\mu + 1$ Evolution Strategy," *IEEE Trans. Magn.*, vol. 51, no. 4, pp. 1–10, Apr. 2015.

[49] S. A. Semidey, Y. Duan, J. R. Mayor, R. G. Harley, and T. G. Habetler, "Optimal electromagnetic-thermo-mechanical integrated design candidate search and selection for surface-mount permanent-magnet machines considering load profiles," *IEEE Trans. Ind. Appl.*, vol. 47, no. 6, pp. 2460–2468, Nov. 2011.

[50] H.-y. Chang and Y.-p. Yang, "Coupled electromagnetic and thermal–fluid analysis for a permanent magnet synchronous motor," in *Proc. 2nd Intl. Conf. Adv. Mech. Robot. Eng. (AMRE2014)*, no. 1, Oct. 2014, pp. 13–17.

[51] B. K. Donaldson, *Introduction to Structural Dynamics*. Cambridge University Press, 2006.

[52] D. Staton, A. Boglietti, and A. Cavagnino, "Solving the more difficult aspects of electric motor thermal analysis in small and medium size industrial induction motors," *IEEE Trans. Energy Convers.*, vol. 20, no. 3, pp. 620–628, Sep. 2005.

[53] T. Hayase, J. Humphrey, and R. Greif, "Numerical calculation of convective heat transfer between rotating coaxial cylinders with periodically embedded cavities," *J. Heat Transfer*, vol. 114, no. 3, pp. 589–597, Aug. 1992.

[54] "UQM PowerPhase 145 datasheet," UQM Technologies Inc., Longmont, Colorado, U.S.

[55] J. Pries and H. Hofmann, "Steady-state algorithms for nonlinear time-periodic magnetic diffusion problems using diagonally-implicit runge-kutta methods," *IEEE Trans. Magn.*, vol. 51, no. 4, pp. 1–12, Apr. 2015.

[56] J. D. Lambert, *Numerical Methods for Ordinary Differential Systems: The Initial Value Problem*. New York, NY, U.S.: John Wiley & Sons, Inc., 1991.

[57] H. H. Cho, C. H. Won, G. Y. Ryu, and D. H. Rhee, "Local heat transfer characteristics in a single rotating disk and co-rotating disks," *Microsyst. Technol.*, vol. 9, no. 6-7, pp. 399–408, Sep. 2003.

[58] C. Kral, A. Haumer, M. Haigis, H. Lang, and H. Kapeller, "Comparison of a CFD analysis and a thermal equivalent circuit model of a TEFC induction machine with measurements," *IEEE Trans. Energy Convers.*, vol. 24, no. 4, pp. 809–818, Dec. 2009.

[59] A. Boglietti, A. Cavagnino, D. Staton, M. Popescu, C. Cossar, and M. McGilp, "End space heat transfer coefficient determination for different induction motor enclosure types," *IEEE Trans. Ind. Appl.*, vol. 45, no. 3, pp. 929–937, May 2009.

[60] J. Hendershot and T. Miller, *Design of brushless permanent-magnet machines*. Venice, Florida, U.S.: Motor Design Books, 2010.

[61] M. F. Hsieh, Y. C. Hsu, D. G. Dorrell, and K. H. Hu, "Investigation on end winding inductance in motor stator windings," *IEEE Trans. Magn.*, vol. 43, no. 6, pp. 2513–2515, 2007.

[62] N. Alatawneh and P. Pillay, "The minor hysteresis loop under rotating magnetic fields in machine laminations," *IEEE Trans. Ind. Appl.*, vol. 50, no. 4, pp. 2544–2553, Jul.–Aug. 2014.

[63] F. Fiorillo and A. Novikov, "An improved approach to power losses in magnetic laminations under nonsinusoidal induction waveform," *IEEE Trans. Magn.*, vol. 26, no. 5, pp. 2904–2910, Sep. 1990.

[64] K. Venkatachalam, C. Sullivan, T. Abdallah, and H. Tacca, "Accurate prediction of ferrite core loss with nonsinusoidal waveforms using only Steinmetz parameters," in *Proc. 2002 IEEE Workshop Comput. Power Electron.*, Jun. 2002.

[65] Y. Chen and P. Pillay, "An improved formula for lamination core loss calculations in machines operating with high frequency and high flux density excitation," in *Proc. 2002 37th IEEE Ind. Appl. Conf. (IAS Annual Meeting)*, vol. 2, Oct. 2002, pp. 759–766.

[66] K. Yoshida, Y. Hita, and K. Kesamaru, "Eddy-current loss analysis in PM of surface-mounted-PM SM for electric vehicles," *IEEE Trans. Magn.*, vol. 36, no. 4, pp. 1941–1944, Jul. 2000.

[67] C. Deak, L. Petrovic, A. Binder, M. Mirzaei, D. Irimie, and B. Funieru, "Calculation of eddy current losses in permanent magnets of synchronous machines," in *Proc. 2008 Int. Symp. Power Electron., Electr. Drives, Autom. Motion (SPEEDAM)*, Jun. 2008, pp. 26–31.

[68] S. J. Salon, *Finite Element Analysis of Electrical Machines*. Boston, Massachusetts, U.S.: Kluwer Academic Publishers, 1995.

[69] D. Graovac and M. Purschel, "Igbt power losses calculation using the data-sheet parameters," Infineon Application Note v1.1, Tech. Rep., 2009.

[70] W. Rui, W. Jialiang, H. Jian, C. Zhongyuan, W. Quanqing, J. Na, and W. Chenghao, "A power loss calculation method of IGBT three-phase SPWM converter," in *Proc. 2012 2nd Int. Conf. Intell. Syst. Design Eng. Applicat. (ISDEA)*, Jan. 2012, pp. 1180–1183.

[71] M. Thompson, C. Hoff, and J. Gover, "A model to estimate the effect of DC bus voltage on HEV powertrain efficiency," in *Proc. 2010 IEEE Vehicle Power & Propulsion Conf. (VPPC)*, Sep. 2010, pp. 1–5.

[72] A. D. Rajapakse, A. M. Gole, and P. L. Wilson, "Approximate loss formulae for estimation of IGBT switching losses through EMTP-type simulations," in *Proc. 2005 Int. Conf. Power Syst. Transients (IPST)*, Jun. 2005, p. 05IPST184.

[73] Y. C. Kwon, S. Kim, and S. K. Sul, "Six-step operation of PMSM with instantaneous current control," *IEEE Trans. Ind. Appl.*, vol. 50, no. 4, pp. 2614–2625, Jul. 2014.

[74] F. Zhang, G. Du, T. Wang, G. Liu, and W. Cao, "Rotor retaining sleeve design for a 1.12-MW high-speed PM machine," *IEEE Trans. Ind. Appl.*, vol. PP, no. 99, pp. 1–1, 2015.

[75] T. Hughes, *The Finite Element Method: Linear Static and Dynamic Finite Element Analysis*. Mineola, New York, U.S.: Dover Publications, 2000.

[76] F. Freitas, J. Rommes, and N. Martins, "Gramian-based reduction method applied to large sparse power system descriptor models," *IEEE Trans. Power Syst.*, vol. 23, no. 3, pp. 1258–1270, Aug. 2008.

[77] J. R. Li, "Model reduction of large linear systems via low rank system gramians," Ph.D. Dissertation, Massachusetts Inst. Technol., Dept. Math., Cambridge, MA, U.S., 2000.

[78] K. Glover, "All optimal Hankel-norm approximations of linear multivariable systems and their L^{∞}-error bounds," *Int. J. Control*, vol. 39, no. 6, pp. 1115–1193, 1984.

[79] C. Sorensen and Y. Zhou, "Bounds on eigenvalue decay rates and sensitivity of solutions to lyapunov equations," Rice Univ., Houston, TX, U.S., Tech. Rep. TR02-07, Mar. 2002.

[80] M. Hettegger, A. Reinbacher-Kostinger, and O. Biro, "Characterizing the convective wall heat transfer on convoluted shapes in the end-region of an induction machine," in *Proc. 2012 XXth Int. Conf. Elect. Mach. (ICEM)*, Sep. 2012, pp. 1219–1226.

[81] D. Lampard, S. Pickering, and J. Mugglestone, "The use of computational fluid dynamics to model the air flow in the end region of a TEFC induction motor," in *Proc. IEE Colloq. Modeling the Performance of Elect. Mach.*, Apr. 1997, pp. 2/1–2/5.

[82] D. Howey, A. Holmes, and K. Pullen, "Measurement and CFD prediction of heat transfer in air-cooled disc-type electrical machines," *IEEE Trans. Ind. Appl.*, vol. 47, no. 4, pp. 1716–1723, Jul. 2011.

[83] X. Hu, S. Asgari, S. Lin, S. Stanton, and W. Lian, "A linear parameter-varying model for HEV/EV battery thermal modeling," in *Proc. 2012 IEEE Energy Conversion Congr. Expo. (ECCE)*, Sep. 2012, pp. 1643–1649.

[84] X. Hu, L. Chaudhari, S. Lin, S. Stanton, S. Asgari, and W. Lian, "A state space thermal model for HEV/EV battery using vector fitting," in *Proc. 2012 IEEE Transportation Electrification Conf. Expo. (ITEC)*, Jun. 2012, pp. 1–8.

[85] L. J. Wu, Z. Q. Zhu, D. Staton, M. Popescu, and D. Hawkins, "Analytical model of eddy current loss in windings of permanent-magnet machines accounting for load," *IEEE Trans. Magn.*, vol. 48, no. 7, pp. 2138–2151, Jul. 2012.

[86] H.-K. Kim, J.-K. Jung, K.-Y. Park, C.-H. Im, and H.-K. Jung, "Efficient technique for 3-D finite element analysis of skin effect in current-carrying conductors," *IEEE Trans. Magn.*, vol. 40, no. 2, pp. 1326–1329, Mar. 2004.

[87] P. Wallmeier, "Improved analytical modeling of conductive losses in gapped high-frequency inductors," *IEEE Trans. Ind. Appl.*, vol. 37, no. 4, pp. 1045–1054, Jul. 2001.

[88] C. R. Sullivan, "Computationally efficient winding loss calculation with multiple windings, arbitrary waveforms, and two-dimensional or three-dimensional field geometry," *IEEE Trans. Power Electron.*, vol. 16, no. 1, pp. 142–150, Jan. 2001.

[89] D. Chaniotis and M. Pai, "Model reduction in power systems using Krylov subspace methods," *IEEE Trans. Power Syst.*, vol. 20, no. 2, pp. 888–894, May 2005.

[90] M. E. Kowalski and J. M. Jin, "Model-order reduction of nonlinear models of electromagnetic phased-array hyperthermia," *IEEE Trans. Biomed. Eng.*, vol. 50, no. 11, pp. 1243–1254, Nov. 2003.

[91] H. Park and M. Sung, "Identification and feedback control of rapid thermal processing systems," *Chem. Eng. Commun.*, vol. 190, no. 11, pp. 1521–1540, 2003.

[92] M. Rewienski and J. White, "A trajectory piecewise-linear approach to model order reduction and fast simulation of nonlinear circuits and micromachined devices," *IEEE Trans. Comput.-Aided Design Integr. Circuits Syst.*, vol. 22, no. 2, pp. 155–170, Feb. 2003.

[93] B. Bond and L. Daniel, "A piecewise-linear moment-matching approach to parameterized model-order reduction for highly nonlinear systems," *IEEE Trans. Comput.-Aided Design Integr. Circuits Syst.*, vol. 26, no. 12, pp. 2116–2129, Dec. 2007.

[94] A. Davoudi, P. L. Chapman, J. Jatskevich, and H. Behjati, "Reduced-order dynamic modeling of multiple-winding power electronic magnetic components," *IEEE Trans. Power Electron.*, vol. 27, no. 5, pp. 2220–2226, May 2012.

[95] A. Davoudi, J. Jatskevich, P. L. Chapman, and A. Bidram, "Multi-resolution modeling of power electronics circuits using model-order reduction techniques," *IEEE Trans. Circuits Syst. I Regul. Pap.*, vol. 60, no. 3, pp. 810–823, Mar. 2013.